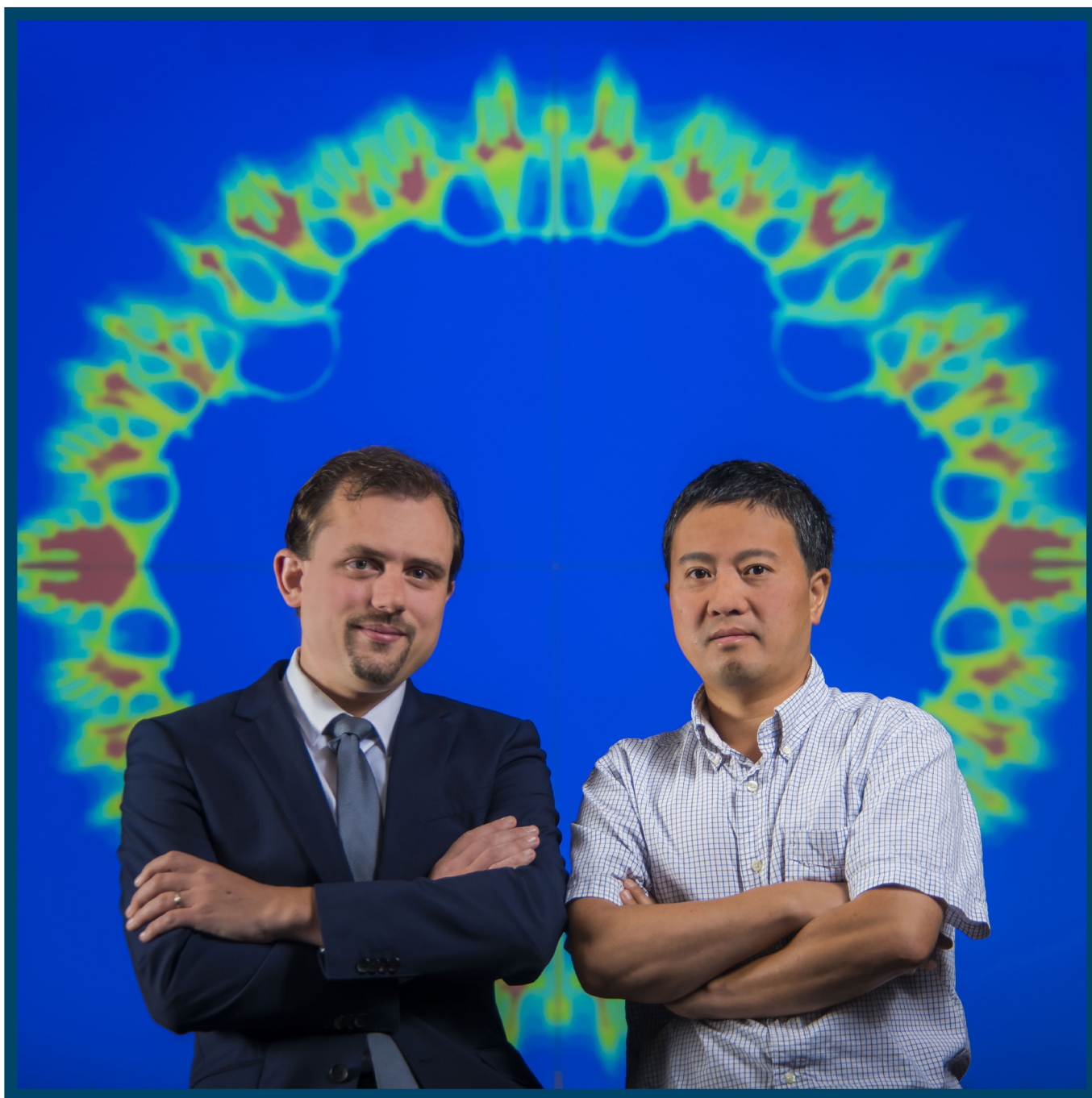


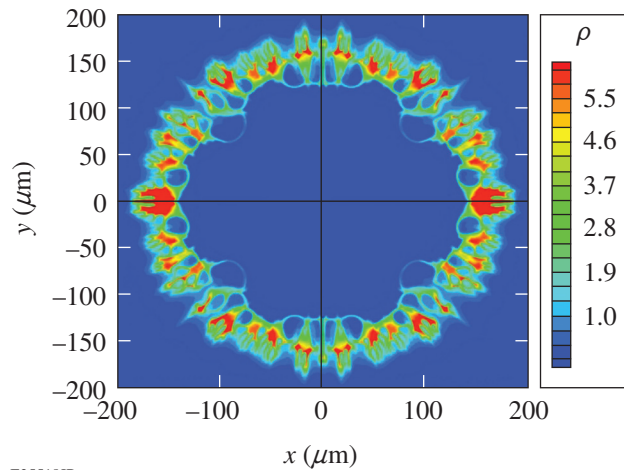
# LLE Review

## Quarterly Report



## About the Cover:

The cover photo shows LLE Scientists Drs. D. T. Michel (left) and S. X. Hu (right) who report on the study of the effect of adiabat on shell decomposition of direct-drive warm-CH implosions on OMEGA. The maximum in-flight shell thickness was obtained using a novel technique where the outer and inner surfaces of the shell were simultaneously measured using self-emission images of the imploding target. When the calculated adiabat of the shell was decreased from 6 to 4.5, the shell thickness was measured to decrease, but when the adiabat was decreased further (1.8), the shell thickness increased. Over this adiabat range, the measured minimum core size continued to decrease, demonstrating that the decompression of the shell measured for low adiabats was not a result of errors in the adiabat calculations, but was caused by the increase in the Rayleigh–Taylor growth associated with a reduction in ablation velocity at lower adiabats. The 2-D hydrodynamic simulations of these experiments were the first to simultaneously include laser imprint (modes 2 to 200) and state-of-the-art physics models for cross-beam energy transfer, nonlocal thermal transport, and first-principles equation of state. The simulations reproduce the measured outer shell trajectory, maximum in-flight shell thicknesses, inner shell deceleration, minimum core size, and neutron yields, and show that the increased shell thickness for adiabats  $<3$  is caused by laser imprint. The image on the cover and reproduced here shows a density contour plot of a low-adiabat ( $\alpha = 3$ ) implosion. The Rayleigh–Taylor growth seeded by laser imprints “shreds” the imploding shell.



This report was prepared as an account of work conducted by the Laboratory for Laser Energetics and sponsored by New York State Energy Research and Development Authority, the University of Rochester, the U.S. Department of Energy, and other agencies. Neither the above-named sponsors nor any of their employees makes any warranty, expressed or implied, or assumes any legal liability or responsibility for the accuracy, completeness, or usefulness of any information, apparatus, product, or process disclosed, or represents that its use would not infringe privately owned rights. Reference herein to any specific commercial product, process, or service by trade name, mark, manufacturer, or otherwise, does not necessarily constitute or imply its endorsement, recommendation, or favoring

by the United States Government or any agency thereof or any other sponsor. Results reported in the LLE Review should not be taken as necessarily final results as they represent active research. The views and opinions of authors expressed herein do not necessarily state or reflect those of any of the above sponsoring entities.

The work described in this volume includes current research at the Laboratory for Laser Energetics, which is supported by New York State Energy Research and Development Authority, the University of Rochester, the U.S. Department of Energy Office of Inertial Confinement Fusion under Cooperative Agreement No. DE-NA00001944, and other agencies.

Printed in the United States of America  
Available from

National Technical Information Services  
U.S. Department of Commerce  
5285 Port Royal Road  
Springfield, VA 22161  
[www.ntis.gov](http://www.ntis.gov)

For questions or comments, contact Wolfgang Theobald,  
Editor, Laboratory for Laser Energetics, 250 East River Road,  
Rochester, NY 14623-1299, (585) 273-2628.

[www.lle.rochester.edu](http://www.lle.rochester.edu)

# LLE Review

## Quarterly Report



### Contents

In Brief .....	iii
Measurements of the Effect of Adiabatic on Shell Decompression in Direct-Drive Implosions on OMEGA .....	109
Optical Smoothing of Laser Imprinting in Planar-Target Experiments on OMEGA EP Using One-Dimensional Multi-FM Smoothing by Spectral Dispersion.....	115
Plasma Characterization Using Ultraviolet Thomson Scattering from Ion-Acoustic and Electron Plasma Waves.....	125
Measurements of Hot-Electron Temperature in Laser-Irradiated Plasmas.....	134
A Pulse-Front-Tilt-Compensated Streaked Optical Spectrometer with High Throughput and Picosecond Time Resolution.....	143
Design of an Extreme Ultraviolet Spectrometer Suite to Characterize Rapidly Heated Solid Matter .....	146
Influence of Surface Modifications on the Adsorption and Absorption of Tritium into Stainless-Steel 316.....	150
Publications and Conference Presentations	



## In Brief

This volume of the LLE Review, covering April–June 2016, features “Measurements of the Effect of Adiabatic on Shell Decompression in Direct-Drive Implosions on OMEGA,” by D. T. Michel, S. X. Hu, A. K. Davis, V. Yu. Glebov, V. N. Goncharov, I. V. Igumenshchev, P. B. Radha, C. Stoeckl, and D. H. Froula. This article (p. 109) reports on measurements of the maximum in-flight shell thickness, which decreased from  $75 \pm 2 \mu\text{m}$  to  $60 \pm 2 \mu\text{m}$  in direct-drive implosions on OMEGA when the shell adiabat was reduced from 6 to 4.5. When the adiabat was decreased further (to  $\alpha = 1.8$ ), the shell thickness increased to  $75 \pm 2 \mu\text{m}$ . Two-dimensional simulations that included laser imprint, nonlocal thermal transport, cross-beam energy transfer, and first-principles equation-of-state models reproduced the measured shell thickness, shell trajectories, minimum core radius, and neutron yield and showed that the increased shell thickness for  $\alpha \leq 3$  was caused by laser imprint.

Additional research highlights presented in this issue include:

- M. Hohenberger, A. Shvydky, J. A. Marozas, G. Fiksel, M. J. Bonino, D. Canning, T. J. B. Collins, C. Dorrer, T. J. Kessler, B. E. Kruschwitz, P. W. McKenty, D. D. Meyerhofer, S. P. Regan, T. C. Sangster, and J. D. Zuegel demonstrate optical smoothing of laser imprinting in planar-target experiments on OMEGA EP using one-dimensional (1-D) multi-FM smoothing by spectral dispersion (SSD) (p. 115). Direct-drive ignition at the National Ignition Facility (NIF) requires single-beam smoothing to minimize imprinting of laser nonuniformities that can negatively affect implosion performance. One-dimensional, multi-FM SSD has been proposed to provide the required smoothing. A prototype multi-FM SSD system has been integrated into the NIF-like beamline of the OMEGA EP Laser System. Experiments have been performed to verify the smoothing performance by measuring Rayleigh–Taylor growth rates in planar targets of laser-imprinted and preimposed surface modulations. One-dimensional, multi-FM SSD has been observed to reduce imprint levels by  $\sim 50\%$  compared to the nominal OMEGA EP SSD system. The experimental results are in agreement with 2-D *DRACO* simulations using realistic, time-dependent far-field spot-intensity calculations that emulate the effect of SSD.
- R. K. Follett, J. A. Delettrez, D. H. Edgell, R. J. Henchen, J. Katz, J. F. Myatt, and D. H. Froula discuss plasma characterization using ultraviolet Thomson scattering from ion-acoustic and electron plasma waves (p. 125). Collective Thomson scattering is a technique for measuring the plasma conditions in laser-plasma experiments. Simultaneous measurements of ion-acoustic and electron plasma wave spectra were obtained using a 263.25-nm Thomson-scattering probe beam. A fully reflective collection system was used to record light scattered from electron plasma waves at electron densities greater than  $10^{21} \text{ cm}^{-3}$ , which produced scattering peaks near 200 nm. An accurate analysis of the experimental Thomson-scattering spectra required accounting for plasma gradients, instrument sensitivity, optical effects, and background radiation. Practical techniques for including these effects when fitting Thomson-scattering spectra are presented and applied to the measured spectra to show the improvement in plasma characterization.
- A. A. Solodov, B. Yaakobi, D. H. Edgell, R. K. Follett, J. F. Myatt, C. Sorce, and D. H. Froula describe measurements of hot-electron temperature in laser-irradiated plasmas (p. 134). In recently published work they reported on measuring the total energy of hot electrons produced by the interaction of a nanosecond laser with planar CH-coated molybdenum targets, using Mo  $K_{\alpha}$  emission. The temperature of the hot electrons in that work was determined by the high-energy bremsstrahlung spectrum measured by a three-channel fluorescence-photomultiplier hard x-ray detector (HXRD). In the present work, which extends that temperature measurement, the HXRD was replaced with a nine-channel image-plate-based detector.

For the same conditions (irradiance of the order of  $10^{14}$  W/cm<sup>2</sup>; 2-ns pulses) the measured temperatures were consistently lower than those measured by the HXR (by a factor  $\sim 1.5$  to  $1.7$ ). This measurement was supplemented with three experiments that measure the hot-electron temperature using  $K_{\alpha}$  emission from high-Z target layers, independent of the hard x-ray emission. These experiments yielded temperatures that were consistent with those measured by the bremsstrahlung. For a given x-ray emission in inertial confinement fusion compression experiments, this result would lead to a higher total energy in hot electrons, but to a lower preheat of the compressed fuel, because of the reduced hot-electron range.

- J. Katz, R. Boni, R. Rivlis, and D. H. Froula (LLE); and C. Muir (Department of Mechanical Engineering, University of Rochester) report on a pulse-front-tilt-compensated streaked optical spectrometer with high throughput and picosecond time resolution (p. 143). A high-throughput, broadband optical spectrometer coupled to the Rochester Optical Streak System equipped with a Photonis P820 streak tube was designed to record time-resolved spectra with 1-ps time resolution. Spectral resolution of 0.8 nm is achieved over a wavelength coverage range of 480 to 580 nm, using a 300-groove/mm diffraction grating in conjunction with a pair of 225-mm-focal-length doublets operating at an  $f/2.9$  aperture. Overall pulse-front tilt across the beam diameter generated by the diffraction grating is reduced by preferentially delaying discrete segments of the collimated input beam using a 34-element reflective echelon optic. The introduced delay temporally aligns the beam segments and the net pulse-front tilt is limited to the accumulation across an individual subelement. The resulting spectrometer design balances resolving power and pulse-front tilt while maintaining high throughput.
- S. T. Ivancic, C. R. Stillman, D. Nelson, I. A. Begishev, C. Mileham, P. M. Nilson, and D. H. Froula present a design of an extreme ultraviolet spectrometer suite to characterize rapidly heated solid matter (p. 146). An ultrafast, streaked, extreme-ultraviolet (XUV) spectrometer (5 to 20 nm) has been developed to measure the temperature dynamics in rapidly heated samples. Rapid heating makes it possible to create exotic states of matter that can be probed during their inertial confinement time—tens of picoseconds in the case of micron-sized targets. In contrast to other forms of pyrometry, where the temperature is inferred from bulk x-ray emission, XUV emission is restricted to the sample surface, allowing for a temperature measurement at the material–vacuum interface. The surface-temperature measurement constrains models for the release of high-energy-density material. Coupling the XUV spectrometer to an ultrafast ( $<2$ -ps) streak camera provided an evolution in the picosecond time scale of the surface-layer emission. Two high-throughput XUV spectrometers were designed to simultaneously measure the time-resolved and absolute XUV emission.
- M. Sharpe, C. Fagan, and W. T. Shmayda (LLE); and W. U. Schröder (Department of Chemistry, University of Rochester) discuss the influence of surface modifications on the adsorption and absorption of tritium into stainless-steel 316 (p. 150). Tritium dissolution within the adsorbed water layers on stainless-steel surfaces can contribute a significant fraction to the total quantity of tritium absorbed during an exposure to tritium-containing gas. Additionally, these water layers govern the migration of tritium from the stainless-steel lattice to the metal surface after the surface is cleaned. The adsorbed water layers are sensitive to the conditions of the metal surface; different pretreatments can lead to different surface concentrations of water. In the present study, the effect of altering the metal surface by mechanical polishing, electropolishing, Fe or Cr oxidation, gold plating, and nitric-acid treatments was studied using linear thermal desorption and plasma-induced ion sputtering. The results demonstrate that altering the metal surface can reduce tritium absorption by  $\geq 35\%$ . Finally, a quantitative migration model accurately describes the migration of tritium out of the stainless-steel lattice after the surface is cleaned.

Wolfgang Theobald  
*Editor*

---

# Measurements of the Effect of Adiatat on Shell Decompression in Direct-Drive Implosions on OMEGA

In inertial confinement fusion (ICF), laser beams are used to implode a spherical shell of deuterium and tritium. To reach maximum compression and achieve fusion conditions, the fuel entropy must be minimized (close to the Fermi-degenerated limit).<sup>1,2</sup> This requires accurate control of the shocks and compression waves launched during the implosion.<sup>3</sup> The entropy in ICF is commonly characterized by the shell's adiabat ( $\alpha$ ) defined as the mass-averaged ratio of the shell's pressure to the Fermi-degenerated pressure.<sup>4,5</sup> One-dimensional (1-D) simulations suggest that reducing the adiabat increases the shell density and reduces shell thickness. At a low adiabat, however, short-scale nonuniformities amplified by the Rayleigh–Taylor (RT) instability lead to shell decompression, which increases its effective adiabat.<sup>5–9</sup> Therefore, optimizing the implosion performance requires a balance between minimizing the adiabat and reducing the RT growth to maintain a compressible shell.

The effect of the adiabat on shell compression has typically been studied by measuring its effect on integrated performance parameters (e.g., neutron yield and areal density). Recently, several studies have shown that increasing the adiabat of the shell improved the neutron yield in both direct-<sup>10,11</sup> and indirect-drive<sup>12,13</sup> configurations. For low-adiabat implosions, the nonuniformities were shown to result in the ablator mixing into the hot spot, which cooled the hot spot and reduced the fusion performance.<sup>14,15</sup> A threshold was observed in the calculated adiabat where, above the threshold, the measured areal density was recovered by 1-D simulations.<sup>16</sup> Previous research aimed at studying integrated implosions has used flux-limiter models,<sup>11,17–19</sup> but these models did not reproduce the mass ablation rate and the conduction-zone length correctly, which led to errors in the calculation of the laser imprint and the RT growth.<sup>20</sup>

This article presents the first measurements of the effect of adiabat on the shell decompression and the first hydrodynamic simulations<sup>21</sup> that reproduce the detailed experimental observables by including laser imprint<sup>17</sup> and cross-beam energy transfer (CBET)<sup>22</sup> models. The maximum in-flight shell thickness was obtained using a novel technique where the outer and inner surfaces of the shell were simultaneously

measured using self-emission images of the imploding target. When the calculated adiabat of the shell was decreased from  $\alpha = 6$  to  $\alpha = 4.5$ , the shell thickness was measured to decrease from  $75 \pm 2 \mu\text{m}$  to  $60 \pm 2 \mu\text{m}$ , but when the adiabat was decreased further to  $\alpha = 1.8$ , the shell thickness was measured to increase to  $75 \pm 2 \mu\text{m}$ . Over this adiabat range, the measured minimum core size continued to decrease, demonstrating that the decompression of the shell measured for low adiabats was not caused by errors in the adiabat calculations, but a result of the increase in the RT growth. The optimum performance (minimum shell thickness and maximum neutron yield) was obtained for  $\alpha = 3$ . In simulations that did not include laser imprint, the simulated thicknesses were close to measurements for  $\alpha > 3$ , but they significantly underestimated the shell thickness for  $\alpha \leq 3$ , which confirmed that the decompression measured for low adiabats was a result of laser imprint. The simulations that included state-of-the-art models reproduce the measured outer-shell trajectory, maximum in-flight shell thicknesses, inner-shell deceleration, minimum core size, and neutron yields and show that the increased shell thickness for  $\alpha \leq 3$  is caused by laser imprint.

The experiments employed 60 ultraviolet ( $\lambda_0 = 351 \text{ nm}$ ) laser beams on the OMEGA laser.<sup>23</sup> The laser beams uniformly illuminated the target and were smoothed by polarization smoothing,<sup>24</sup> smoothing by spectral dispersion (SSD),<sup>25</sup> and distributed phase plates (fourth-order super-Gaussian with 95% of the energy contained within the initial target diameter).<sup>26</sup> On some shots, the laser imprint was increased by turning off SSD. A 100-ps-long picket and a  $1.7 \pm 0.2 \times 10^{14} \text{ W/cm}^2$  foot on the rise of the drive pulse were used to set the adiabat of the shell.<sup>9</sup> They were followed by a 2-ns-long drive pulse that accelerated the target to its final velocity of  $\sim 200 \text{ km/s}$ . The picket intensity was varied between  $0.85 \times 10^{14} \text{ W/cm}^2$  and  $5.5 \times 10^{14} \text{ W/cm}^2$  to vary the adiabat of the shell between 1.8 and 6. The total laser energy was  $21 \pm 0.3 \text{ kJ}$ , which resulted in a maximum on-target overlapped intensity of  $4.7 \pm 0.06 \times 10^{14} \text{ W/cm}^2$ . The shells were made of  $26.5 \pm 0.2 \text{ }\mu\text{m}$ -thick glow-discharge polymer (CH with a density of  $1.03 \text{ g/cm}^3$ ) with an outer radius of  $433 \pm 4 \text{ }\mu\text{m}$  and filled with  $11 \pm 0.5 \text{ atm}$  of deuterium.

The recently developed self-emission x-ray imaging technique<sup>27</sup> was adapted to simultaneously measure the outer- and inner-shell trajectories (Fig. 147.1). The soft x rays emitted by the imploding target were imaged with an array of 10- $\mu\text{m}$ -diam pinholes onto a four-strip, fast x-ray framing camera<sup>28</sup> using a magnification of 6. With this setup, the point-spread function (PSF) of the diagnostic had a diameter at full width at half maximum of  $d_{\text{PSF}} = 12 \mu\text{m}$ . The images were integrated over 40 ps. A 25.4- $\mu\text{m}$ -thick Be filter was used to select the soft x rays above  $\sim 1 \text{ keV}$ . The absolute timing between the laser pulse and the images was known to an accuracy of 20 ps and the interstrip timing was determined within 5 ps (Refs. 29 and 30).

Figure 147.1(c) shows the x-ray self-emission profile at the beginning of the deceleration of the shell calculated by post-processing the hydrodynamic simulations [Fig. 147.1(b)] with *Spect3D*.<sup>31</sup> The inner edge of the outer peak generated by the coronal plasma was used to determine the position of the outer surface of the shell, while the outer edge of the central emission (hot spot) was used to determine the position of the inner surface of the shell. The emission of the coronal plasma is maximum near the outer surface of the shell because the plasma has a larger density and the integration distance to the detector is maximum. Just inside the outer surface of the shell, the emission drops by a factor of 2 over a few microns as the emission from the back of the target is absorbed into the cold shell. When the shell begins to decelerate, the pressure of the hot spot rapidly increases ( $P_{\text{hs}} \propto 1/R^5$ ), resulting in an increase

in the electron temperature and a rapid start of the emission of x rays from the hot spot with energies above 1 keV. The maximum emission occurs close to the inner edge of the shell, where the shell is ablated and the plasma has a high density. To account for the PSF of the diagnostic, the edge position is measured using the 10% intensity point [ $0.1 \times (I_{\text{max}} - I_{\text{min}}) + I_{\text{min}}$ , where  $I_{\text{max}}$  and  $I_{\text{min}}$  are the maximum and minimum emissions inside the coronal emission]. During the deceleration phase, this outer edge corresponds to the inner side of the cold shell where the temperature drops below 400 eV.

Figure 147.2 shows the self-emission images measured at the end of the laser pulse and at maximum compression. Accurate measurements of the positions of the outer- and inner-shell radii were obtained by averaging the positions of the inner edge of the outer peak and the outer edge of the hot-spot emission determined at each angle. To reduce the noise, self-emission images were angularly averaged over the spatial resolution of the diagnostic ( $\theta_{\text{avg}} = d_{\text{PSF}}/R \approx 20^\circ$ , where  $R$  is either the outer- or inner-shell radius). With this method, the standard deviation in the variation (as a function of the angle) of the position of the outer edge (inner edge) of the shell was  $\sigma_{\text{outer}} = \pm 2 \mu\text{m}$  ( $\sigma_{\text{inner}} = \pm 3 \mu\text{m}$ ), resulting in an error in the  $360^\circ$  averaged radius of  $\delta R_{\text{outer}} = \sigma_{\text{outer}}/\sqrt{N_p} \approx 0.2 \mu\text{m}$  (Ref. 30) ( $\delta R_{\text{inner}} \approx \pm 0.5 \mu\text{m}$ ), where  $N_p = 2\pi R/d_{\text{PSF}}$  is the number of independent measurements and  $R$  is the averaged radius. To measure the inner-shell radius, an additional error was introduced by the difference between the 10% intensity point and the inner radius. A maximum error of  $\sim 2 \mu\text{m}$  was determined

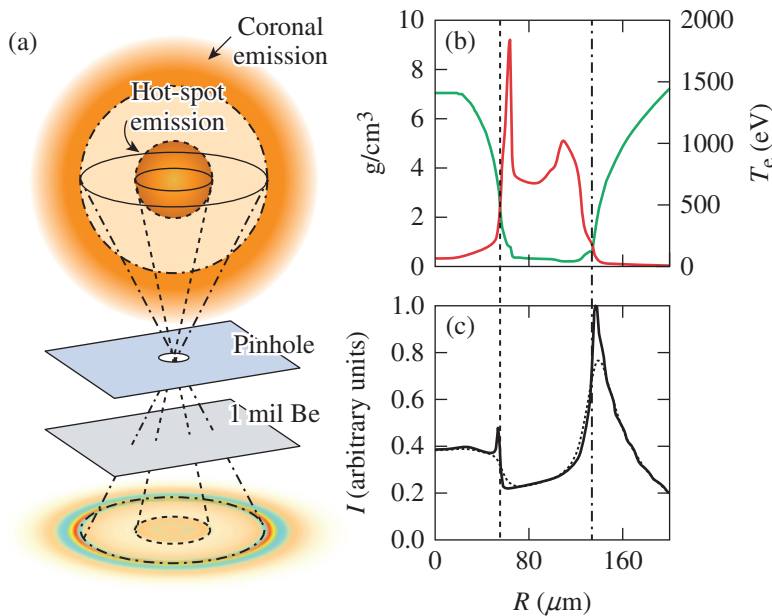
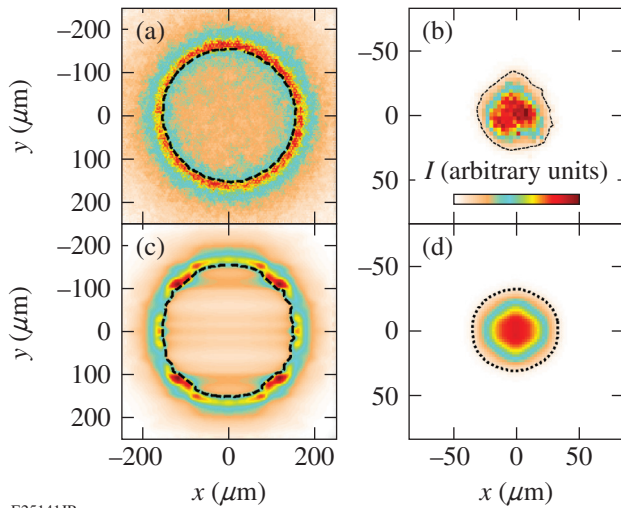


Figure 147.1

(a) The x-ray emission above 1 keV from the coronal plasma and the hot spot was imaged by a pinhole through a Be filter and measured by an x-ray framing camera. A synthetic image calculated for an implosion with an adiabat of 6 is shown. (b) The temperature (green curve) and density profiles (red curve) of the target are compared with the (c) self-emission profiles measured at the diagnostic plane with (dotted curve) and without (solid curve) convolving with the point-spread function (PSF) of the diagnostic. The positions of the outer (dashed-dotted vertical lines) and inner shell (dashed vertical lines) are indicated.

E25140JR



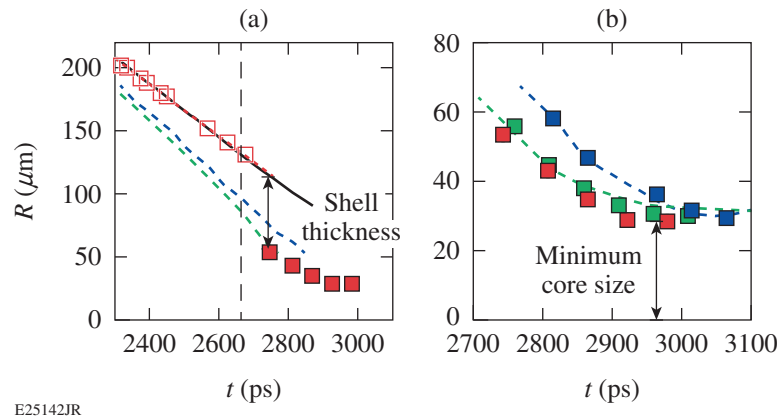
E25141JR

Figure 147.2

Comparisons of the [(a),(b)] measured and [(c),(d)] calculated self-emission images at the end of the laser pulse (2.6 ns) and at the maximum compression (3 ns), respectively. The positions of the [(a),(c)] outer and [(b),(d)] inner shell are shown as dashed black lines and dotted black lines, respectively.

by comparing those two quantities in hydrodynamic simulations performed with and without nonuniformities (Fig. 147.3).

Figure 147.3 shows the simultaneous measurement of the outer and inner surfaces of the shell, which determined the maximum in-flight shell thickness, the deceleration of the shell,



E25142JR

Figure 147.3

(a) The thickness of the shell was determined by the distance between the outer-shell radius (open squares) extrapolated with a constant velocity (short dashed red line) and the inner-shell radius (solid squares) at the time when the hot spot first emits x rays. Once the laser turned off (long black dashed line), the position of the outer surface was determined by extrapolating the measured outer-shell trajectory along a free-fall line. The inner surface trajectory at  $1/e$  of the maximum density was calculated from a simulation without laser imprint (dashed blue curve) and with laser imprint (dashed green curve). For the two simulations, the outer-shell trajectories at 0.2 of the maximum are the same (black curve) and are in excellent agreement with measurements. (b) The measured inner-surface trajectories (red squares) are compared with a 2-D simulations with (green squares) and without (blue squares) laser imprint. The trajectories of the surface where the hot-spot electron temperature drops below 400 eV is plotted for both simulations (dashed curves). The laser beams were smoothed by smoothing by spectral dispersion (SSD) and drove the implosion with  $\alpha = 3$ , which is slightly larger than the adiabat in the simulation (+2.5) because of the experimental reproducibility.

and the minimum core size. Once the laser turned off, the position of the outer surface was determined by extrapolating the measured outer-shell trajectory along a free-fall line. During this time (up to 70 ps), the target was not accelerated by the laser and it imploded with a constant velocity (simulations show that at this time convergence effects are negligible). The 4% error in the measurement of the velocity of the outer shell<sup>30</sup> resulted in a maximum error of  $\pm 1 \mu\text{m}$  in the inferred outer-shell radius at the beginning of the core emission.

Figure 147.4(a) shows that when SSD was used, the maximum in-flight shell thickness was measured to decrease from  $75 \mu\text{m}$  to  $60 \mu\text{m}$  when the adiabat was decreased from  $\alpha = 6$  to  $\alpha = 4.5$ , but when the adiabat was reduced to  $\alpha = 1.8$ , the thickness of the shell increased to  $75 \mu\text{m}$ . This is not consistent with the reduction of the shell's adiabat. For each experiment, the measured outer-shell trajectory was nearly identical, indicating that the ablation pressure was similar among these shots. This increase in shell thickness is not explained by an error in the adiabat calculation because the measured minimum core size continued to decrease as the adiabat was reduced [Fig. 147.4(b)] and the neutron yield was up to  $5\times$  larger for the lower-adiabat ( $\alpha = 1.8$  to  $\alpha = 3$ ) implosions compared with the higher-adiabat ( $\alpha = 4.5$  to  $\alpha = 6$ ) implosions [Fig. 147.4(c)]. This is consistent with previous observations that showed a mild reduction in the areal density measured at maximum neutron yield compared to 1-D simulations at low adiabat.<sup>11</sup> The measured increase in

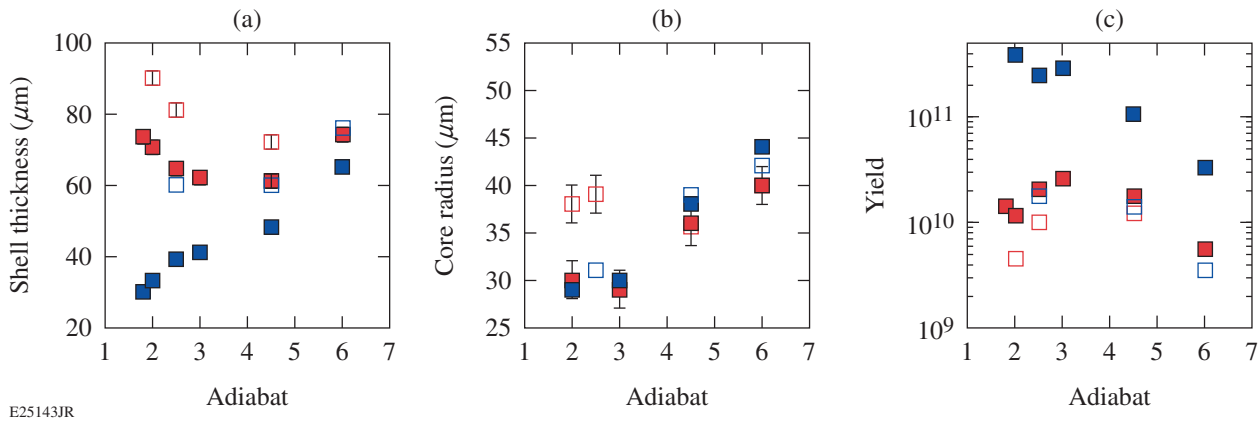


Figure 147.4

(a) The measured shell thicknesses at the beginning of the core emission, (b) core radii at maximum compression, and (c) neutron yields were compared for the different adiabats with (solid red points) and without (open red points) SSD. The corresponding simulations with (open blue squares) and without imprint (solid blue squares) are shown.

the shell thickness for low-adiabat implosions was consistent with an increase in the RT growth that resulted in larger shell nonuniformities, which decompressed the shell.

To understand the shell decompression measured for low-adiabat implosions, hydrodynamic simulations were performed with the 2-D hydrodynamic code *DRACO*<sup>17</sup> using the current state-of-the-art models for nonlocal thermal transport,<sup>32,33</sup> CBET, first-principles equation of state,<sup>34</sup> and laser imprint (including modes between 2 and 200). To resolve both CBET and laser imprint, each simulation required approximately three months of computational time on  $\sim 300$  cores. Only the shell nonuniformities caused by laser imprint were simulated because the RT growth is dominant for large modes ( $>100$ ) and the perturbations caused by target roughness are smaller by about a factor of 10 than those imposed by imprint. For all simulations, the trajectory of the outer surface of the shell was well reproduced, indicating that the hydrodynamic efficiency was correctly modeled.<sup>29</sup> Simulations were able to reproduce the maximum in-flight shell thickness, inner-shell deceleration, minimum core size, and neutron yield (Figs. 147.3 and 147.4). This excellent agreement for  $\alpha \leq 3$  suggests that the shell decompression measured for low-adiabat implosions was caused by laser imprint. For larger-adiabat implosions, the excellent agreement shows that the reduction in the RT growth with the shell adiabat was correctly modeled. For the lowest-adiabat ( $\alpha \leq 2$ ) implosions, the simulated shell was broken in-flight, which produced a nonphysical hole (i.e., ring) in the shell as a result of the 2-D symmetry. This resulted in a large increase in the final core size and a strong reduction in neutron yield.

The fact that the final core size was significantly smaller for lower-adiabat implosions, even when the maximum in-flight shell thickness was similar, is a result of the laser imprint primarily decompressing the outer surface of the shell. The inner-shell density, and therefore the inner-shell pressure, remained large, leading to a small final core radius.<sup>10</sup> Furthermore, the core pressure was reduced slightly by the RT-induced mix of the CH into the  $\text{D}_2$  core, allowing the shell to converge further. For the larger-adiabat implosions, the shell thickness increased because of increased shock heating, resulting in a smaller convergence.

Figure 147.4 shows that hydrodynamic simulations performed without laser imprint (1-D-like) are in better agreement with measurements for high-adiabat shots, but they significantly underestimate the shell thickness for low-adiabat implosions. For  $\alpha \leq 3$ , these simulations predict that the shell thickness continues to decrease contrary to the experiments. This confirms that the laser imprint causes the decompression of the shell. This increased decompression resulted in an increasing difference between the measured and calculated neutron yields [Fig. 147.4(c)].

When the laser imprint was increased by turning SSD off, the thickness of the shell was increased by  $\sim 25\%$ , leading to a reduced neutron yield for each adiabat tested (Fig. 147.4). Compared to SSD-on shots, a weaker degradation of the implosion performances (smaller increase of the core size and smaller reduction in neutron yield) was obtained for a larger adiabat ( $\alpha = 4.5$ ) than for a lower adiabat ( $\alpha = 2.5$  and  $\alpha = 2$ ). This is a result of the larger laser imprint that required a stronger mitigation of the RT growth to keep the shell compressible.

In summary, the decompression of an imploding shell was studied by measuring the maximum in-flight shell thicknesses for adiabats ranging from 1.8 to 6 and comparing the results with the first 2-D hydrodynamic simulations, which included laser imprint, nonlocal thermal transport, CBET, and first-principles equation-of-state models. When the adiabat of the shell was decreased, the shell thickness was initially measured to decrease. Reducing the adiabat below 3 resulted in an increasing shell thickness. Over this adiabat scan, the measured minimum core size continued to decrease, showing that the decompression of the shell measured for low adiabats was not caused by errors in the adiabat calculations but by an increase in the RT growth. Hydrodynamic simulations reproduced the measured outer-shell trajectory, maximum in-flight shell thicknesses, inner-shell deceleration, minimum core size, and neutron yields. Simulations that did not include laser imprint were in good agreement with measurements for  $\alpha > 3$ , but they significantly underestimated the shell thickness for  $\alpha \leq 3$ , which confirmed that the decompression measured for low adiabats was a result of laser imprint.

#### ACKNOWLEDGMENT

This work was supported by the U.S. Department of Energy Office of Inertial Confinement Fusion under Award Number DE-NA0001944, the University of Rochester, and the New York State Energy Research and Development Authority. The support of DOE does not constitute an endorsement by DOE of the views expressed in this article.

#### REFERENCES

1. M. C. Herrmann, M. Tabak, and J. D. Lindl, *Phys. Plasmas* **8**, 2296 (2001).
2. R. Betti, K. Anderson, V. N. Goncharov, R. L. McCrory, D. D. Meyerhofer, S. Skupsky, and R. P. J. Town, *Phys. Plasmas* **9**, 2277 (2002).
3. J. Nuckolls *et al.*, *Nature* **239**, 139 (1972).
4. J. D. Lindl, *Inertial Confinement Fusion: The Quest for Ignition and Energy Gain Using Indirect Drive* (Springer-Verlag, New York, 1998).
5. S. E. Bodner, D. G. Colombant, J. H. Gardner, R. H. Lehmborg, S. P. Obenshain, L. Phillips, A. J. Schmitt, J. D. Sethian, R. L. McCrory, W. Seka, C. P. Verdon, J. P. Knauer, B. B. Afeyan, and H. T. Powell, *Phys. Plasmas* **5**, 1901 (1998).
6. S. E. Bodner, *Phys. Rev. Lett.* **33**, 761 (1974).
7. V. N. Goncharov, R. Betti, R. L. McCrory, P. Sorotokin, and C. P. Verdon, *Phys. Plasmas* **3**, 1402 (1996).
8. V. N. Goncharov, J. P. Knauer, P. W. McKenty, P. B. Radha, T. C. Sangster, S. Skupsky, R. Betti, R. L. McCrory, and D. D. Meyerhofer, *Phys. Plasmas* **10**, 1906 (2003).
9. V. N. Goncharov, T. C. Sangster, T. R. Boehly, S. X. Hu, I. V. Igumenshchev, F. J. Marshall, R. L. McCrory, D. D. Meyerhofer, P. B. Radha, W. Seka, S. Skupsky, C. Stoeckl, D. T. Casey, J. A. Frenje, and R. D. Petrasso, *Phys. Rev. Lett.* **104**, 165001 (2010).
10. V. N. Goncharov, T. C. Sangster, R. Betti, T. R. Boehly, M. J. Bonino, T. J. B. Collins, R. S. Craxton, J. A. Delettrez, D. H. Edgell, R. Epstein, R. K. Follet, C. J. Forrest, D. H. Froula, V. Yu. Glebov, D. R. Harding, R. J. Henchen, S. X. Hu, I. V. Igumenshchev, R. Janezic, J. H. Kelly, T. J. Kessler, T. Z. Kosc, S. J. Loucks, J. A. Marozas, F. J. Marshall, A. V. Maximov, R. L. McCrory, P. W. McKenty, D. D. Meyerhofer, D. T. Michel, J. F. Myatt, R. Nora, P. B. Radha, S. P. Regan, W. Seka, W. T. Shmayda, R. W. Short, A. Shvydky, S. Skupsky, C. Stoeckl, B. Yaakobi, J. A. Frenje, M. Gatu-Johnson, R. D. Petrasso, and D. T. Casey, *Phys. Plasmas* **21**, 056315 (2014).
11. P. B. Radha, C. Stoeckl, V. N. Goncharov, J. A. Delettrez, D. H. Edgell, J. A. Frenje, I. V. Igumenshchev, J. P. Knauer, J. A. Marozas, R. L. McCrory, D. D. Meyerhofer, R. D. Petrasso, S. P. Regan, T. C. Sangster, W. Seka, and S. Skupsky, *Phys. Plasmas* **18**, 012705 (2011).
12. O. A. Hurricane *et al.*, *Nature* **506**, 343 (2014).
13. H. S. Park *et al.*, *Phys. Rev. Lett.* **112**, 055001 (2014).
14. S. P. Regan, R. Epstein, B. A. Hammel, L. J. Suter, J. Ralph, H. Scott, M. A. Barrios, D. K. Bradley, D. A. Callahan, C. Cerjan, G. W. Collins, S. N. Dixit, T. Doeppner, M. J. Edwards, D. R. Farley, S. Glenn, S. H. Glenzer, I. E. Golovkin, S. W. Haan, A. Hamza, D. G. Hicks, N. Izumi, J. D. Kilkenny, J. L. Kline, G. A. Kyrala, O. L. Landen, T. Ma, J. J. MacFarlane, R. C. Mancini, R. L. McCrory, N. B. Meezan, D. D. Meyerhofer, A. Nikroo, K. J. Peterson, T. C. Sangster, P. Springer, and R. P. J. Town, *Phys. Plasmas* **19**, 056307 (2012).
15. T. Ma, P. K. Patel, N. Izumi, P. T. Springer, M. H. Key, L. J. Atherton, L. R. Benedetti, D. K. Bradley, D. A. Callahan, P. M. Celliers, C. J. Cerjan, D. S. Clark, E. L. Dewald, S. N. Dixit, T. Döppner, D. H. Edgell, R. Epstein, S. Glenn, G. Grim, S. W. Haan, B. A. Hammel, D. Hicks, W. W. Hsing, O. S. Jones, S. F. Khan, J. D. Kilkenny, J. L. Kline, G. A. Kyrala, O. L. Landen, S. Le Pape, B. J. MacGowan, A. J. Mackinnon, A. G. MacPhee, N. B. Meezan, J. D. Moody, A. Pak, T. Parham, H.-S. Park, J. E. Ralph, S. P. Regan, B. A. Remington, H. F. Robey, J. S. Ross, B. K. Spears, V. Smalyuk, L. J. Suter, R. Tommasini, R. P. Town, S. V. Weber, J. D. Lindl, M. J. Edwards, S. H. Glenzer, and E. I. Moses, *Phys. Rev. Lett.* **111**, 085004 (2013).
16. T. C. Sangster, V. N. Goncharov, R. Betti, P. B. Radha, T. R. Boehly, D. T. Casey, T. J. B. Collins, R. S. Craxton, J. A. Delettrez, D. H. Edgell, R. Epstein, C. J. Forrest, J. A. Frenje, D. H. Froula, M. Gatu-Johnson, V. Yu. Glebov, D. R. Harding, M. Hohenberger, S. X. Hu, I. V. Igumenshchev, R. Janezic, J. H. Kelly, T. J. Kessler, C. Kingsley, T. Z. Kosc, J. P. Knauer, S. J. Loucks, J. A. Marozas, F. J. Marshall, A. V. Maximov, R. L. McCrory, P. W. McKenty, D. D. Meyerhofer, D. T. Michel, J. F. Myatt, R. D. Petrasso, S. P. Regan, W. Seka, W. T. Shmayda, R. W. Short, A. Shvydky, S. Skupsky, J. M. Soures, C. Stoeckl, W. Theobald, V. Versteeg, B. Yaakobi, and J. D. Zuegel, *Phys. Plasmas* **20**, 056317 (2013).
17. P. B. Radha, T. J. B. Collins, J. A. Delettrez, Y. Elbaz, R. Epstein, V. Yu. Glebov, V. N. Goncharov, R. L. Keck, J. P. Knauer, J. A. Marozas, F. J. Marshall, R. L. McCrory, P. W. McKenty, D. D. Meyerhofer, S. P. Regan, T. C. Sangster, W. Seka, D. Shvarts, S. Skupsky, Y. Srebro, and C. Stoeckl, *Phys. Plasmas* **12**, 056307 (2005).

18. S. X. Hu, P. B. Radha, J. A. Marozas, R. Betti, T. J. B. Collins, R. S. Craxton, J. A. Delettrez, D. H. Edgell, R. Epstein, V. N. Goncharov, I. V. Igumenshchev, F. J. Marshall, R. L. McCrory, D. D. Meyerhofer, S. P. Regan, T. C. Sangster, S. Skupsky, V. A. Smalyuk, Y. Elbaz, and D. Shvarts, *Phys. Plasmas* **16**, 112706 (2009).
19. S. X. Hu, V. N. Goncharov, P. B. Radha, J. A. Marozas, S. Skupsky, T. R. Boehly, T. C. Sangster, D. D. Meyerhofer, and R. L. McCrory, *Phys. Plasmas* **17**, 102706 (2010).
20. D. T. Michel, A. K. Davis, V. N. Goncharov, T. C. Sangster, S. X. Hu, I. V. Igumenshchev, D. D. Meyerhofer, W. Seka, and D. H. Froula, *Phys. Rev. Lett.* **114**, 155002 (2015).
21. S. X. Hu, D. T. Michel, A. K. Davis, R. Betti, P. B. Radha, E. M. Campbell, D. H. Froula, and C. Stoeckl, "Understanding the Effects of Laser Imprint on Plastic-Target Implosions on OMEGA," to be published in *Physics of Plasmas*.
22. J. A. Marozas and T. J. B. Collins, *Bull. Am. Phys. Soc.* **57**, 344 (2012).
23. T. R. Boehly, D. L. Brown, R. S. Craxton, R. L. Keck, J. P. Knauer, J. H. Kelly, T. J. Kessler, S. A. Kumpan, S. J. Loucks, S. A. Letzring, F. J. Marshall, R. L. McCrory, S. F. B. Morse, W. Seka, J. M. Soures, and C. P. Verdon, *Opt. Commun.* **133**, 495 (1997).
24. T. R. Boehly, V. A. Smalyuk, D. D. Meyerhofer, J. P. Knauer, D. K. Bradley, R. S. Craxton, M. J. Guardalben, S. Skupsky, and T. J. Kessler, *J. Appl. Phys.* **85**, 3444 (1999).
25. S. Skupsky, R. W. Short, T. Kessler, R. S. Craxton, S. Letzring, and J. M. Soures, *J. Appl. Phys.* **66**, 3456 (1989).
26. T. J. Kessler, Y. Lin, J. J. Armstrong, and B. Velazquez, *Proc. SPIE* **1870**, 95 (1993).
27. D. T. Michel, C. Sorce, R. Epstein, N. Whiting, I. V. Igumenshchev, R. Jungquist, and D. H. Froula, *Rev. Sci. Instrum.* **83**, 10E530 (2012).
28. D. K. Bradley, P. M. Bell, J. D. Kilkenny, R. Hanks, O. Landen, P. A. Jaanimagi, P. W. McKenty, and C. P. Verdon, *Rev. Sci. Instrum.* **63**, 4813 (1992).
29. D. T. Michel, V. N. Goncharov, I. V. Igumenshchev, R. Epstein, and D. H. Froula, *Phys. Rev. Lett.* **111**, 245005 (2013).
30. D. T. Michel, A. K. Davis, W. Armstrong, R. Bahr, R. Epstein, V. N. Goncharov, M. Hohenberger, I. V. Igumenshchev, R. Jungquist, D. D. Meyerhofer, P. B. Radha, T. C. Sangster, C. Sorce, and D. H. Froula, *High Power Laser Science and Engineering* **3**, e19 (2015).
31. J. J. MacFarlane *et al.*, *High Energy Density Phys.* **3**, 181 (2007).
32. G. P. Schurtz, Ph. D. Nicolaï, and M. Busquet, *Phys. Plasmas* **7**, 4238 (2000).
33. D. Cao, G. Moses, and J. Delettrez, *Phys. Plasmas* **22**, 082308 (2015).
34. S. X. Hu, L. A. Collins, V. N. Goncharov, J. D. Kress, R. L. McCrory, and S. Skupsky, *Phys. Rev. E* **92**, 043104 (2015).

---

# Optical Smoothing of Laser Imprinting in Planar-Target Experiments on OMEGA EP Using One-Dimensional Multi-FM Smoothing by Spectral Dispersion

## Introduction

One of the primary missions of the National Ignition Facility (NIF)<sup>1</sup> is to experimentally demonstrate ignition with inertial confinement fusion (ICF),<sup>2–4</sup> either by the indirect-drive (or x-ray-drive) approach, where laser beams heat the inside of a high-Z enclosure (“hohlraum”) in which an implosion capsule is placed,<sup>4</sup> or by the direct-drive approach, where a capsule is illuminated directly by the laser beams to launch the capsule implosion.<sup>5</sup> In ICF the stability of the shell that encases the fusion fuel during the implosion is a key determinant of achieving ignition. Achieving sufficient irradiation uniformity for a successful direct-drive-ignition experiment necessitates the use of single-beam smoothing. Typical requirements for direct-drive illumination are in excess of what is required for indirect-drive illumination since direct drive lacks the inherent smoothing of the radiation field as it flows from the hohlraum wall to the capsule.<sup>6–8</sup>

Shell stability is primarily degraded by the growth of hydrodynamic instabilities that cause both short- and long-wavelength modulations of the shell’s areal density. These modulations can result in shell breakup during the acceleration phase of the implosion or lead to a mixing of the cold shell material with the hot fuel,<sup>9</sup> quenching the fusion reactions and reducing target performance during the implosion’s deceleration phase. The dominant hydrodynamic instability is the Rayleigh–Taylor (RT) instability.<sup>10,11</sup> It develops during the acceleration phase of the fusion target as the cold dense shell material is accelerated by the hot, low-density blowoff plasma.

In direct-drive targets, initial perturbations that lead to RT growth are primarily seeded by target-surface roughness and nonuniformities of the incident laser intensity (“imprint”). Laser imprinting occurs because spatial variations in the laser intensity drive pressure variations into the target. This distorts the shock and ablation front and creates lateral mass flow in the shock-compressed material, resulting in mass modulations at the ablation surface of the driven target.<sup>12</sup> Various laser-smoothing techniques have been developed to reduce the level of imprinting. These include distributed phase plates

(DPP’s),<sup>13</sup> continuous-contour phase plates (CPP’s),<sup>14</sup> polarization smoothing,<sup>15</sup> induced spatial incoherence (ISI),<sup>16</sup> and smoothing by spectral dispersion (SSD).<sup>17</sup>

SSD varies the interference speckle pattern of a DPP- or CPP-focused laser beam on a shorter time scale than the characteristic hydrodynamic response time of the target, i.e., the imprinting time. This is achieved by adding bandwidth, typically of a few angstroms, to the fundamental laser frequency using an electro-optical modulator. Introducing spectral dispersion to the broadened-bandwidth light, which is focused by including a phase plate, causes the interference structure from beamlets originating at different phase-plate elements to vary in time. At any given moment, the intensity profile is highly modulated because of the interference pattern from the phase-plate-modulated wavefront, but the time-averaged intensity is smoothed.<sup>17</sup>

Some instability mitigation is provided by the SSD system currently installed on the NIF,<sup>18,19</sup> although the level of smoothing is less than that required for direct-drive-ignition experiments.<sup>8</sup> There are two potential paths to implementing SSD beam smoothing for direct-drive ignition on the NIF: (1) Two-dimensional (2-D) SSD, as currently used on the OMEGA laser,<sup>20</sup> has been shown to reduce single-beam irradiation non-uniformities to the few-percent level<sup>21</sup> and to efficiently suppress instability seeds.<sup>22</sup> Adding a comparable 2-D SSD system to the NIF would necessitate major modifications to the preamplifier modules (PAM’s) and require additional tripler crystals to convert the extra bandwidth.<sup>8,23</sup> (2) One-dimensional smoothing by spectral dispersion with multiple phase-modulation frequencies (1-D multi-FM SSD)<sup>24,25</sup> was developed at LLE as a more cost-effective and labor-efficient solution to providing the smoothing level required for the current NIF polar-direct-drive-ignition point design. It is compatible with the existing NIF Laser System, and modifications that are necessary to implement 1-D multi-FM SSD on the NIF are limited to fiber-based systems in the Master Oscillator Room, in addition to a new diffraction grating in the PAM.<sup>8</sup> Both 2-D SSD and 1-D multi-FM SSD are predicted to provide the smoothing required by the ignition design.

A prototype multi-FM seed source has been implemented in Beamline 4 of the OMEGA EP laser<sup>26</sup> to validate the predicted multi-FM performance. Amplifying and angularly dispersing the phase-modulated beam in a NIF PAM before injection into Beamline 4 ensures the compatibility of the multi-FM system with the NIF's front end.

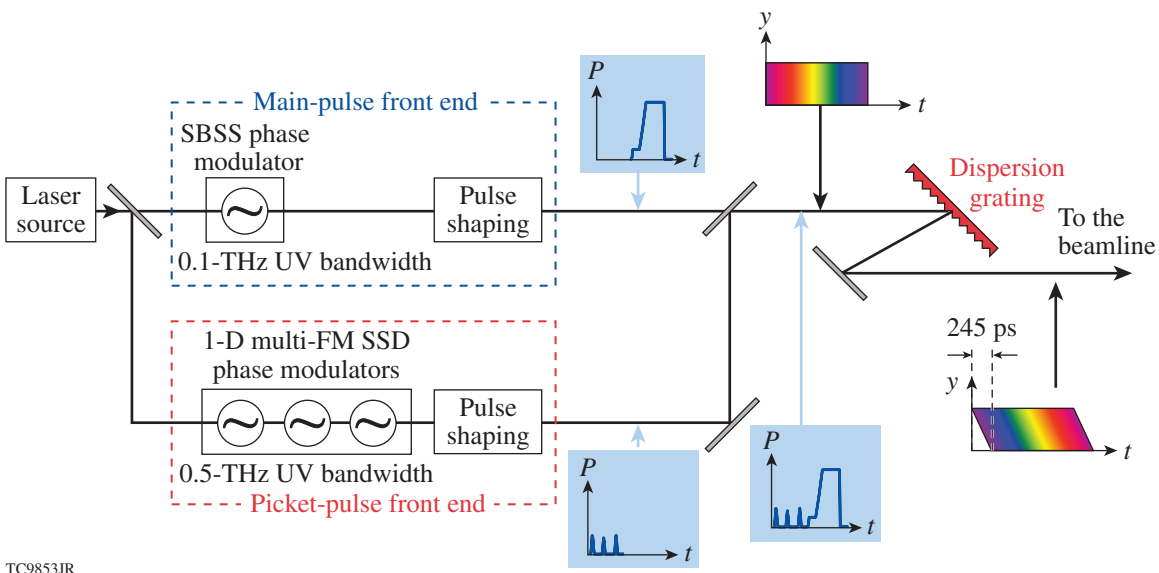
The multi-FM performance qualification consists of two parts: (1) measurement of equivalent-target-plane modulations of the laser intensity and (2) validation of the numerical treatment of 1-D multi-FM SSD to predict imprint levels and instability growth with dedicated on-target shots. The remaining sections briefly describe the multi-FM SSD system and its implementation on OMEGA EP; discuss the equivalent-target-plane measurements to characterize modulations in the focal-spot intensity using different SSD methods; describe the experiments that characterize laser-imprint levels by measuring the RT instability growth, including 2-D hydrodynamic simulations of the data; and present our conclusions.

### One-Dimensional Multi-FM SSD on OMEGA EP

The implementation of 1-D multi-FM SSD into the front end of Beamline 4 on OMEGA EP is shown schematically in Fig. 147.5. Two separate pulse-shaping systems provide different levels of SSD bandwidth to the laser pulse by transforming the incident electric field  $E(t) \propto \exp(i\omega_L t)$  to

$$E(t) \propto \exp\left[i\omega_L t + i\sum_n \delta_n \cos(\omega_n t + \varphi_n)\right]. \quad (1)$$

Here,  $\omega_L$  is the incident laser frequency;  $t$  is the time; and  $\delta_n$ ,  $\omega_n$ , and  $\varphi_n$  are the modulation depth, frequency, and phase of modulator  $n$ , respectively, with the sum being calculated over the number of modulators in the system. The OMEGA EP main-pulse front end introduces bandwidth to the fundamental laser frequency to suppress stimulated Brillouin scattering (SBSS SSD) in the laser system optics. It operates with a modulation frequency of 3 GHz and a modulation depth of 5.5 in the infrared (IR), resulting in a ultraviolet (UV) bandwidth of 0.1 THz. In parallel, a picket-pulse channel provides the bandwidth for the 1-D multi-FM SSD. It comprises three modulators with incommensurate frequencies of 21.2 GHz, 22.8 GHz, and 31.9 GHz and corresponding modulation depths of 0.45, 1.04, and 2.07, respectively. This results in a combined bandwidth in the UV of  $\sim 0.5$  THz. Multi-FM SSD is typically applied to the early part of the laser pulse during which laser imprint dominates, with SBSS SSD bandwidth applied to the main portion. The two parts are then optically combined to form the desired pulse shape and SSD bandwidth profile. This dynamic bandwidth reduction ensures that the increased bandwidth of multi-FM SSD is not applied during the high-intensity portion of the laser pulse, where it can potentially damage the laser optics.<sup>27</sup> After optical combination, the beam is passed through a diffraction grating, resulting in



TC9853JR

Figure 147.5

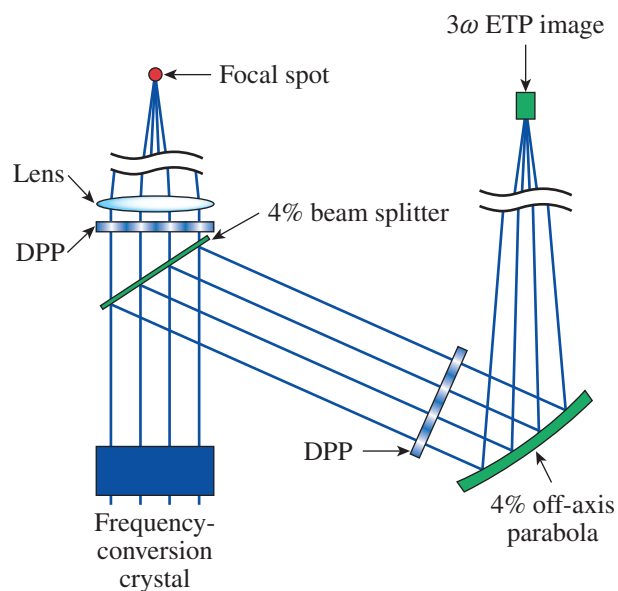
One-dimensional multi-FM setup of Beamline 4 on OMEGA EP. Two separate front ends provide bandwidth for either stimulated Brillouin scattering suppression (SBSS) or multi-FM smoothing by spectral dispersion (SSD). The two pulses are then combined optically to form the desired pulse shape and SSD profile. A grating introduces spectral dispersion, resulting in a spatiotemporal shear of 245 ps.

spectral dispersion of the phase-modulated beam and the spatial frequency modulation across the beam necessary for SSD. The grating imposes an uncompensated spatiotemporal shear of  $\Delta t = 245$  ps to the pulse. Since the NIF laser's front end, for which multi-FM has been designed, is a fiber-based system, it is not possible to place an additional grating in the laser chain before the phase modulators to compensate for this temporal skew. This imposes a minimum rise time of  $\sim 250$  ps to the portion of the laser pulse to which the multi-FM bandwidth is applied.

For the experiments discussed below, the pulse shapes were generated fully in either the SBSS or the multi-FM SSD front end, without employing dynamic bandwidth reduction.

### Equivalent-Target-Plane Measurements

High-resolution, equivalent-target-plane (ETP) measurements of the UV irradiation uniformity of SSD-smoothed laser pulses were performed using the setup shown in Fig. 147.6. The setup is very similar to the UV ETP system on OMEGA, which has been demonstrated to fully resolve individual speckles.<sup>28</sup> After frequency conversion and before focusing into the target chamber, a portion of the Beamline 4 light is picked up using a 4% beam splitter and focused onto a camera with an off-axis parabola. This provides an image of the focal spot equivalent to the on-target conditions with a spatial resolution of  $\sim 4$   $\mu\text{m}$ . The speckle size  $w$  is given by the relationship  $w = \lambda f \approx 6.5$   $\mu\text{m}$ , with  $\lambda$  and  $f$  being the laser wavelength and imaging  $f$  number, respectively.

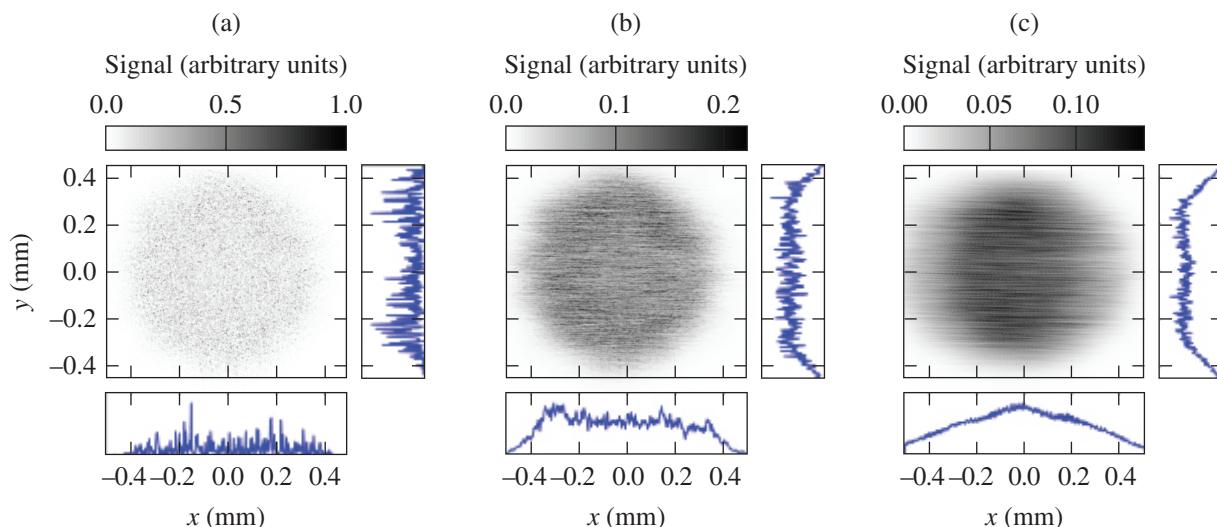


E25133JR

Figure 147.6

The equivalent-target-plane (ETP) diagnostic on OMEGA EP measures the focal-spot profile of a low-power, phase-plate-focused beam with and without SSD bandwidth. DPP: distributed phase plate.

Images of the far-field profile of a wEP-SG8-0800 DPP irradiated with a 2-ns pulse and using different levels of SSD are shown in Fig. 147.7. In addition to the time-integrated far-field data, each image shows central lineouts through the data in the horizontal and vertical directions, below and to the right of the far-field image, respectively. All far-field spots contain the same



TC10827JR

Figure 147.7

Equivalent-target-plane images of the far field of a wEP-SG8-0800 phase plate and central lineouts in the horizontal and vertical directions. (a) With no applied SSD bandwidth, the speckle pattern of the phase-plate-focused far field is well resolved. (b) SBSS SSD and (c) multi-FM SSD applied smoothing in the horizontal direction. The data smoothed by multi-FM SSD are significantly smoother in both the vertical and horizontal directions because of the increased bandwidth.

amount of energy, and the color scales have been adjusted for each image to fully capture the recorded signal range.

The case where no SSD has been applied is shown in Fig. 147.7(a). There is no SSD bandwidth and the speckle pattern is unperturbed and stationary throughout the pulse duration. The speckle pattern is well resolved in the ETP data, and the central lineouts through the data exhibit severe intensity modulations in both the  $x$  and  $y$  directions. Figure 147.7(b) shows the effect of applying SBSS SSD to the laser pulse. The speckle pattern is displaced in the horizontal direction, smoothing the time-integrated intensity profile. Applying 1-D multi-FM SSD results in the far-field laser spot shown in Fig. 147.7(c)—the smoothest of the three cases shown here—where the intensity modulations in the central lineouts are reduced considerably. Both SBSS SSD and multi-FM SSD apply the angular dispersion in one dimension only, resulting in the smoothing applied predominantly in a single direction (horizontal in Fig. 147.7). As can be seen from the central lineouts, despite the 1-D nature of the applied SSD bandwidth, smoothing is observed in both the  $x$  and  $y$  directions.

The recorded ETP data agree well with numerical predictions of the smoothing performance. Figure 147.8 shows azimuthally averaged power spectral densities (PSD's) of the far-field data in Fig. 147.7 (blue lines) and the equivalent theoretical predictions (red). The predicted PSD's were calculated by propagating measured near-field phase fronts using the code *Waasikwa*,<sup>29</sup> which incorporates numerical models of the phase plate and SSD. The experimental data agree well with the predictions up to the ETP system resolution at a frequency of  $\sim 0.1 \mu\text{m}^{-1}$ . While SBSS SSD generates a notably smoother

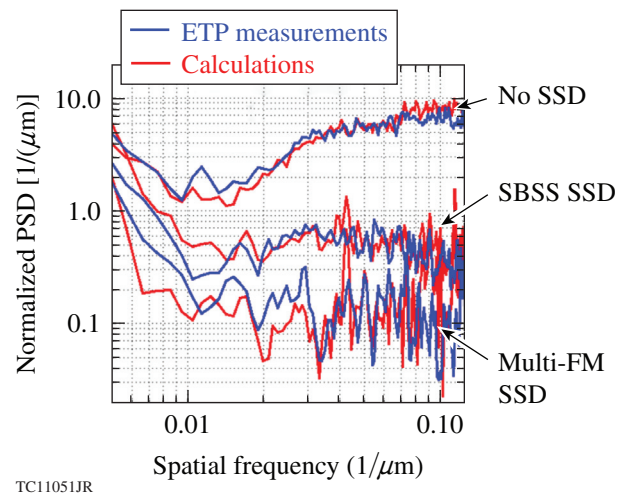


Figure 147.8

The azimuthally averaged power spectral densities of the far-field data in Fig. 147.7 (blue) agree well with the numerical predictions for the different SSD cases (red). Over the plotted frequency range, the power amplitudes are reduced by 50% for multi-FM versus SBSS SSD. PSD: power spectral density.

profile than in the case of no applied SSD, multi-FM SSD reduces the PSD amplitudes further by  $\sim 50\%$  to  $70\%$  in the range of  $0.01$  to  $0.1 \mu\text{m}^{-1}$ , corresponding to modes  $\sim 100$  to  $1000$  of an ignition-scale target.

### Measurements and Simulations of Experimental RT Growth

Experiments were performed to study the effect of multi-FM smoothing on laser imprinting in dedicated OMEGA EP target experiments. The experimental setup shown schematically in Fig. 147.9 is based on similar RT-growth experiments per-

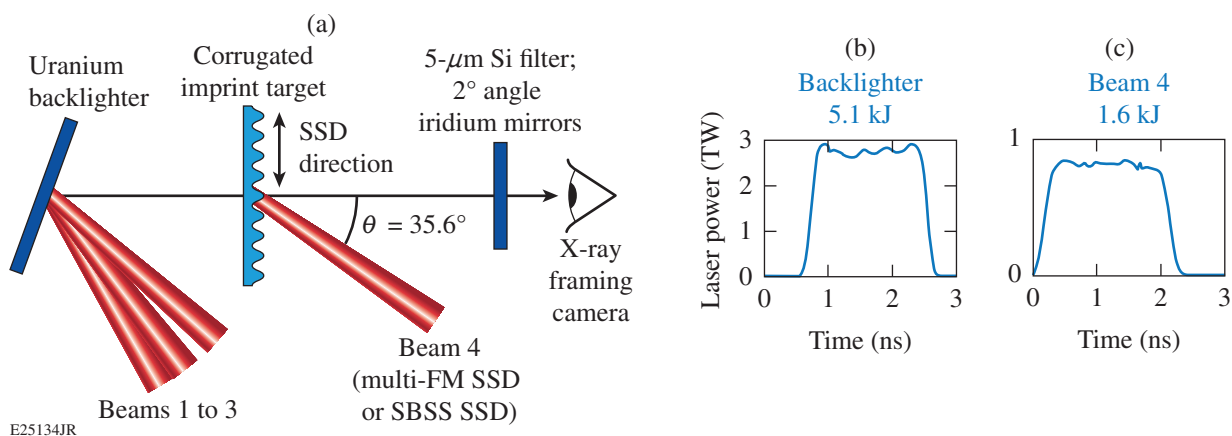


Figure 147.9

Rayleigh–Taylor growth of laser-imprint-seeded modulation and an imposed  $30\text{-}\mu\text{m}$  corrugation were tracked by face-on radiography. The spatial variation in the optical depth of the imprint target was recorded using a fast x-ray framing camera giving  $100\text{-ps}$  snapshots of the target evolution.

formed on OMEGA.<sup>22,30</sup> A planar, 20- $\mu\text{m}$ -thick CH foil was driven with  $\sim 1.6$  kJ by Beamline 4 using a 2-ns square pulse with an on-target irradiance of  $\sim 10^{14}$  W/cm<sup>2</sup> and a rise time of  $\sim 250$  ps, dominated by the temporal skew imposed by the SSD dispersion grating. The imprint target featured a single-mode, sinusoidal surface corrugation with a wavelength of 30  $\mu\text{m}$  and amplitude of 0.1  $\mu\text{m}$  that acts as a reference for the imprint-seeded, broadband RT growth. For a typical ignition-scale direct-drive target, this corresponds to a Legendre mode of  $\sim 350$  (Ref. 7).

The corrugation was oriented approximately perpendicular to the active SSD direction. The experiments were carried out with either SBSS SSD or multi-FM SSD applied over the full duration of the drive laser. Operation without any SSD bandwidth was not supported because of the potential risk of optics damage in the laser system. The RT-amplified corrugation mode and broadband laser imprint were measured using face-on x-ray radiography of the driven target, providing an optical-depth map of the target at discrete times and highlighting areas of spike and bubble growth. The backlighter was a uranium foil driven with Beamlines 1, 2, and 3 of the OMEGA EP laser with a 2-ns pulse containing a total of  $\sim 5$  kJ of energy and an on-target irradiance of  $\sim 3 \times 10^{14}$  W/cm<sup>2</sup>. An undriven, 3- $\mu\text{m}$ -thick Al foil was placed between the backlighter and the imprint foil. This foil acted as a shield, protecting the imprint target from plasma blowoff generated at the backlighter, as well as from soft x-ray emission that could preheat the imprint target. X rays transmitted through the Al heat shield and the imprint target were imaged with 10- $\mu\text{m}$  pinholes onto a fast x-ray framing camera.<sup>31</sup> A combination of iridium-coated, grazing-incidence mirrors oriented at a 2° angle of incidence and 5- $\mu\text{m}$ -thick Si filtering limited the recorded x-ray energy to  $\sim 1.5$  keV. The x-ray framing camera recorded multiple snapshots of the target's optical depth over an  $\sim 1$ -ns window, with individual images integrated over the camera gate width of  $\sim 100$  ps. This radiography technique lacks the sensitivity to measure imprint levels or the preimposed corrugation feature directly and relies on RT growth of the target modulations to produce detectable levels of variation in optical depth.

Unlike previous planar-target imprint experiments performed on OMEGA (see, e.g., Ref. 22), in the experiments discussed here the imprint target was irradiated from the side facing the detector (compare Fig. 147.9). Driving the imprint target from the rear is the preferred option since the CH target itself acts as a filter for its own self-emission. The reverse geometry for the multi-FM measurements, however, is necessitated by the beam and diagnostics layout on OMEGA EP, where all

beams originate from the same direction. At an x-ray energy of 1.5 keV, the energy used to probe the optical-depth evolution, a 20- $\mu\text{m}$ -thick plastic foil attenuates the x-ray flux to  $\sim 25\%$ . This drops the achievable signal-to-noise ratio in these experiments by approximately a factor of 4 compared to a rear-driven geometry since the backlighter emission competes with higher levels of self-emission.

To extract the evolution of modulation amplitudes, the optical-depth maps are converted into frequency space by Fourier transformation. Examples of experimental optical-depth maps are shown in Fig. 147.10, with Fig. 147.10(a) using SBSS SSD and Fig. 147.10(b) using 1-D multi-FM SSD; Figs. 147.10(c) and 147.10(d) are the equivalent frequency maps, respectively. The optical-depth maps, plotted on the same color scale, were obtained  $\sim 1.75$  ns after the onset of the laser drive. In these data, the initially imposed corrugation is oriented vertically; i.e., lines of equal amplitude are parallel to the y direction, and the active SSD direction is approximately horizontal. While the corrugation mode is more dominant in the multi-FM-smoothed data, the corrugation is well resolved in both data sets, appear-

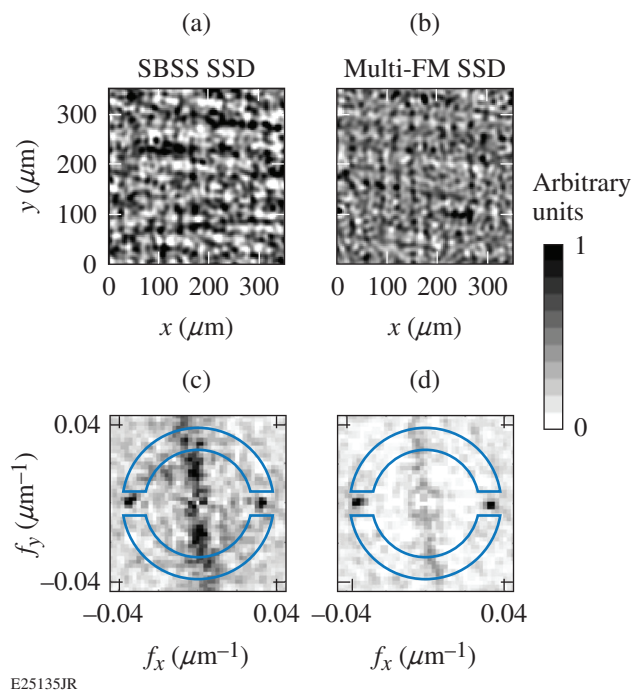


Figure 147.10 [(a),(b)] Optical-depth data with SBSS SSD and multi-FM SSD, respectively. The 30- $\mu\text{m}$  corrugation appears as vertical lines, with SSD acting mainly in the horizontal direction. In frequency space [(c),(d)] the corrugation appears as a single peak at  $f_x = 1/30 \mu\text{m}^{-1}$ . Because of the 1-D nature of multi-FM SSD, broadband imprint is predominantly located along  $f_y$  for  $f_x \sim 0$ . The semicircles denote the analysis region for the  $f \sim 1/30\text{-}\mu\text{m}$  broadband mode.

ing as vertical lines in the optical depth, and as a single peak in frequency space for  $f_x = 1/30 \mu\text{m}^{-1}$  and  $f_y = 0$ . In both cases, broadband imprint and RT growth are predominantly visible in the direction perpendicular to the active SSD smoothing, appearing as irregular structures in the horizontal direction in the optical-depth data and elevated mode amplitudes in the  $f_y$  direction for  $f_x \sim 0$  in the frequency maps. The data are oriented such that the corrugation feature falls at  $f_y = 0$ , while a slight target misalignment resulted in the direction of least smoothing (i.e., perpendicular to the active SSD direction) at  $\varphi \approx 98^\circ$ . The broadband-imprint feature along this direction is noticeably broader in  $f_x$  for the SBSS data [Fig. 147.10(c)] than in the multi-FM case [Fig. 147.10(d)], as expected from the improved smoothing of 1-D multi-FM SSD.

To calculate areal density from the measured optical depth, the backlighter emission was characterized by radiographing an undriven sample target in a dedicated experiment. The sample target was made of the same CH material as the imprint target and comprised multiple steps of known CH thickness. This calibration experiment directly relates experimental optical depth and target areal densities and confirms a central backlighter energy of  $\sim 1.5$  keV.

The experimentally measured evolution of the 30- $\mu\text{m}$  corrugation is shown in Fig. 147.11(a), plotting the areal-density amplitude as a function of time. The circles denote data recorded with 1-D multi-FM SSD applied to the drive laser, while the squares denote data taken with SBSS SSD. Since the corrugation mode is preimposed and not an imprint feature, its growth and absolute amplitude should be independent of the applied SSD bandwidth, as confirmed by the experimental data. The data points in Fig. 147.11(b) show the root-mean-square (rms) amplitude of the broadband 30- $\mu\text{m}$  imprint, corresponding to the azimuthally integrated  $f \sim 1/30\text{-}\mu\text{m}^{-1}$  mode in frequency space, but excluding a region of  $\Delta f_x = \Delta f_y = 1/250^{-1} \mu\text{m}$  centered around the corrugation peak at  $f_x = 1/30 \mu\text{m}^{-1}$  and  $f_y = 0$ . The integration range is marked by the region inside the two semicircles overlaid onto the frequency space maps in Figs. 147.10(c) and 147.10(d). These data were recorded on the same shots as the data shown in Fig. 147.11(a). While there is considerable noise in the data, the SBSS-smoothed amplitudes consistently exceed the multi-FM case by a factor of  $\sim 2$ .

Simulation results for the growth of the corrugation mode and the rms amplitude of the  $f \sim 1/30\text{-}\mu\text{m}$  broadband imprint mode are shown as the solid lines in Figs. 147.11(a) and 147.11(b), respectively. The target evolution was simulated using the 2-D radiation-hydrodynamics code *DRACO*,<sup>32</sup> which

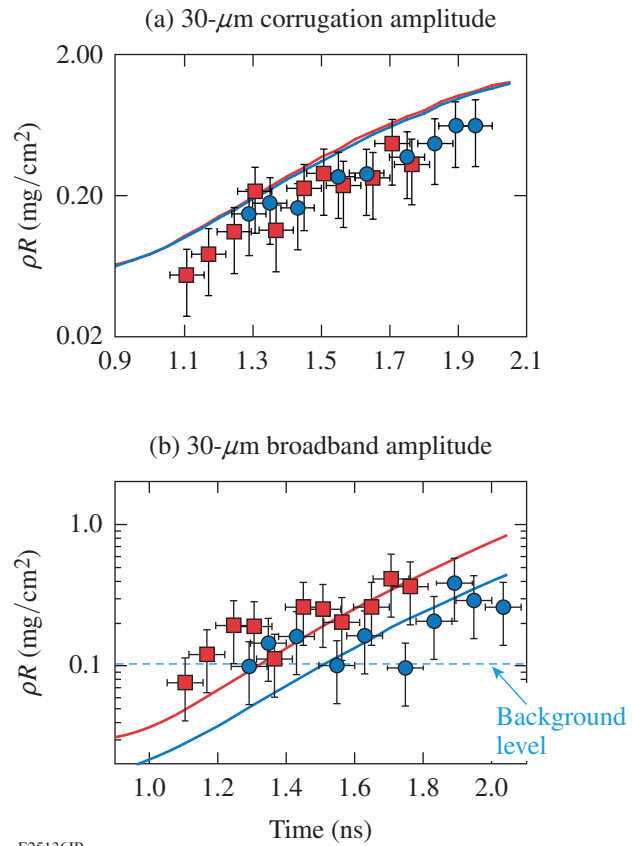
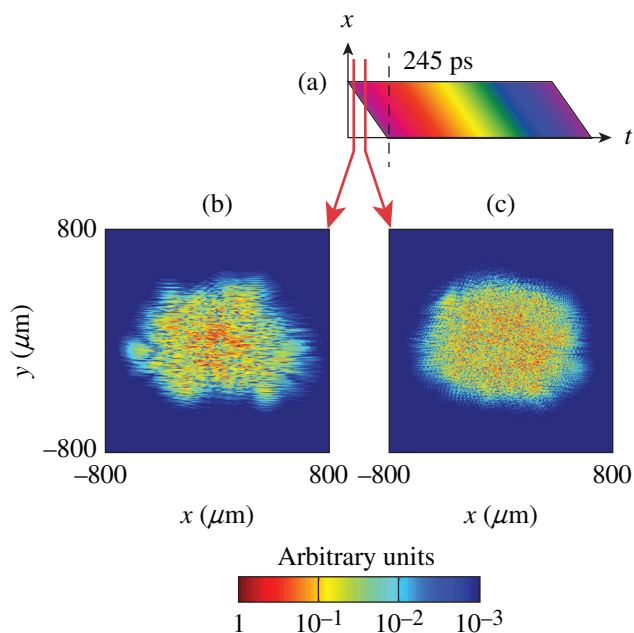


Figure 147.11

(a) Time evolution of the 30- $\mu\text{m}$  experimental (data points) and simulated (lines) corrugation amplitudes. The red squares denote data acquired with SBSS SSD and the blue circles denote data acquired with multi-FM SSD. The corrugated mode is not affected by imprint and exhibits a growth rate independent of the SSD bandwidth. (b) Root-mean-square (rms) amplitude of the experimental (data points) and simulated (lines) broadband 30- $\mu\text{m}$  mode. The dashed horizontal line denotes the background level in the experimental data. The red and blue lines are 2-D *DRACO* simulated growth rates for SBSS and multi-FM, respectively.

includes a 3-D ray-trace package to model the laser absorption. The effect of the SSD bandwidth is taken into account by calculating the far-field laser spots multiple times per picosecond using the code *Waasikwa*.<sup>29</sup> The code uses the near-field laser intensity and phase, including the SSD bandwidth and its effect, and propagates it through the phase plate and the main lens to obtain an instantaneous far field. Figure 147.12(a) illustrates a laser beam's near-field lineout along the SSD active direction as a function of time, with different colors illustrating the change in light frequency related to the SSD bandwidth. The temporal skew caused by the uncompensated diffraction grating in the SSD chain results in an initially sub-aperture beam incident onto the DPP, which gradually increases in area to full aperture by the end of the 245-ps skew interval. The action of 1-D SSD and an uncompensated diffraction grating result in an asym-

metric and time-dependent far-field spot and speckle pattern, as illustrated in Figs. 147.12(b) and 147.12(c), which show calculated far-field profiles at 20 ps and 100 ps, respectively.



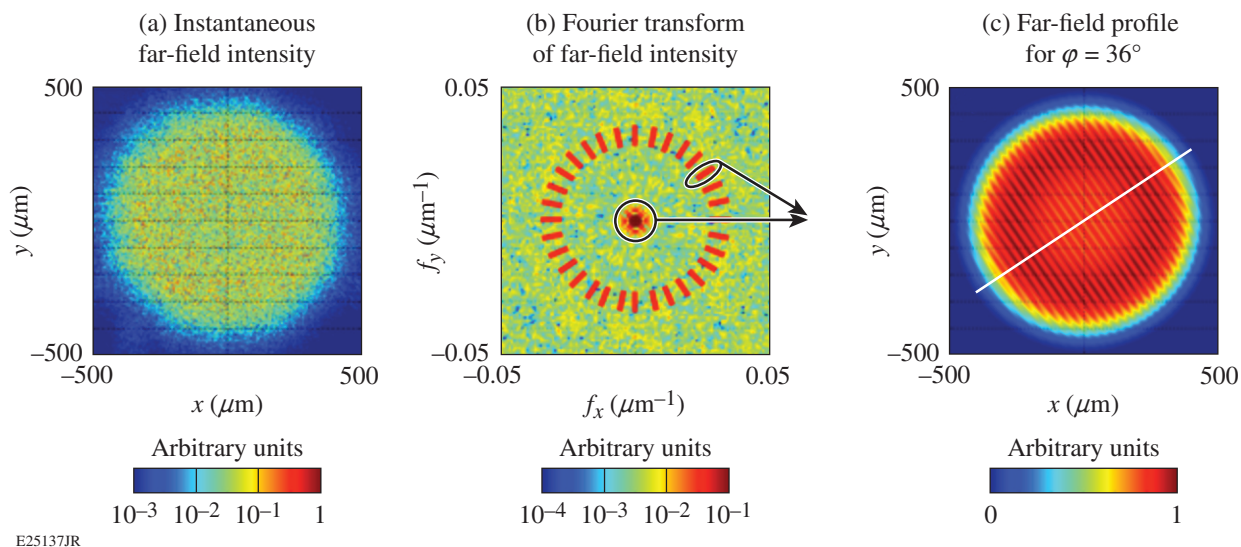
TC11052JR

Figure 147.12

(a) Illustration of the laser beam's near field along the SSD active direction versus time. [(b),(c)] Far fields calculated by *Waasikwa* from instantaneous near fields at times of 20 ps and 100 ps, respectively.

To fully simulate the interaction of the 1-D multi-FM and SBSS SSD-smoothed laser beams with the target requires a 3-D hydrocode and a 3-D ray trace. In such calculations, the instantaneous far fields would be used to assign the energy of rays launched at the outer boundary of the simulation region, which would then be traced through the plasma, depositing their energy in cells of the simulation mesh by the inverse bremsstrahlung process, capturing the asymmetry of the SSD action with respect to the target's  $x$  and  $y$  coordinates. In 2-D cylindrical hydro simulations with a 3-D ray trace, however, such as used for the simulations presented here, the  $x$  and  $y$  coordinates are reduced to a single axis by averaging the laser deposition along the azimuthal angle  $\varphi$ . This makes it impossible to capture the effect of SSD with a single 2-D calculation. It is possible to simplify the problem, however, by taking advantage of the fact that at early stages of the laser drive, the nonuniformities are small and the RT growth is in its linear stage. During the linear stage, individual modulation modes do not interact with each other and can be considered independently. This allows one to reproduce the 3-D nature of the experiment with a set of 2-D hydrocode simulations in which each simulation considers only a single frequency slice of the incident far-field spectrum.

As illustrated in Fig. 147.13, the full 3-D target response was calculated by dividing the instantaneous, incident far field [Fig. 147.13(a)] into 120 frequency slices at a 3° separation



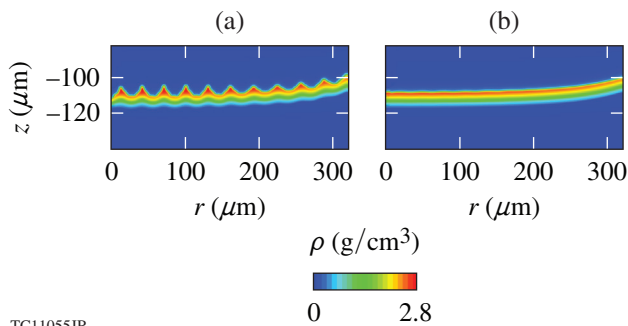
E25137JR

Figure 147.13

Combining multiple 2-D simulations using a reduced far-field spot as the input captured the 3-D experimental imprint. The instantaneous laser far field (a) is converted into frequency space (b) and divided into 120 frequency slices with 3° separation. (c) The reduced far-field spot for  $\varphi = 36^\circ$  is constructed by combining the low-spatial-frequency envelope with the 29- to 31-μm wavelength range of the  $\varphi = 36^\circ$  frequency slice.

[Fig. 147.13(b)]. Combining the time-varying, low-spatial-frequency envelope at the center of the frequency map with the Fourier modes with the 29- to 31- $\mu\text{m}$  wavelengths contained within each frequency slice gives a “reduced” far-field spot. This reduced far-field spot contains modulations in only a single direction, as determined by the selected frequency slice, and can be used as an input for a 2-D simulation. An example of such a reduced far field [Fig. 147.13(c)] shows the far-field spot for the  $\varphi = 36^\circ$  frequency slice. In these 2-D calculations, the initial target corrugation was included in only the frequency slice for  $\varphi = 0^\circ$ ; i.e., along the 1-D multi-FM SSD active direction and the direction of the most-efficient smoothing.

Individual frequency-slice calculations that emulate the effect of 1-D multi-FM SSD are presented in Fig. 147.14. These images show mass-density profiles of the accelerated foil at 1.75 ns. Figure 147.14(a) shows the case for the frequency slice at  $\varphi = 90^\circ$  (along the vertical axis and perpendicular to the multi-FM SSD active direction); Fig. 147.14(b) shows the case for the frequency slice at  $\varphi = 69^\circ$ . The smoothing is least efficient perpendicular to the SSD active direction, and the density profile shown in Fig. 147.14(a) has noticeable RT growth, resulting from far-field-spot modulations and laser imprint. In contrast, the profile in Fig. 147.14(b) exhibits very little growth, emphasizing how 1-D multi-FM SSD efficiently suppresses imprint modes that have a non-negligible component along the active SSD direction.



TC11055JR

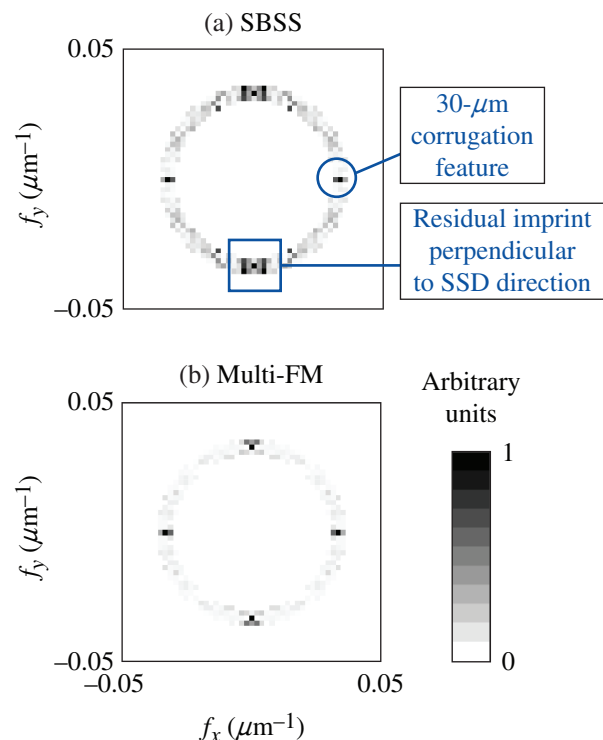
Figure 147.14

Profiles of the calculated foil density at 1.75 ns using 1-D multi-FM SSD for two of the 120 laser far-field frequency slices with wavelengths of 29 to 30  $\mu\text{m}$ . (a) The least amount of imprint mitigation is found for the far-field frequency component perpendicular to the active SSD direction. (b) At  $69^\circ$  off the active SSD direction, imprint is already significantly reduced.

As shown in Fig. 147.15, *DRACO* simulations reproduce imprint and corrugation features seen in the Fourier space of the experimental optical-depth maps, such as the directionality of the SSD observed in frequency space (compare to

Fig. 147.10). The broadband imprint is dominated by Fourier modes perpendicular to the active SSD direction and close to  $f_x \sim 0$ , while the modes with  $f_x \neq 0$  are effectively removed by the SSD (more so in the case of multi-FM than SBSS SSD).

The simulated corrugation amplitudes versus time are shown in Fig. 147.11(a) as the solid lines. While the growth rate observed in the experiment is reproduced correctly, the simulation exhibits a 40%-higher amplitude compared to the experimental data. The source of the disagreement between the experimental growth of the preimposed corrugation and its simulation is currently unknown, but it is likely caused by a combination of the background in the data or an uncharacterized level of surface roughness of the imprint foil. The simulated broadband imprint amplitudes of the nonuniformities at a frequency of  $1/30 \mu\text{m}^{-1}$  are shown in Fig. 147.11(b) for the SBSS (red line) and multi-FM SSD case (blue line). The numerical calculations reproduce the experimental data within the error bars once the data exceed the background level. The simulations predict an  $\sim 2\times$  reduction of the imprint level for the multi-FM SSD case compared to the SBSS SSD case, consistent with the experimental data. The calculations further reproduce



TC11056JR

Figure 147.15

Fourier transform of *DRACO*-simulated optical depth at 1.75 ns for  $f \sim 1/30 \mu\text{m}$  using (a) SBSS SSD and (b) multi-FM SSD.

the directionality of SSD observed in frequency space [compare Fig. 147.15 and Figs. 147.10(c) and 147.10(d)]. The broadband imprint is dominated by Fourier modes perpendicular to the active SSD direction and close to  $f_x \sim 0$ , while the modes with  $f_x \neq 0$  are effectively removed by SSD (more so in the case of multi-FM than SBSS SSD).

### Conclusions

In summary, 1-D multi-FM SSD beam smoothing was developed at LLE to provide sufficient far-field uniformity for direct-drive inertial confinement fusion applications at the National Ignition Facility. A prototype of the multi-FM system has been implemented in the NIF-like Beamline 4 on the OMEGA EP laser for verification purposes. Multi-FM SSD beam-smoothing performance was verified with both equivalent-target-plane measurements of the laser's far field and in dedicated planar-target experiments by comparing smoothing rates with SBSS SSD and multi-FM SSD. Numerical calculations using the code *Waasikwa* agree well with measurements of the multi-FM-smoothed, far-field spatial frequency spectrum. In the planar-target experiments, Rayleigh–Taylor growth rates of laser-imprinted and preimposed surface modulations at  $f \sim 1/30 \mu\text{m}$  were measured by face-on x-ray radiography. As expected, the growth of the preimposed surface corrugation is independent of the SSD bandwidth, while 1-D multi-FM SSD is observed to reduce imprint levels by  $\sim 50\%$  compared to SBSS SSD. The target experiment was simulated using the 2-D hydrodynamics code *DRACO* and realistic, time-dependent, far-field spot intensity calculations that included the effect of SSD. The 3-D nature of the imprint experiment was captured in the 2-D calculations by 120 individual simulations of a reduced far-field spot, containing only broadband modes in a single 2-D frequency slice. Within the error bars, the simulations correctly reproduce the relative and absolute amplitude levels between multi-FM and SBSS-SSD-smoothed broadband data, but they fail to capture the absolute amplitudes of the preimposed corrugation mode. An experimental unknown, such as surface roughness or an unaccounted-for background level, may be the cause of this discrepancy. Despite this discrepancy, the experimental data show a clear enhancement in smoothing performance of multi-FM SSD compared to SBS-suppression SSD, in agreement with simulations.

### ACKNOWLEDGMENT

This material is based upon work supported by the Department of Energy National Nuclear Security Administration under Award Number DE-NA0001944, the University of Rochester, and the New York State Energy Research and Development Authority. The support of DOE does not constitute an endorsement by DOE of the views expressed in this article.

### REFERENCES

1. G. H. Miller, E. I. Moses, and C. R. Wuest, *Opt. Eng.* **43**, 2841 (2004).
2. J. Nuckolls *et al.*, *Nature* **239**, 139 (1972).
3. J. D. Lindl, *Inertial Confinement Fusion: The Quest for Ignition and Energy Gain Using Indirect Drive* (Springer-Verlag, New York, 1998).
4. S. Atzeni and J. Meyer-ter-Vehn, *The Physics of Inertial Fusion: Beam Plasma Interaction, Hydrodynamics, Hot Dense Matter, International Series of Monographs on Physics* (Clarendon Press, Oxford, 2004).
5. R. S. Craxton, K. S. Anderson, T. R. Boehly, V. N. Goncharov, D. R. Harding, J. P. Knauer, R. L. McCrory, P. W. McKenty, D. D. Meyerhofer, J. F. Myatt, A. J. Schmitt, J. D. Sethian, R. W. Short, S. Skupsky, W. Theobald, W. L. Kruer, K. Tanaka, R. Betti, T. J. B. Collins, J. A. Delettrez, S. X. Hu, J. A. Marozas, A. V. Maximov, D. T. Michel, P. B. Radha, S. P. Regan, T. C. Sangster, W. Seka, A. A. Solodov, J. M. Soures, C. Stoeckl, and J. D. Zuegel, *Phys. Plasmas* **22**, 110501 (2015).
6. P. W. McKenty, V. N. Goncharov, R. P. J. Town, S. Skupsky, R. Betti, and R. L. McCrory, *Phys. Plasmas* **8**, 2315 (2001).
7. T. J. B. Collins, J. A. Marozas, K. S. Anderson, R. Betti, R. S. Craxton, J. A. Delettrez, V. N. Goncharov, D. R. Harding, F. J. Marshall, R. L. McCrory, D. D. Meyerhofer, P. W. McKenty, P. B. Radha, A. Shvydky, S. Skupsky, and J. D. Zuegel, *Phys. Plasmas* **19**, 056308 (2012).
8. M. Hohenberger, P. B. Radha, J. F. Myatt, S. LePape, J. A. Marozas, F. J. Marshall, D. T. Michel, S. P. Regan, W. Seka, A. Shvydky, T. C. Sangster, J. W. Bates, R. Betti, T. R. Boehly, M. J. Bonino, D. T. Casey, T. J. B. Collins, R. S. Craxton, J. A. Delettrez, D. H. Edgell, R. Epstein, G. Fiksel, P. Fitzsimmons, J. A. Frenje, D. H. Froula, V. N. Goncharov, D. R. Harding, D. H. Kalantar, M. Karasik, T. J. Kessler, J. D. Kilkenny, J. P. Knauer, C. Kurz, M. Lafon, K. N. LaFortune, B. J. MacGowan, A. J. Mackinnon, A. G. MacPhee, R. L. McCrory, P. W. McKenty, J. F. Meecker, D. D. Meyerhofer, S. R. Nagel, A. Nikroo, S. Obenshain, R. D. Petrasso, J. E. Ralph, H. G. Rinderknecht, M. J. Rosenberg, A. J. Schmitt, R. J. Wallace, J. Weaver, C. Widmayer, S. Skupsky, A. A. Solodov, C. Stoeckl, B. Yaakobi, and J. D. Zuegel, *Phys. Plasmas* **22**, 056308 (2015).
9. D. K. Bradley, J. A. Delettrez, R. Epstein, R. P. J. Town, C. P. Verdon, B. Yaakobi, S. Regan, F. J. Marshall, T. R. Boehly, J. P. Knauer, D. D. Meyerhofer, V. A. Smalyuk, W. Seka, D. A. Haynes, Jr., M. Gunderson, G. Junkel, C. F. Hooper, Jr., P. M. Bell, T. J. Ognibene, and R. A. Lerche, *Phys. Plasmas* **5**, 1870 (1998).
10. S. E. Bodner, *Phys. Rev. Lett.* **33**, 761 (1974).
11. S. Chandrasekhar, in *Hydrodynamic and Hydromagnetic Stability, International Series of Monographs on Physics* (Clarendon Press, Oxford, 1961).
12. V. N. Goncharov, S. Skupsky, T. R. Boehly, J. P. Knauer, P. McKenty, V. A. Smalyuk, R. P. J. Town, O. V. Gotchev, R. Betti, and D. D. Meyerhofer, *Phys. Plasmas* **7**, 2062 (2000).
13. Y. Lin, T. J. Kessler, and G. N. Lawrence, *Opt. Lett.* **21**, 1703 (1996).
14. S. N. Dixit *et al.*, *Proc. SPIE* **2633**, 141 (1995).

15. T. R. Boehly, V. A. Smalyuk, D. D. Meyerhofer, J. P. Knauer, D. K. Bradley, R. S. Craxton, M. J. Guardalben, S. Skupsky, and T. J. Kessler, *J. Appl. Phys.* **85**, 3444 (1999).
16. R. H. Lehmberg and S. P. Obenschain, *Opt. Commun.* **46**, 27 (1983).
17. S. Skupsky, R. W. Short, T. Kessler, R. S. Craxton, S. Letzring, and J. M. Soures, *J. Appl. Phys.* **66**, 3456 (1989).
18. B. J. MacGowan *et al.*, *Phys. Plasmas* **3**, 2029 (1996).
19. C. A. Haynam *et al.*, *Appl. Opt.* **46**, 3276 (2007).
20. T. R. Boehly, D. L. Brown, R. S. Craxton, R. L. Keck, J. P. Knauer, J. H. Kelly, T. J. Kessler, S. A. Kumpan, S. J. Loucks, S. A. Letzring, F. J. Marshall, R. L. McCrory, S. F. B. Morse, W. Seka, J. M. Soures, and C. P. Verdon, *Opt. Commun.* **133**, 495 (1997).
21. S. P. Regan, J. A. Marozas, R. S. Craxton, J. H. Kelly, W. R. Donaldson, P. A. Jaanimagi, D. Jacobs-Perkins, R. L. Keck, T. J. Kessler, D. D. Meyerhofer, T. C. Sangster, W. Seka, V. A. Smalyuk, S. Skupsky, and J. D. Zuegel, *J. Opt. Soc. Am. B* **22**, 998 (2005).
22. T. R. Boehly, V. N. Goncharov, O. Gotchev, J. P. Knauer, D. D. Meyerhofer, D. Oron, S. P. Regan, Y. Srebro, W. Seka, D. Shvarts, S. Skupsky, and V. A. Smalyuk, *Phys. Plasmas* **8**, 2331 (2001).
23. S. Skupsky and R. S. Craxton, *Phys. Plasmas* **6**, 2157 (1999).
24. *LLE Review Quarterly Report* **114**, 73, Laboratory for Laser Energetics, University of Rochester, Rochester, NY, LLE Document No. DOE/NA/28302-826, NTIS Order No. DE2008935224 (2008).
25. J. A. Marozas, J. D. Zuegel, and T. J. B. Collins, *Bull. Am. Phys. Soc.* **55**, 294 (2010).
26. L. J. Waxer, M. J. Guardalben, J. H. Kelly, B. E. Kruschwitz, J. Qiao, I. A. Begishev, J. Bromage, C. Dorrer, J. L. Edwards, L. Folsbee, S. D. Jacobs, R. Jungquist, T. J. Kessler, R. W. Kidder, S. J. Loucks, J. R. Marciante, D. N. Maywar, R. L. McCrory, D. D. Meyerhofer, S. F. B. Morse, A. V. Okishev, J. B. Oliver, G. Pien, J. Puth, and A. L. Rigatti, in *Conference on Lasers and Electro-Optics/Quantum Electronics and Laser Science Conference and Photonic Applications Systems Technologies, OSA Technical Digest (CD)* (Optical Society of America, Washington, DC, 2008), Paper JThB1.
27. *LLE Review Quarterly Report* **85**, 39, Laboratory for Laser Energetics, University of Rochester, Rochester, NY, LLE Document No. DOE/SF/19460-378, PB2006106656 (2000).
28. S. P. Regan, J. A. Marozas, J. H. Kelly, T. R. Boehly, W. R. Donaldson, P. A. Jaanimagi, R. L. Keck, T. J. Kessler, D. D. Meyerhofer, W. Seka, S. Skupsky, and V. A. Smalyuk, *J. Opt. Soc. Am. B* **17**, 1483 (2000).
29. J. A. Marozas, S. P. Regan, J. H. Kelly, D. D. Meyerhofer, W. Seka, and S. Skupsky, *J. Opt. Soc. Am. B* **19**, 7 (2002).
30. V. A. Smalyuk, T. R. Boehly, D. K. Bradley, V. N. Goncharov, J. A. Delettrez, J. P. Knauer, D. D. Meyerhofer, D. Oron, D. Shvarts, Y. Srebro, and R. P. J. Town, *Phys. Plasmas* **6**, 4022 (1999).
31. D. K. Bradley *et al.*, *Rev. Sci. Instrum.* **66**, 716 (1995).
32. P. B. Radha, V. N. Goncharov, T. J. B. Collins, J. A. Delettrez, Y. Elbaz, V. Yu. Glebov, R. L. Keck, D. E. Keller, J. P. Knauer, J. A. Marozas, F. J. Marshall, P. W. McKenty, D. D. Meyerhofer, S. P. Regan, T. C. Sangster, D. Shvarts, S. Skupsky, Y. Srebro, R. P. J. Town, and C. Stoeckl, *Phys. Plasmas* **12**, 032702 (2005).

# Plasma Characterization Using Ultraviolet Thomson Scattering from Ion-Acoustic and Electron Plasma Waves

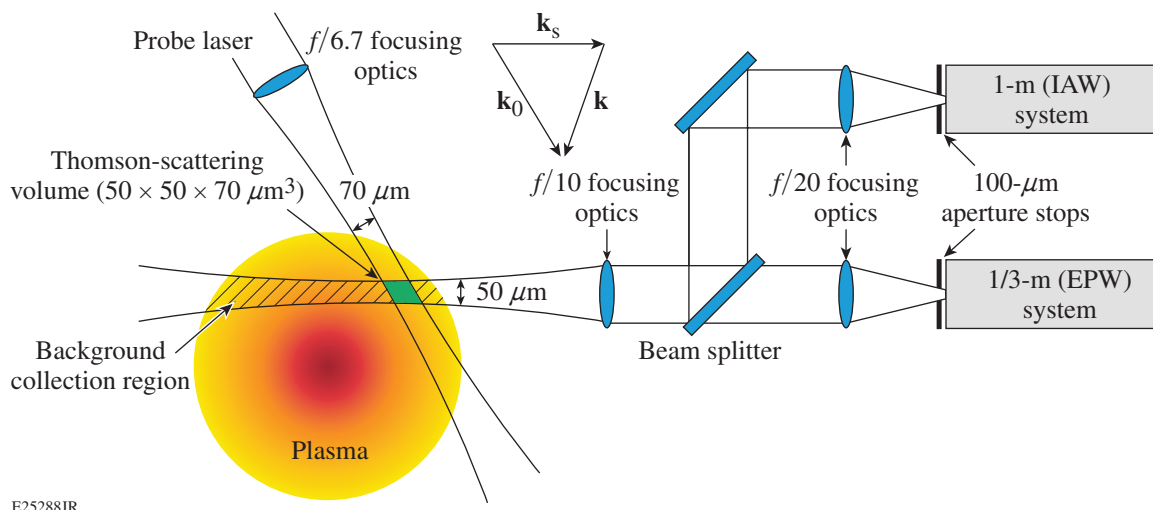
## Introduction

Optical Thomson scattering from collective plasma oscillations is a standard technique for diagnosing underdense plasma conditions in high-energy-density-physics experiments.<sup>1</sup> Thomson scattering is used to make spatially<sup>2</sup> and temporally resolved<sup>3–5</sup> measurements of the electron temperature ( $T_e$ ), ion temperature ( $T_i$ ), electron density ( $n_e$ ), fluid velocity ( $\mathbf{u}$ ), heat flux, ionization state ( $Z$ ), and ion species fractions (for a multiple ion species plasma). Thomson scattering is used here to diagnose a number of plasma-wave instabilities including stimulated Brillouin scattering,<sup>6–8</sup> stimulated Raman scattering,<sup>9</sup> two-ion decay,<sup>10</sup> and two-plasmon decay.<sup>11,12</sup>

Thomson-scattering diagnostics take a local measurement of the plasma conditions averaged over a small volume (typically  $\sim 50 \mu\text{m}^3$ ). The Thomson-scattering volume is created by overlapping the waist of the probe laser with an aperture stop within the collection system [typically a pinhole at the spectrometer's entrance (see Fig. 147.16)]. Light scattered from

the Thomson-scattering volume is collected by a telescope and transported to a spectrometer/streak-camera pair to obtain spectral and temporal resolution.<sup>2</sup>

By conserving momentum ( $\mathbf{k}_0 = \mathbf{k}_s + \mathbf{k}$ ), Thomson-scattering probes the plasma waves with wavelengths  $\lambda = 2\pi/|\mathbf{k}|$  ( $\mathbf{k}_0$ ,  $\mathbf{k}_s$ , and  $\mathbf{k}$  are the wave vectors of the probe beam, scattered light, and plasma wave, respectively). The normal modes of the plasma are observed in the Thomson-scattering spectra when probing the appropriate wavelengths, and the measured frequencies of these normal modes provide a powerful diagnostic of the plasma conditions. This collective Thomson-scattering regime is typically characterized by comparing the probed wavelength to the Debye length [ $\lambda_{De} \equiv v_{te}/\omega_{pe}$ , where  $v_{te} = \sqrt{T_e/m_e}$  is the electron thermal velocity,  $\omega_{pe} = \sqrt{4\pi e^2 n_e/m_e}$  is the plasma frequency in centimeter-gram-second (cgs) units, and  $m_e$  is the electron mass]. When  $k\lambda_{De} < 1$ , electron plasma wave (EPW) features are present in the spectrum; when  $k\lambda_{De} < \sqrt{ZT_e/T_i}$ , ion-acoustic features are observed.



E25288JR

Figure 147.16

Thomson-scattering diagnostic configuration on OMEGA. Note that the schematic shows transmissive optics but the actual focusing/collection optics were reflective. IAW: ion-acoustic wave; EPW: electron plasma wave.

In practice, the complete shape of the Thomson-scattering spectrum is used to determine the plasma conditions by integrating the differential Thomson-scattered power per unit frequency per unit solid angle per unit volume over the Thomson-scattering volume and the solid angle of the collection optic:<sup>1</sup>

$$\frac{\partial^3 P_s}{\partial \omega \partial \Omega \partial V} = \frac{I_0 n_e r_0^2}{2\pi} \left| \hat{k}_s \times (\hat{k}_s \times \hat{E}_0) \right| \left( 1 + \frac{2\omega}{\omega_0} \right) S(k, \omega), \quad (1)$$

where  $I_0$  is the incident probe-beam intensity,  $r_0 = e^2/m_e c^2$  is the classical electron radius,  $\hat{E}_0$  is the polarization direction of the probe beam, and  $\omega(\omega_0)$  is the frequency of the plasma wave (probe beam). The frequency of the scattered light is given by the matching condition

$$\omega_s = \omega_0 - \omega, \quad (2)$$

where  $\omega \in \mathbb{R}$  and waves with negative frequency propagate antiparallel to  $\mathbf{k}$ .

The dynamic form factor (neglecting collisions and in the absence of applied magnetic fields) is derived from the linearized Vlasov equation (and Poisson's equation),

$$S(\mathbf{k}, \omega) = \frac{(k\lambda_{De})^2}{\pi\omega} \left[ \left| 1 - \frac{\chi_e}{\varepsilon} \right|^2 \text{Im}\{\chi_e\} + \sum_j \frac{Z_j^2 n_{ij} T_{ij}}{n_i T_e} \left| \frac{\chi_e}{\varepsilon} \right|^2 \text{Im}\{\chi_{i,j}\} \right], \quad (3)$$

where the sum is over ion species,  $n_{i,j}(T_{i,j})$  is the number density (temperature) of the  $j^{\text{th}}$  ion species,  $n_i = \sum_j Z_j n_{i,j}$ , and  $\varepsilon \equiv 1 + \chi_e + \sum_j \chi_{i,j}$  is the plasma dielectric function. The electron ( $\chi_e$ ) and ion ( $\chi_i$ ) susceptibilities are

$$\chi_s(\mathbf{k}, \omega) = \frac{4\pi q_s^2 n_{s0}}{m_s k^2} \int_{-\infty}^{\infty} d\mathbf{v} \frac{\mathbf{k} \cdot \partial f_{s0} / \partial \mathbf{v}}{\omega - \mathbf{k} \cdot \mathbf{v} - i\gamma}, \quad (4)$$

where  $n_{s0}$  and  $f_{s0}$  are the unperturbed number density and velocity distribution, respectively.

The dominant modes observed in collective Thomson-scattering experiments are given by the real part of the roots of  $\varepsilon(\mathbf{k}, \omega) = 0$ . The difference in frequency between the scattered light and probe beam in the lab frame is determined by

substituting the lab frame probe ( $\omega'_0 + \mathbf{k}_0 \cdot \mathbf{u}$ ) and scattered-light ( $\omega'_s = \omega_s + \mathbf{k}_s \cdot \mathbf{u}$ ) frequencies and the plasma-wave frequency into Eq. (2), which, for scattering from ion-acoustic waves, gives

$$\Delta\omega_{\pm} = (\omega'_s - \omega'_0) = \pm k c_s - \mathbf{k} \cdot \mathbf{u}, \quad (5)$$

and from EPW's

$$\Delta\omega_{\pm} = (\omega'_s - \omega'_0) = \pm \sqrt{\omega_{pe}^2 + 3k^2 v_{te}^2} - \mathbf{k} \cdot \mathbf{u}, \quad (6)$$

where  $\Delta\omega_{\pm}$  corresponds to the frequency shift in the blue- and red-shifted light and  $c_s = \sqrt{(ZT_e + 3T_i)/m_i}$  is the sound speed ( $m_i$  is the ion mass).

Equation (5) shows that the frequencies of the two ion-acoustic wave (IAW) spectral peaks are given by the sound speed, fluid velocity, and plasma-wave vector. The frequency of the peaks in the EPW spectrum is dominated by the electron density because the contribution to the frequency shift related to the  $\omega_{pe}^2$  term in Eq. (6) is typically much larger than the contribution from the other terms. To obtain further information from Thomson-scattering spectra, synthetic power spectra generated using the kinetic description [Eq. (1)] are directly compared to measured spectra. In theory, arbitrary moments of the unperturbed velocity distributions (or their projections along  $\mathbf{k}$ ) can be inferred by fitting Eq. (1) to measured spectra, but experimental uncertainties and degeneracy between parameter variations limit practical measurements to the fourth moment (heat flux) and require the shape of the unperturbed velocity distribution ( $f_{s0}$ ) to be assumed (e.g., Maxwellian or Maxwellian with polynomial corrections).<sup>13,14</sup>

A common challenge in determining accurate plasma conditions from Thomson-scattering spectra is that measured spectra have broader peaks than calculated spectra. This has been attributed to ion-ion collisions,<sup>13,15</sup> plasma gradients, and probing a range of wave vectors.<sup>16</sup> As a first-order approximation, these effects can be accounted for by convolving the calculated spectra with a Gaussian response function. A physically consistent model is required, however, to measure parameters that depend on the detailed shape and not just the frequency of the spectral peaks.

The impact of gradients on Thomson-scattering measurements can be approximated by comparing the derivatives of Eqs. (5) and (6) to the linear Landau-damping rates. Gradient effects can be neglected when the broadening of the spectral peaks related to gradients is much less than the broadening

caused by damping. In the weak damping limit, the damping rate is given by the imaginary part of the dielectric function divided by the spectral derivative of its real part evaluated at the normal mode frequency  $[\omega_i = -\epsilon_i / (\partial\epsilon_r / \partial\omega)]$  (Ref. 17). Simplifying to 1-D, the dominant term in broadening of the spectral peaks caused by spatial gradients in Eq. (5) is typically the fluid velocity gradient  $\delta\omega_{\pm} = \delta x k \partial u / \partial x$ , and variations in the probed wave vector give  $\delta\omega_{\pm} = \delta k (\pm c_s - u)$ . Wave-vector variations are typically negligible in Eq. (6) and the dominant spatial term is  $\delta\omega_{\pm} = \delta x \omega_{pe} / L_n$ , where  $L_n$  is the density scale length.

Some of the physical effects that should be included when fitting measured Thomson-scattering spectra to calculated spectra are presented in this article. The following sections (1) present experimentally measured Thomson-scattering spectra from IAW's and EPW's from a series of direct-drive inertial confinement fusion implosions<sup>18</sup> on the OMEGA laser<sup>19</sup> and discuss spectral calibration and background radiation; (2) describe the techniques used to analyze the measured spectra; (3) present the methods used to calculate the plasma gradients and compare the results of fitting Thomson-scattering data with and without accounting for gradient effects; (4) discuss error analysis and present the results of applying these techniques to the measured scattering spectra; and (5) summarize our findings.

### Thomson-Scattering Measurements

The Thomson-scattering diagnostic on OMEGA consists of a reflective  $f/10$  collection system coupled to two spectrometer/streak-camera pairs.<sup>2</sup> The  $f/6.7$  probe beam ( $\lambda_{4\omega} = 263.25$  nm) had a best-focus diameter of  $\sim 70$   $\mu\text{m}$  (Ref. 20). The spectral resolutions of the IAW and EPW systems were 0.05 nm and 0.5 nm, respectively. The scattering volume was  $\sim 50 \times 50 \times 70$   $\mu\text{m}^3$ . The angle between the probe beam and collection optic was  $120^\circ$ .

Figure 147.17 shows IAW and EPW Thomson-scattering spectra taken during 60-beam ( $\lambda_{3\omega} = 351$ -nm) implosions on the OMEGA laser with the Thomson-scattering diagnostic configured to probe wave vectors perpendicular to the target normal. The targets were 870- $\mu\text{m}$ -diam, 23- $\mu\text{m}$ -thick spherical CH shells filled with 10 atm of  $\text{D}_2$  gas. The laser pulse was a 1.2-ns square pulse preceded by three 100-ps picket pulses with a total energy of 12 kJ. Distributed phase plates<sup>21</sup> were used on each beam to define 860- $\mu\text{m}$  full width at 95% flattop laser spots using  $f/6.7$  lenses.

#### 1. Spectral Sensitivity

The spectral sensitivity of the Thomson-scattering diagnostic was calculated using

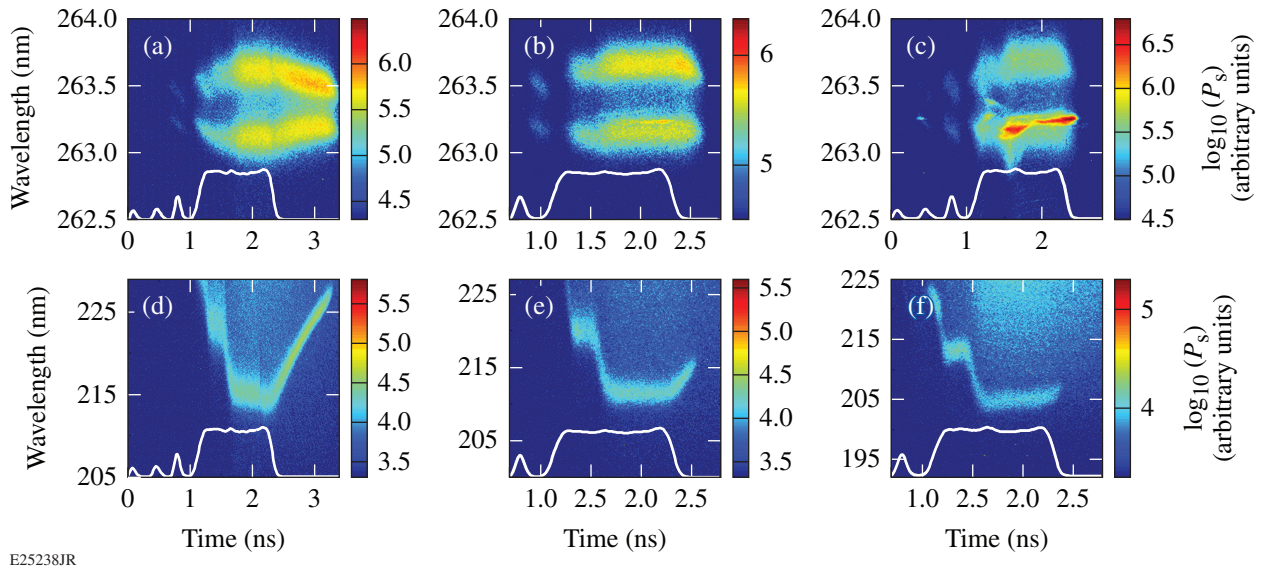
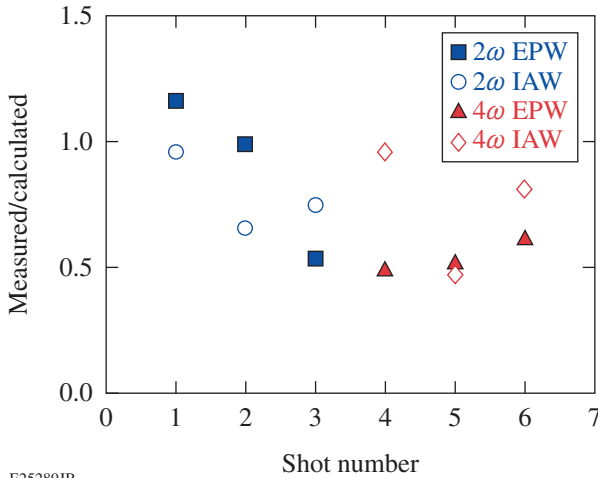


Figure 147.17 Thomson scattering from [(a)–(c)] IAW's and [(d)–(f)] EPW's at [(a),(d)] 400  $\mu\text{m}$ , [(b),(e)] 300  $\mu\text{m}$ , and [(c),(f)] 200  $\mu\text{m}$  from the initial target surface. The drive-laser pulse shape is overlaid. The bright features at  $\sim 263.2$  nm in the IAW spectra correspond to reflected or refracted light from the probe beam.

$$C(\lambda) = \frac{m \cdot k \cdot G \cdot px}{M} \left( \frac{\lambda}{hc} \right) Q(\lambda) T(\lambda) \frac{\text{CCD } e^- \cdot \text{nm}}{\text{pixel} \cdot \text{watt}},$$

the system parameters of which are shown in Table 147.I ( $h = 6.62 \times 10^{-27}$  erg · s). The number of charge-coupled-device (CCD) counts per pixel is given by the product of the sensitivity with the power scattered  $[C(\lambda) \int d\Omega \int dV \partial^3 P_s / \partial \lambda \partial \Omega \partial V]$ , where  $\partial P_s / \partial \lambda = (d\omega / d\lambda) \partial P_s / \partial \omega$  integrated over the scattering volume and the solid angle of the collection optics.

Figure 147.18 shows the ratio of measured-to-calculated signals for a variety of Thomson-scattering configurations (planar and spherical targets using  $2\omega$  and  $4\omega$  probe beams). The predictions are within a factor of 2 of the measured values, which is sufficient for determining appropriate probe energies and filtering when designing experiments. Although the fits shown



E25289JR

Figure 147.18

The ratio of measured-to-calculated peak scattering signals for the IAW and EPW features using  $2\omega$  (526.5-nm) and  $4\omega$  (263.25-nm) probe beams.

in this article were normalized to minimize  $\chi^2$ , it was necessary to account for the spectral sensitivity of the detector when fitting the EPW spectra because the sensitivity varied significantly (factor of 2) over the range of wavelengths included in the fits.

## 2. Background Radiation

The two primary sources of background radiation are bremsstrahlung and Thomson scattering from beams other than the Thomson probe. The two types of background radiation can be distinguished by noting that self-Thomson scattering of the drive beams occurs only when the drive lasers are on, while bremsstrahlung radiation can persist beyond the end of the laser pulse. The background radiation from Thomson scattering of other beams can be calculated using Eq. (1). The differential bremsstrahlung power in watts per unit wavelength ( $\lambda$ ) per unit volume ( $V$ ) per unit solid angle ( $\Omega$ ) is<sup>1</sup>

$$\frac{\partial^3 P_{\text{Br}}}{\partial \lambda \partial \Omega \partial V} = \frac{6.61 \times 10^{-35}}{4\pi} \frac{g Z_{\text{eff}}^2 n_e^2}{\lambda^2 T_e^{1/2}} e^{-0.124/\lambda T_e}, \quad (7)$$

where  $Z_{\text{eff}}^2 = \langle Z^2 \rangle / \langle Z \rangle$ ,  $n_e$  is in  $\text{cm}^{-3}$ ,  $\lambda$  is in cm,  $T_e$  is in keV, and the Gaunt factor  $g \sim 1$ .

Because the background radiation comes from the entire conical volume observed by the Thomson-scattering diagnostic, an accurate calculation of the background radiation requires spatially resolved knowledge of the plasma conditions along the entire line of sight of the Thomson-scattering collection system (Fig. 147.16). For all of the analysis in this article, the bremsstrahlung radiation was calculated by ray tracing simulations from the radiation-hydrodynamics code *LILAC*<sup>22</sup> from the collection optic back through the plasma while integrating Eq. (7) along the rays. The amount of background radiation observed by the diagnostic as a function of the distance from the image plane in the plasma is approximately constant because the col-

Table 147.I: Calibration parameters for the OMEGA Thomson-scattering diagnostic.

Parameter	Symbol	Value	Units
Optical transmission	$T(\lambda)$	$\sim 0.01$	
Photocathode quantum efficiency	$Q(\lambda)$	$\sim 0.1$	Photoelectron/photon
Spectrometer dispersion	$m$	0.002 to 0.03	nm/ $\mu\text{m}$ at PC
Sweep rate	$k$	$1.1 \times 10^{-12}$	s/ $\mu\text{m}$ at CCD
Streak-tube gain	$G$	150	CCD electron/photoelectron
Pixel size	px	170	$\mu\text{m}^2/\text{pixel}$
Tube magnification	$M$	1.3	

PC: photocathode; CCD: charge-coupled device.

lection efficiency of the diagnostic falls off at the same rate as the area of the observed conical cross section increases. For practical estimates, a cylinder with the diameter of the optical aperture stop at the plasma image plane and a length sufficient to include the entire plasma along the view of the collection system is a reasonable background-collection volume.

### Analysis

The plasma parameters in the Thomson-scattering data shown in Fig. 147.17 were inferred by minimizing  $\chi^2 = \int d\lambda [a_s P_s(\lambda) + a_B P_B(\lambda) - P_M(\lambda)]^2$  for a series of spectral lineouts at different times ( $P_s$ ,  $P_B$ , and  $P_M$  are the calculated Thomson-scattered power, the calculated background power, and the measured power, respectively;  $a_s$  and  $a_B$  are normalization coefficients). Distinct normalization coefficients were used for the Thomson-scattered and background radiation because their relative intensities are sensitive to optical alignment. The coefficients were determined by differentiating  $\chi^2$  with respect to  $a_s$  and  $a_B$  and solving the resulting system of equations:

$$a_s \equiv \frac{\left(\int d\lambda P_M P_s\right)\left(\int d\lambda P_B^2\right) - \left(\int d\lambda P_M P_B\right)\left(\int d\lambda P_s P_B\right)}{\left(\int d\lambda P_s^2\right)\left(\int d\lambda P_B^2\right) - \left(\int d\lambda P_s P_B\right)^2},$$

$$a_B \equiv \frac{\int d\lambda P_B^2 (P_M - a_s P_s)}{\int d\lambda P_B^2}.$$

Figure 147.19 shows spectra (averaged over 50 ps) from Figs. 147.17(a) and 147.17(d) taken at 2.8 ns. The spectra are compared to the best-fit spectra calculated with and without

gradients. The IAW fit calculated without gradients is not even qualitatively similar to the measurement, while the EPW spectrum is reasonably well reproduced except in the wings of the spectral peak. The electron temperatures inferred independently from the EPW (1.15-keV) and IAW (0.77-keV) spectra were not self-consistent, and the ion temperature inferred from the IAW (1.62-keV) spectrum was unphysically high for the experimental configuration.

### Gradients

#### 1. Plasma Gradients

When gradients are present, the observed scattered light is a superposition of scattering from the various plasma conditions present within the scattering volume (spatially and temporally). The effects of gradients can be included in calculated spectra by taking a weighted sum of spectra calculated at the various plasma conditions.

The typical plasma parameters that are required to account for gradients within the Thomson-scattering volume are the spatial and temporal derivatives of the fluid velocity and electron density. Two methods of approximating the derivatives are ray-tracing hydrodynamic simulations or using mass and momentum conservation to calculate the gradients iteratively using measured spectra.

The fits shown in Fig. 147.19, where gradients were included, are significantly better than those without gradients (without introducing any additional degrees of freedom). Table 147.II compares plasma parameters inferred from the fits with and without gradients and the results of *LILAC* simulations. When

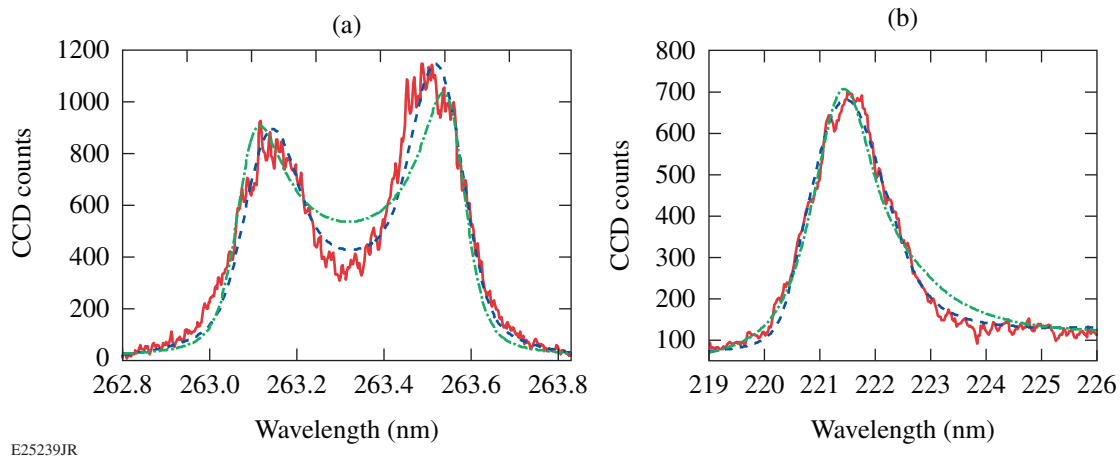


Figure 147.19

Thomson-scattering spectral lineouts at 2.8 ns (400  $\mu\text{m}$  from the target) for scattering from (a) IAW's and (b) EPW's. The solid red curves are the measured spectra, the dashed blue curves are the best fit with gradients included, and the dashed-dotted green curves are the best fit without gradients.

Table 147.II: Comparison of the plasma parameters inferred from the calculated spectra shown in Fig. 147.19. The density is given in  $10^{20} \text{ cm}^{-3}$  and the temperatures are in keV. The plasma was assumed to be completely ionized. The typical error (see **Error**, p. 131) is  $\sim 5\%$  for  $n_e$ ,  $\sim 20\%$  for  $T_e$  from the EPW,  $\sim 5\%$  for  $T_e$  from the IAW, and  $\sim 40\%$  for  $T_i$ .

	EPW fits		IAW fits	
	$n_e$	$T_e$	$T_e$	$T_i$
Gradients	4.40	0.93	0.85	0.82
No gradients	4.04	1.15	0.77	1.62
Simulation	4.45	0.78	0.78	0.58

gradients were included in the fits, the electron temperatures inferred from the IAW and EPW spectra were within 10%, and the ion temperature inferred from the IAW spectrum was slightly lower than the electron temperature, consistent with expectations for a laser-ablated plasma a few hundred picoseconds after the end of the laser pulse. The corresponding simulated plasma parameters shown in Table 147.II were also in better agreement with the inferred values when gradients were included in the fits. The electron density inferred from the EPW spectrum and the electron temperature inferred from the IAW spectrum were relatively insensitive to the effects of gradients.

The gradients in plasma parameters used to calculate the spectra in Fig. 147.19 were assumed to be independent and to have a Gaussian distribution of weights. While the gradients in various plasma parameters are not independent in reality, this assumption is valid when the gradient in a single plasma parameter is dominant. The choice of a Gaussian weight distribution was based on the results of ray-trace calculations and is primarily determined by the use of a Gaussian probe beam.

The plasma gradients were calculated by ray tracing density profiles from hydrodynamic simulations. Rays were traced from the probe to the detector and their overlap on a 3-D grid was used to calculate intensity-weighted histograms of the plasma conditions in the Thomson-scattering volume as a function of time. This technique provided a good approximation to the plasma gradients (both temporal and spatial) and implicitly accounts for the effects of refraction. It allowed for self-consistent comparisons between Thomson-scattering measurements and hydrodynamic simulations by comparing the inferred values from the measurement to the intensity-weighted average value in the calculated interaction volume.

An alternative approach to calculating plasma gradients that avoids relying on hydrodynamic predictions is to calcu-

late the gradients iteratively using the measured spectra. This technique relies on the fact that the density and flow velocity can be determined relatively accurately without knowledge of the gradients. The temporal derivatives of the density and fluid velocity can be determined using time-resolved spectra, and the spatial derivatives can be calculated using conservation of mass and momentum. Assuming that the Thomson-scattering volume is small compared to the relevant scale lengths, the electron density and fluid velocity and their spatial and temporal derivatives can be treated as 1-D constants (spatially) over the scattering volume. The continuity and momentum equations for species  $\alpha$  are

$$\frac{\partial n_\alpha}{\partial t} + \frac{\partial}{\partial x} n_\alpha u_\alpha = 0,$$

$$\frac{\partial u_\alpha}{\partial t} + u_\alpha \frac{\partial u_\alpha}{\partial x} = -\frac{1}{m_\alpha n_\alpha} \frac{\partial}{\partial x} n_\alpha T_\alpha.$$

Defining the mass density ( $\rho \equiv \sum_\alpha m_\alpha n_\alpha$ ) and center-of-mass velocity ( $u \equiv \rho^{-1} \sum_\alpha m_\alpha n_\alpha u_\alpha$ ), assuming  $m_e \ll m_i$ , and solving for the spatial derivatives give

$$\frac{\partial \rho}{\partial x} = \frac{\rho}{u^2 - \eta} \left( \frac{\partial u}{\partial t} - \frac{u}{\rho} \frac{\partial \rho}{\partial t} + \frac{\partial \eta}{\partial x} \right), \quad (8)$$

$$\frac{\partial u}{\partial x} = \frac{u}{u^2 - \eta} \left( \frac{\eta}{\rho u} \frac{\partial \rho}{\partial t} - \frac{\partial u}{\partial t} + \frac{\partial \eta}{\partial x} \right), \quad (9)$$

where  $\eta \equiv (ZT_e + T_i)/m_i$  for a single ion species and  $\eta \equiv [(Z_1 R + Z_2)T_e + (1+R)T_i]/(m_1 R + m_2)$  for two-ion species ( $R \equiv n_1/n_2$ ). These equations are unchanged if the mass density is replaced by the electron density because the constant factor of  $\rho = n_e(m_1 R + m_2)/(Z_1 R + Z_2)$  cancels out. Equations (8) and (9) do not allow for an iterative calculation of the terms involving the spatial gradients in temperature, but these are usually negligible.

## 2. Instrument Effects

Variations in the probed wave vector (because of the finite  $f$  number of the probe and collection optics) can lead to asymmetry in both the amplitude and width of the two IAW peaks. A wave-vector gradient results in asymmetric IAW peaks when variations in the probed wave vector result in the two scattering peaks being shifted by different magnitudes. The source of this asymmetry is the fact that the term corresponding to the propagation of IAW's in Eq. (5) (the first term on the right-

hand side) causes the red- and blue-shifted IAW peaks to shift in opposite directions when the magnitude of the probed wave vector is varied, but the Doppler-shifted term (last term on the right-hand side) shifts both peaks in the same direction. A sufficient condition for wave-vector gradients to cause asymmetry in an IAW spectrum is

$$\left| \frac{\partial \Delta \omega_+}{\partial k} \right| - \left| \frac{\partial \Delta \omega_-}{\partial k} \right| = |c_s - u \cos \theta_f| - |c_s + u \cos \theta_f| \neq 0, \quad (10)$$

where  $\theta_f$  is the angle between the flow velocity and the probed wave vector ( $\mathbf{k}$ ). This inequality is satisfied whenever  $c_s > 0$ ,  $u > 0$ , and  $\cos \theta_f \neq 0$ . This correction has a significant impact when using the IAW feature to infer the relative drift between the ions and electrons.<sup>23</sup>

The range of probed wave vectors was determined by treating the focusing and collection optics as a superposition of point sources and calculating each pairwise interaction. The wave-vector gradients cannot be approximated by 1-D Gaussian distributions because variations in the probed wave vector affect the magnitude of the observed wave vector and

its projection along the fluid velocity. Each pairwise interaction was sorted into a bivariate histogram of wave-vector magnitude and projection along the fluid velocity (100 bins were used).

Figure 147.20 shows spectra calculated with and without gradient/wave-vector effects. To show the amount of broadening introduced by the gradients, the “no-gradients” spectra in Fig. 147.20 correspond to the same plasma parameters as the spectra where gradients were included. The IAW spectra [Fig. 147.20(a)], including the effects of gradients results in a nearly constant amount of spectral broadening because probed wave-vector gradients (which do not vary in time), were the dominant source of broadening. Density gradients cause significant broadening of the EPW spectral peaks [Fig. 147.20(b)] only during the rise of the laser pulse and after the laser is turned off because the temporal gradients vanish and the density scale length is relatively long when the plasma is in steady state.

**Error**

Figure 147.21 shows the electron densities and temperatures inferred from the EPW spectra and the plasma temperatures inferred from the IAW spectra. The plasma parameters predicted by 1-D hydrodynamic simulations (*LILAC*) are shown

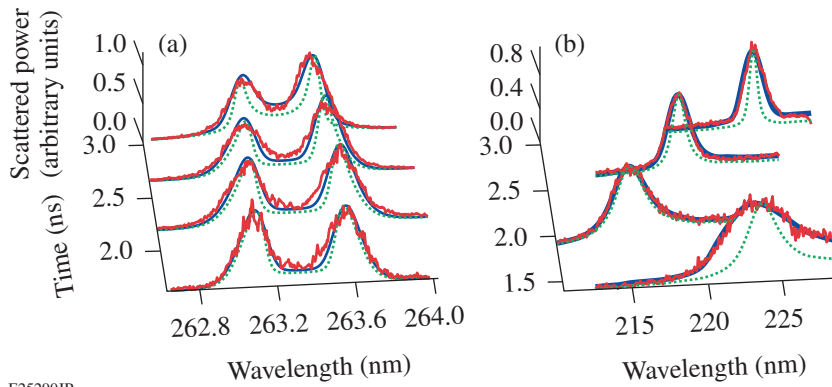


Figure 147.20 Measured spectral lineouts (red) and the corresponding calculated spectra (blue) at several different times for the (a) IAW and (b) EPW collected at 400 μm from the initial target surface. The green dotted curves correspond to calculated spectra using the same plasma parameters as the best-fit curve (blue) but without including gradient/wave-vector effects.

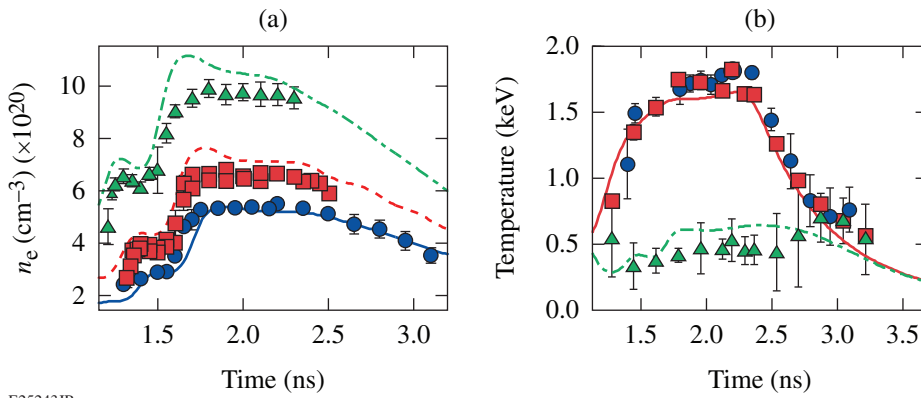


Figure 147.21 (a) Measured (symbols) and simulated (curves) electron density at 400 μm (circles), 300 μm (squares), and 200 μm (triangles) from the initial target surface. (b) Electron temperature inferred from IAW (squares) and EPW (circles) spectra, and ion temperature (triangles) inferred from the IAW spectra at 400 μm. The error in absolute timing is ~100 ps.

as solid curves. Because the error in Thomson-scattering measurements is sensitive to a number of fixed parameters, a Monte Carlo approach was used for the analysis. The inferred plasma parameters and error bars shown in Fig. 147.21 correspond to the mean and standard deviation of 100 fits, where the fixed parameters shown in Table 147.III were varied on each iteration using normally distributed values with variances characteristic to each parameter. The uncertainties shown in Table 147.III are generous estimates because the actual uncertainties (particularly in the gradients, which were the dominant source of error) are not well characterized. The error introduced by noise was accounted for by adding random noise (on each iteration) with variance equal to the variance between the measured spectrum and the initial best fit.

Table 147.III: Uncertainties included in error analysis.

Parameter	Standard deviation
Point-spread function	20%
Spectrometer dispersion	2%
Spectrometer alignment	100 $\mu\text{m}$
Gradients	20%

### Summary

Simultaneous measurements of IAW and EPW Thomson-scattering spectra were obtained using a 263.25-nm probe beam. A fully reflective collection system was used to record light scattered from EPW's at electron densities up to  $10^{21} \text{ cm}^{-3}$ , which produced scattering peaks near 200 nm. An accurate analysis of the experimental Thomson-scattering spectra required accounting for plasma gradients, instrument sensitivity, optical effects, and background radiation. Two methods for calculating plasma gradients using hydrodynamic simulations or by fitting measured spectra iteratively were presented. Fits to measured Thomson-scattering spectra show the importance of including gradient effects. For example, the electron temperature inferred from the EPW feature was overestimated by ~35% when density gradients were neglected. The ion temperature was overestimated by ~50% when gradients in the flow and finite optical effects were neglected. The finite diameter of the probe focusing and collection optics was shown to introduce an asymmetry in the amplitude and width of the IAW features when a plasma flow was present.

### ACKNOWLEDGMENT

This material is based upon work supported by the Department of Energy National Nuclear Security Administration under Award Number DE-NA0001944, the University of Rochester, and the New York State Energy Research and Development Authority.

### REFERENCES

1. D. H. Froula, S. H. Glenzer, N. C. Luhmann, and J. Sheffield, *Plasma Scattering of Electromagnetic Radiation: Theory and Measurement Techniques*, 2nd ed. (Academic Press, Burlington, MA, 2011).
2. J. Katz, R. Boni, C. Sorce, R. Follett, M. J. Shoup III, and D. H. Froula, *Rev. Sci. Instrum.* **83**, 10E349 (2012).
3. S. H. Glenzer *et al.*, *Phys. Rev. Lett.* **82**, 97 (1999).
4. D. S. Montgomery *et al.*, *Phys. Rev. Lett.* **87**, 155001 (2001).
5. D. H. Froula, L. Divol, H. A. Baldis, R. L. Berger, D. G. Braun, B. I. Cohen, R. P. Johnson, D. S. Montgomery, E. A. Williams, and S. H. Glenzer, *Phys. Plasmas* **9**, 4709 (2002).
6. C. E. Clayton, C. Joshi, and F. F. Chen, *Phys. Rev. Lett.* **51**, 1656 (1983).
7. S. H. Glenzer *et al.*, *Phys. Rev. Lett.* **86**, 2565 (2001).
8. D. H. Froula, L. Divol, and S. H. Glenzer, *Phys. Rev. Lett.* **88**, 105003 (2002).
9. K. L. Baker, R. P. Drake, B. S. Bauer, K. G. Estabrook, A. M. Rubenchik, C. Labaune, H. A. Baldis, N. Renard, S. D. Baton, E. Schifano, A. Michard, W. Seka, and R. E. Bahr, *Phys. Rev. Lett.* **77**, 67 (1996).
10. C. Niemann, R. L. Berger, L. Divol, D. H. Froula, O. Jones, R. K. Kirkwood, N. Meezan, J. D. Moody, J. S. Ross, C. Sorce, L. J. Suter, and S. H. Glenzer, *Phys. Rev. Lett.* **100**, 045002 (2008).
11. H. A. Baldis and C. J. Walsh, *Phys. Fluids* **26**, 1364 (1983).
12. R. K. Follett, D. H. Edgell, R. J. Henchen, S. X. Hu, J. Katz, D. T. Michel, J. F. Myatt, J. Shaw, and D. H. Froula, *Phys. Rev. E* **91**, 031104(R) (2015).
13. J. F. Myatt, W. Rozmus, V. Yu. Bychenkov, and V. T. Tikhonchuk, *Phys. Rev. E* **57**, 3383 (1998).
14. J. Zheng, C. X. Yu, and Z. J. Zheng, *Phys. Plasmas* **4**, 2736 (1997).
15. J. Zheng, C. X. Yu, and Z. J. Zheng, *Phys. Plasmas* **6**, 435 (1999).
16. T. E. Tierney IV *et al.*, *J. Phys. A, Math. Gen.* **36**, 5981 (2003).
17. D. R. Nicholson, *Introduction to Plasma Theory*, *Wiley Series in Plasma Physics* (Wiley, New York, 1983).

18. V. N. Goncharov, T. C. Sangster, R. Betti, T. R. Boehly, M. J. Bonino, T. J. B. Collins, R. S. Craxton, J. A. Delettrez, D. H. Edgell, R. Epstein, R. K. Follet, C. J. Forrest, D. H. Froula, V. Yu. Glebov, D. R. Harding, R. J. Henchen, S. X. Hu, I. V. Igumenshchev, R. Janezic, J. H. Kelly, T. J. Kessler, T. Z. Kosc, S. J. Loucks, J. A. Marozas, F. J. Marshall, A. V. Maximov, R. L. McCrory, P. W. McKenty, D. D. Meyerhofer, D. T. Michel, J. F. Myatt, R. Nora, P. B. Radha, S. P. Regan, W. Seka, W. T. Shmayda, R. W. Short, A. Shvydky, S. Skupsky, C. Stoeckl, B. Yaakobi, J. A. Frenje, M. Gatu-Johnson, R. D. Petrasso, and D. T. Casey, *Phys. Plasmas* **21**, 056315 (2014).
19. T. R. Boehly, R. S. Craxton, T. H. Hinterman, J. H. Kelly, T. J. Kessler, S. A. Kumpan, S. A. Letzring, R. L. McCrory, S. F. B. Morse, W. Seka, S. Skupsky, J. M. Soures, and C. P. Verdon, *Rev. Sci. Instrum.* **66**, 508 (1995).
20. A. J. Mackinnon, S. Shiromizu, G. Antonini, J. Auerbach, K. Haney, D. H. Froula, J. Moody, G. Gregori, C. Constantin, C. Sorce, L. Divol, R. L. Griffith, S. Glenzer, J. Satariano, P. K. Whitman, S. N. Locke, E. L. Miller, R. Huff, K. Thorp, W. Armstrong, W. Bahr, W. Seka, G. Pien, J. Mathers, S. Morse, S. Loucks, and S. Stagnitto, *Rev. Sci. Instrum.* **75**, 3906 (2004).
21. T. J. Kessler, Y. Lin, J. J. Armstrong, and B. Velazquez, *Proc. SPIE* **1870**, 95 (1993).
22. J. Delettrez, R. Epstein, M. C. Richardson, P. A. Jaanimagi, and B. L. Henke, *Phys. Rev. A* **36**, 3926 (1987).
23. J. Hawreliak *et al.*, *J. Phys. B: At. Mol. Opt. Phys.* **37**, 1541 (2004).

---

# Measurements of Hot-Electron Temperature in Laser-Irradiated Plasmas

## Introduction

Recently published work<sup>1-3</sup> has studied the production of hot electrons related to the two-plasmon-decay (TPD) instability caused by laser pulse interaction with solid planar targets at an irradiation of  $10^{14}$  W/cm<sup>2</sup>. The hot electrons generated by TPD can preheat the cold compressed core in cryogenic implosions, thereby degrading the final compression and the target performance.<sup>4-6</sup> The first step in evaluating preheat is to determine the hot-electron temperature ( $T_{\text{hot}}$ ). It is required for (a) deducing the total energy in hot electrons from the measured target x-ray radiation ( $K_{\alpha}$  or continuum), and (b) calculating the hot-electron energy deposition in the fuel, i.e., the preheat. In previous work<sup>1-3</sup> we deduced  $T_{\text{hot}}$  from the measured hard x-ray (HXR) spectrum using a three-channel fluorescence-photomultiplier hard x-ray detector (HXRD).<sup>7</sup> The total energy in hot electrons ( $E_{\text{hot}}$ ) was derived from the Mo  $K_{\alpha}$  line intensity from an embedded Mo target. We extend those measurements here by

- a. implementing a new nine-channel hard x-ray image-plate (HXIP) spectrometer to measure the hot-electron temperature more reliably and to derive the total energy in hot electrons. The spectrum is recorded on image plates (IP's) that are absolutely calibrated;<sup>8</sup> this feature makes it possible to derive  $E_{\text{hot}}$  (which was not the case with the uncalibrated HXRD, where  $E_{\text{hot}}$  was derived from  $K_{\alpha}$  measurements).  $T_{\text{hot}}$  is found to be consistently lower (by a factor of 1.5 to 1.7) than the results reported in Ref. 1.
- b. performing experiments to measure  $T_{\text{hot}}$  independently of the x-ray continuum spectrum (using ratios of  $K_{\alpha}$  lines). The results (see  **$K_{\alpha}$  Measurement of  $T_{\text{hot}}$** , p. 138) were consistent with those derived from the continuum spectrum measured by HXIP.
- c. measuring the thermal (softer) x-ray spectrum from the heated plasma and including it in the derivation of the total energy in hot electrons from the high-energy continuum.

- d. demonstrating that the total energy in hot electrons derived from the measurements of  $K_{\alpha}$  and from the high-energy continuum are consistent.

Determining preheat of fusion targets by hot electrons consists of two stages: (1) determining  $T_{\text{hot}}$  and then the total energy in hot electrons (or the total number of hot electrons) and (2) determining the energy deposited by the hot electrons in the compressed, cold target core. The second stage is target specific and is not discussed in this article. The first stage yields a quasi-universal curve of the fraction  $f_{\text{hot}} = E_{\text{hot}}/E_{\text{L}}$  of laser energy ( $E_{\text{L}}$ ) converted to hot electrons. As shown in Ref. 1,  $f_{\text{hot}}$  for planar targets rises steeply from the TPD threshold at a laser intensity of  $\sim 1.5 \times 10^{14}$  W/cm<sup>2</sup> and then saturates at a value of a few percent above  $\sim 7 \times 10^{14}$  W/cm<sup>2</sup>. For spherical targets, the value of  $f_{\text{hot}}$  at a given laser intensity is smaller than it is for planar targets (because the density scale length is smaller in spherical targets). However, when  $f_{\text{hot}}$  is plotted as a function of the calculated TPD linear gain (or, alternatively, as a function of the measured  $T_{\text{hot}}$ ), the measured  $f_{\text{hot}}$  points fall on a quasi-universal curve, independent of the target geometry.<sup>2,3</sup> Therefore, the planar-target measurements in this and previous articles<sup>1-3</sup> are relevant to calculating preheat in spherically imploding fusion targets: the fraction  $f_{\text{hot}}$  (and the concomitant  $T_{\text{hot}}$ ) serves as a source to calculate the transport of hot electrons through the target at hand.

We used two methods to determine the total energy in hot electrons in our planar-target experiments: (1) the emission of  $K_{\alpha}$  lines from an embedded high-Z target layer and (2) from the high-energy bremsstrahlung emission. The targets must be thick enough to capture most of the hot electrons. The targets in these experiments were either 30- $\mu\text{m}$ -thick Mo or 125- $\mu\text{m}$ -thick CH [the targets discussed in  **$K_{\alpha}$  Measurement of  $T_{\text{hot}}$**  (p. 138) were for measuring  $T_{\text{hot}}$ , not  $E_{\text{hot}}$ , and were thicker]. In each case the range of most electrons is smaller than the target thickness, so most of the hot-electron energy is included. The high-Z targets were coated with a 30- $\mu\text{m}$ -thick CH layer;

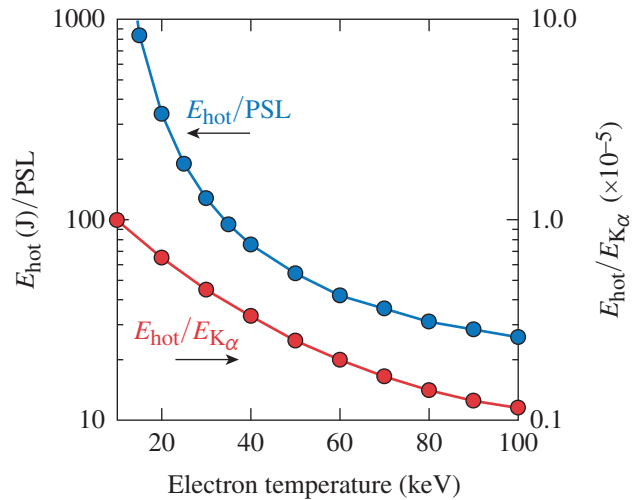
therefore, in all cases the laser interacted with CH, and the production of hot electrons was the same for the same laser intensity and target geometry. In the cases of high-Z targets, it was evident that the laser did not burn through the outer CH layer because of the absence of high-Z lines, except for the inner-shell  $K_\alpha$  transitions, i.e., lines excited by the hot electrons.

Measuring  $E_{\text{hot}}$  in implosion experiments is difficult because (a) a high-Z layer cannot be incorporated into the target core without modifying the desired implosion characteristics and (b) the electrons (mostly those that miss the compressed core) lose a small fraction of their energy in making one pass through the target; this requires knowledge of the hot-electron divergence and refluxing back into the target. Cryogenic targets present an additional complication: even if  $E_{\text{hot}}$  is known, the preheat of the compressed fuel is not simple to derive because most of the HXR radiation is emitted by the CH corona, not the compressed fuel.<sup>9</sup> However, measuring the hot-electron source using thick planar targets makes it possible to calculate the transport of hot electrons through the fusion target at the same TPD gain or the same  $T_{\text{hot}}$ .

High-Z target layers in the previous work served a different purpose than in the present experiments: in the previous experiments, the high-Z  $K_\alpha$  lines were used to determine  $E_{\text{hot}}$  (while the required  $T_{\text{hot}}$  came from HXR, which, being uncalibrated, could not yield  $E_{\text{hot}}$ ). Here,  $T_{\text{hot}}$  comes from HXIP (i.e., from the continuum slope) as well as from  $K_\alpha$  line ratios (in the targets discussed in  **$K_\alpha$  Measurement of  $T_{\text{hot}}$** , p. 138), whereas  $E_{\text{hot}}$  also comes from the absolutely calibrated HXIP.

The laser configuration here was the same as in Ref. 1: four OMEGA EP<sup>10</sup> beams intersected the target at an angle of 23° with respect to the target normal. The laser pulse had a square temporal shape with a width of 2 ns. The irradiance was varied in the range of  $\sim 1$  to  $7 \times 10^{14}$  W/cm<sup>2</sup> by increasing the laser energy in the range of  $\sim 2$  to 9 kJ.

The energy in hot electrons ( $E_{\text{hot}}$ ) was derived from either the  $K_\alpha$  emission from the high-Z layers or the HXR bremsstrahlung radiation (using the calibrated readings of the HXIP). The relation between the measurements and  $E_{\text{hot}}$  was calculated using the *EGSnrc* Monte Carlo code.<sup>11</sup> The code assumes, as input, a Maxwellian hot-electron spectrum that is transported through the planar target. Figure 147.22 shows the calculated ratios of hot-electron energy and radiation yield as well as hot-electron energy and  $K_\alpha$  emission. The blue curve uses the photostimu-



TC12827JR

Figure 147.22

Curves used to determine the total energy in hot electrons for the two methods: using  $K_\alpha$  and using continuum radiation. Shown are Monte Carlo calculations of the energy in hot electrons ( $E_{\text{hot}}$ ) divided by either the measured Mo  $K_\alpha$  energy per unit solid angle in the target normal direction (for targets containing a 30- $\mu\text{m}$ -thick Mo layer) or the photostimulated luminescence (PSL) signal (for thick CH targets) registered by the fifth channel of the hard x-ray image-plate (HXIP) diagnostic. The inverse of these curves is simply the x-ray yield per energy in hot electrons. The x-ray energy is converted to PSL units using the known absolute calibration of the image plates.

lated luminescence unit (PSL) for channel 5 of the HXIP (see the next section). Using the intermediate channel 5 avoids the effect of thermal (or plasma) radiation on the lower channels, as well as the noise effect on the higher channels. Because of the good agreement of simulated and measured channel signals (see **Image-Plate-Based HXR Spectrometer**, p. 136), the same result would have been obtained with any other intermediate channel. The curves fall with increasing electron temperature because the radiation yields increase with  $T_{\text{hot}}$  [the curves rise at temperatures above  $\sim 100$  keV (not shown in Fig. 147.22)]. Figure 147.22 can be used to determine  $E_{\text{hot}}$  (provided  $T_{\text{hot}}$  is known) because the x-ray yields for both the crystal x-ray spectrometer (XRS),<sup>1</sup> used to measure the Mo  $K_\alpha$  line, and the image plates<sup>8</sup> are absolutely calibrated. The sharper fall of the HXIP (blue) curve was shown to be mitigated when the thermal radiation was included in the analysis (see **The Fraction of Laser Energy Converted to Hot Electrons**, p. 140). The blue curve in Fig. 147.22 assumes a 125- $\mu\text{m}$ -thick CH target; the red curve is for a 30- $\mu\text{m}$ -thick CH coating over 30- $\mu\text{m}$ -thick Mo. If the HXIP is used with a target containing a high-Z layer, the HXR is emitted primarily by the high-Z material and the blue curve will be lower by a factor  $Z$  since the HXR yield from a

thick target is proportional to  $Z$ .<sup>12</sup> For low hot-electron temperatures, the thermal plasma emission (which is not calculated by the Monte Carlo code) is not negligible with respect to the hot-electron bremsstrahlung. Therefore, the measured radiation must be corrected before applying the blue curve in Fig. 147.22 (discussed in **The Fraction of Laser Energy Converted to Hot Electrons**, p. 140).

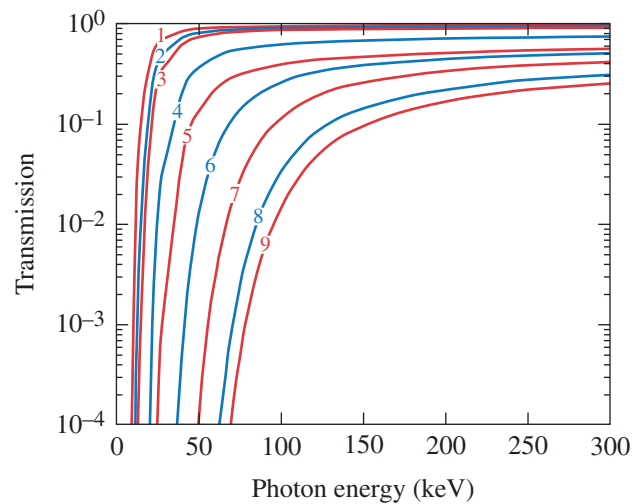
Using planar targets has an advantage over spherical targets: the density scale length  $\left[ \equiv (1/n \, dn/dx)^{-1} \right]$  in these experiments (for the highest intensity) was  $\sim 400 \, \mu\text{m}$  (from 2-D hydrodynamic simulations of the experiments).<sup>1</sup> For a given laser irradiance, the laser energy required to generate a long-scale-length plasma is smaller for planar targets than for spherical targets.<sup>13,14</sup>

### Image-Plate–Based HXR Spectrometer

The hot-electron temperature was measured by a nine-channel instrument (HXIP) using an image plate as a detector. Image plates<sup>8</sup> contain an x-ray–sensitive layer of phosphor  $\text{BaF}(\text{Br},\text{I}):\text{Eu}^{2+}$ . Recorded data are read in the photostimulated luminescence (PSL) process. The sensitivity of image plates was shown to be linear over five orders of magnitude in intensity.<sup>15</sup> The HXIP is contained in a 3/4-in.-thick lead enclosure to reduce background radiation from other radiation sources in the vacuum tank, including scattered target radiation. Additionally, the inside faces of the lead were covered, sequentially, by copper, aluminum, and Mylar layers to attenuate fluorescence from the walls. The spectral decomposition of the target radiation is achieved by an array of nine filters (aluminum and copper of different thicknesses) placed halfway between the target and the image-plate detector, with a total distance between the target and the image plate of 49 cm. Figure 147.23 shows the x-ray transmission curves of the nine filters. Figure 147.24 shows a typical image obtained on the HXIP. A single image plate records the nine projections through the filters (the signals) as well as the background. The background measured outside the nine squares is a result of Compton scattering of target radiation from the components within the HXIP enclosure and fluorescence from these components (primarily the lead walls). An additional background is caused by smearing (or bleeding) from the IP laser scanning. One advantage of using an IP-based system is that the total background is recorded and can be subtracted from the signals. The background is significant for only the last few channels (i.e., highest photon energy). For the first few channels the relative background intensity is  $<1\%$ , for the intermediate channels it is  $<5\%$ , and for the last channels it is  $\sim 50\%$  of the signals. Therefore, knowing the background is essential to determining a reliable temperature. If the background is not fully subtracted, the inferred temperature will be

too high. One indication that the 2-D background subtraction is valid is that the resulting net signals are uniform over the square area of even the last channels.

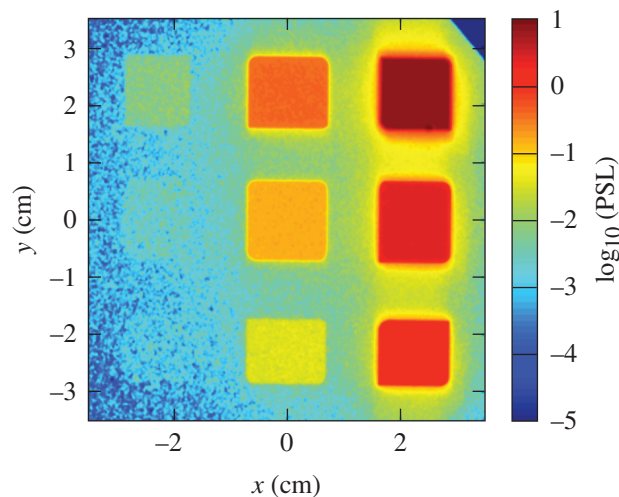
The wall layers behind and close to the IP are one source of background radiation that requires special attention. Radiation that traverses the IP is absorbed into the back wall and scattered; fluorescent radiation enters the IP from its back. Monte Carlo



TC12828JR

Figure 147.23

X-ray transmission of HXIP channels 1 to 9 (left to right) as a function of the photon energy. Higher-number channels are sensitive to progressively higher photon energies.



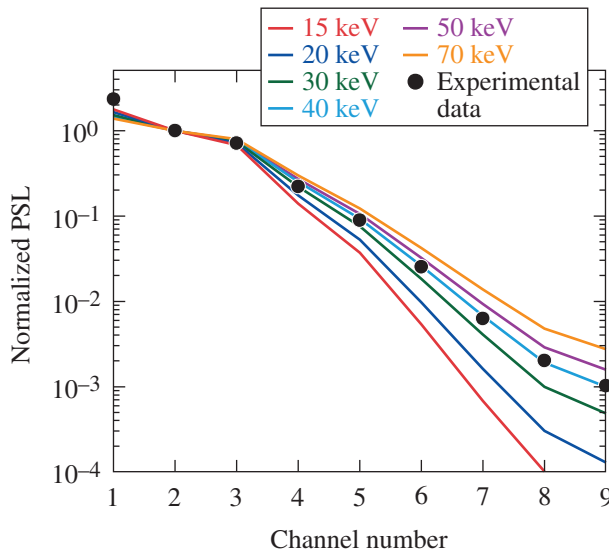
TC12829JR

Figure 147.24

A typical image (logarithmic intensity scale) obtained on an HXIP. The signals from nine channels are seen, as well as a background around and between the signals. The ability to subtract the background around each channel image makes it possible to correctly determine the emitted spectrum.

simulations show that the back-wall radiation is not uniform over the scale of the signal size (15 mm × 15 mm) because of the proximity; however, its intensity is about 20× lower than the total signal for any of the channels and is therefore unimportant.

Since the scattered radiation is removed from the net signals, they reflect only the transmission through the filters, which can be calculated without a Monte Carlo simulation. Figure 147.25 shows the calculated response curves for several hot-electron temperatures. The target HXR radiation spectrum is assumed to be a single exponential of the temperature  $T_{\text{hot}}$ . The measurements at each channel agree well with the best-fit curve, suggesting that the exponential assumption is valid. Therefore, in calculating the energy in hot electrons from Fig. 147.22, any channel (above the first) should give the same result. The signal curve relating to the HXIP in Fig. 147.22 corresponds to channel 5. This channel was chosen because lower channels are burdened by the plasma thermal radiation and by bound-free absorption in high-Z layers; also, higher channels may be too weak for reliable measurement. The filters for channel 5 absorb strongly below ~20 keV; this is the reason for the steep drop in the HXIP curve in Fig. 147.22. A special case is the first channel, which includes the radiation tail from the thermal plasma. This is why we normalized the curves and the data points to the second (rather than the first) channel.

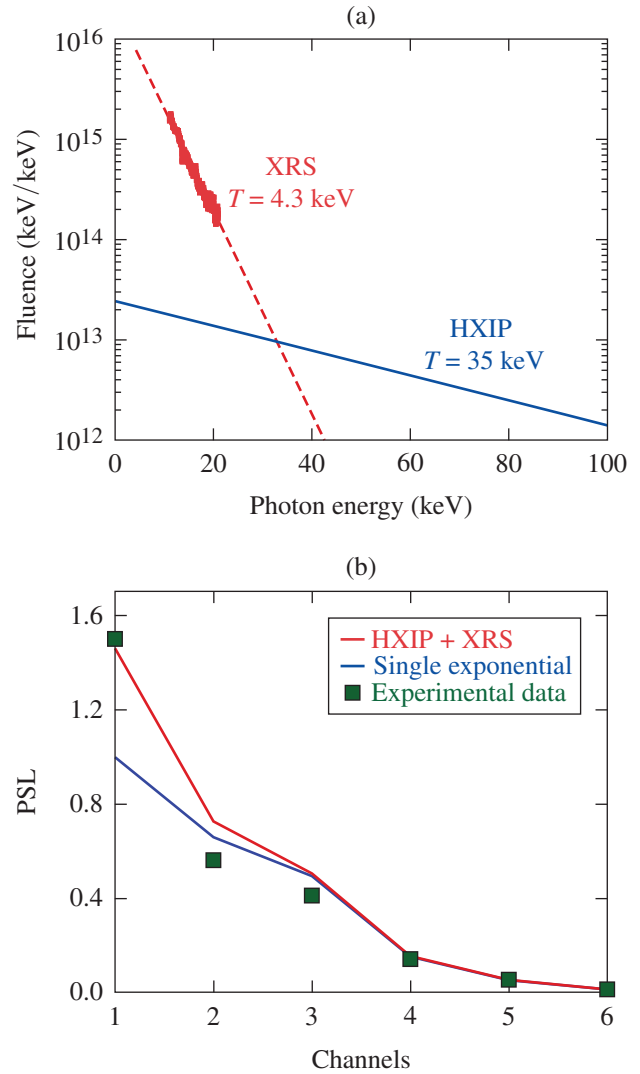


TC12830JR

Figure 147.25

A typical example of determining hot-electron temperature using the HXIP data. The curves represent the nine-channel data, calculated by using the filter transmissions and measured image-plate (IP) sensitivity. To determine the hot-electron temperature, the curves of PSL data were normalized to the channel 2 data. Channel 1's excess signal is explained by the plasma thermal emission.

To demonstrate the role of the thermal radiation, Fig. 147.26(a) shows the simultaneous HXR spectrum deduced from the HXIP and the tail of the thermal spectrum measured using XRS. The irradiance for this shot was  $6 \times 10^{14} \text{ W/cm}^2$ . The HXIP spectrum (which was assumed to be exponential) was obtained using the temperature from Fig. 147.25 and was normalized to the measured channel 5 signal. The target in Fig. 147.26 was CH; for a target with a higher-Z layer, the intensity of the induced component in Fig. 147.26(a) would be higher by about a fac-

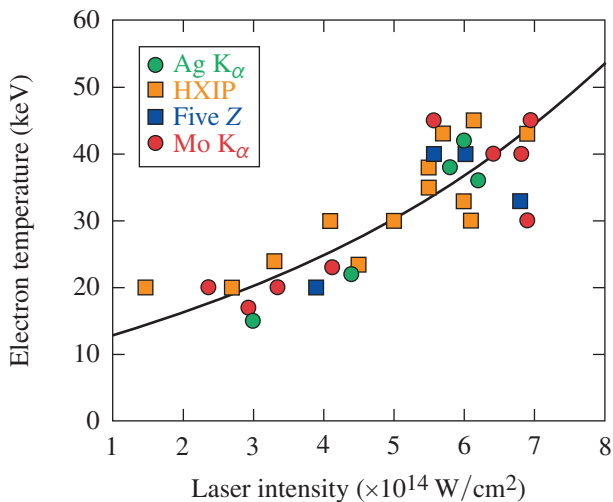


TC12831JR

Figure 147.26

(a) The tail of the plasma-emission spectrum measured by the x-ray spectrometer (XRS) diagnostic (red line) and the hard x-ray (HXR) radiation emitted by hot electrons, as deduced from the HXIP measurement (blue line). (b) Using the sum of the two spectra in (a) as the input spectrum, the simulated channel signals (red curve) reproduce the measured HXIP data, including channel 1 (solid green squares), unlike the single-exponential spectrum (blue curve).

tor of Z, while the thermal plasma radiation would not change since the laser interaction in all cases is in the CH coating. Figure 147.26 illustrates that using HXIP alone to deduce the hot-electron temperature is valid if the first channel is excluded from the fitting procedure. Figure 147.26(b) shows the result of replacing the assumed single HXR exponential with the sum of the two exponentials in Fig. 147.26(a). The inclusion of the thermal spectrum with the calculated HXIP data agrees with the measured points for all channels, including channel 1. Figure 147.26(a) also shows that for low  $T_{\text{hot}}$  ( $<30$  keV), the two spectra must be untangled (discussed in **The Fraction of Laser Energy Converted to Hot Electrons**, p. 140). For most fusion experiments, the relevant temperature is much higher and the low-temperature case is of interest only for exploring the TPD instability threshold. Figure 147.27 shows the compilation of temperature measurements from different shots as a function of the laser intensity. The temperatures inferred using HXIP measurements are represented by the orange squares. The other points in Fig. 147.27 are discussed in the next section.



TC12832JR

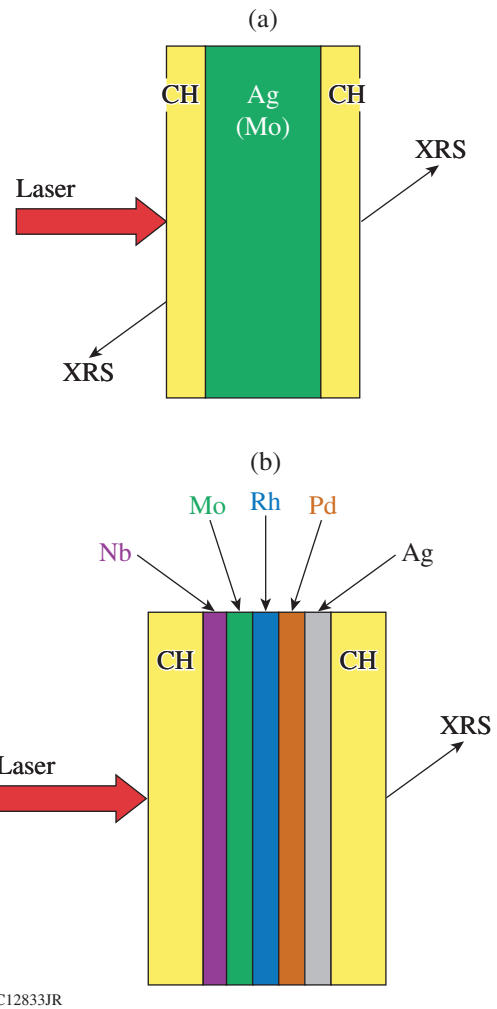
Figure 147.27  
Compilation of measured hot-electron temperatures. The curve serves to guide the eye.

### $K_{\alpha}$ Measurement of $T_{\text{hot}}$

Because of the discrepancy in temperature obtained by the HXRD (see Fig. 8 of Ref. 1) and HXIP, we designed three experiments to measure  $T_{\text{hot}}$  in a way that does not depend on the continuum radiation. Figure 147.28 shows the target configuration for the three experiments.

#### 1. Thick Molybdenum Target

The target in this experiment consisted of 100- $\mu\text{m}$ -thick molybdenum, coated with 30  $\mu\text{m}$  of CH on both sides. The Mo



TC12833JR

Figure 147.28  
Target configurations for three experiments designed to measure the hot-electron temperature using  $K_{\alpha}$  emission from high-Z targets (not drawn to scale): (a) Thick molybdenum and silver targets. The targets consist of 100- $\mu\text{m}$ -thick molybdenum (127- $\mu\text{m}$ -thick silver), coated with 30  $\mu\text{m}$  of CH on both sides. The measured quantities are the ratios of  $K_{\alpha}$  emission from the front and rear of the target. (b) Five-element target. The target consists of five layers (Nb, Mo, Rh, Pd, and Ag), 5  $\mu\text{m}$  thick each, coated with 30  $\mu\text{m}$  of CH on both sides. The measured quantity is the  $K_{\alpha}$  for increasing-Z elements.

thickness was larger than the range for most hot electrons, so the Mo  $K_{\alpha}$  line was attenuated while traveling to the back of the target. For lower hot-electron temperatures, the  $K_{\alpha}$  is emitted closer to the front surface, consequently being absorbed more when exiting from the back. Therefore, the ratio of the Mo  $K_{\alpha}$  yields from the front and back of the target decreases with increasing  $T_{\text{hot}}$ . The ratio as a function of  $T_{\text{hot}}$  is calculated by the Monte Carlo code and shown in Fig. 147.29(a). The directions of the angles are with respect to the target normal. In the experiment, the laser intensity was varied and the calculated

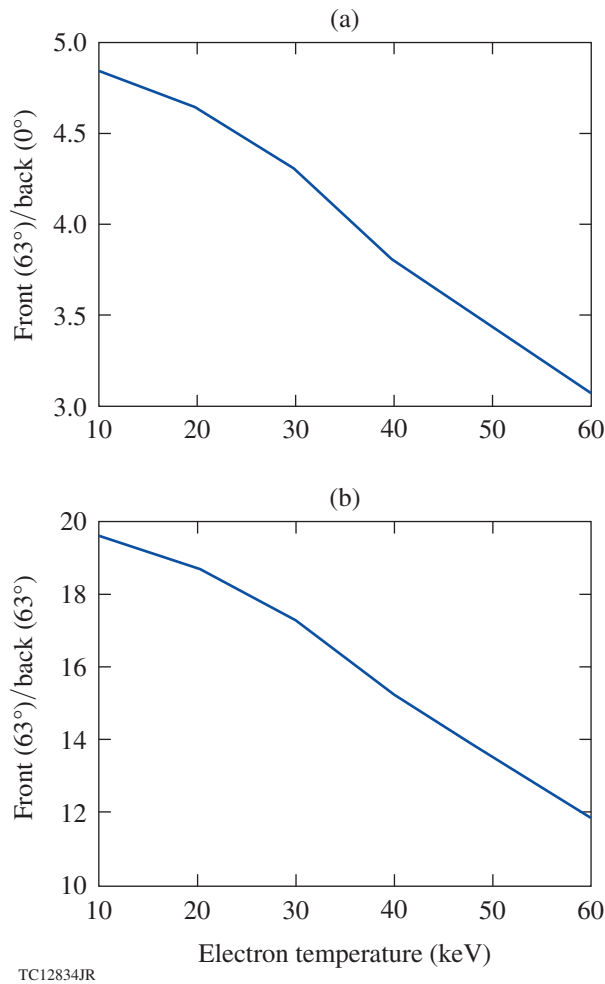


Figure 147.29

The ratios of Mo  $K_{\alpha}$  and Ag  $K_{\alpha}$  yields from the front and of the thick (a) Mo and (b) Ag targets, in the direction toward the detectors, as functions of the hot-electron temperature, calculated by the Monte Carlo code. The direction angles are with respect to target normal.

ratio was used to determine the hot-electron temperature. The resulting temperatures are shown by the solid red circles in Fig. 147.27.

## 2. Thick Silver Target

A 127- $\mu\text{m}$ -thick silver layer replaced the molybdenum layer in the previous experiment. The Monte Carlo-calculated ratio of the Ag  $K_{\alpha}$  yields from the front and back of the target is shown in Fig. 147.29(b). The higher K edge of Ag (25 keV) as compared with Mo (20 keV) reduces the fraction of coronal radiation available for  $K_{\alpha}$  excitation and, therefore, supports ruling it out as a significant contributor to the observed  $K_{\alpha}$  line (further discussed later in this section). The temperature results obtained are shown by the solid green circles in Fig. 147.27.

## 3. Five-Element Target

This target consists of five layers (Nb, Mo, Rh, Pd, and Ag), 5  $\mu\text{m}$  thick each, coated with 30  $\mu\text{m}$  CH [Fig. 147.28(b)]. The five corresponding  $K_{\alpha}$  lines are measured using XRS behind the target. The five layers are of increasing  $Z$  in the direction of the incident laser ( $Z = 41, 42, 45, 46, 47$ ). Each  $K_{\alpha}$  line of a given  $Z$  can excite the  $K_{\alpha}$  lines of the lower- $Z$  layers but not of the higher- $Z$  layers. The main effect is the decrease in the number of hot electrons as they move in the direction of the laser. Therefore, the XRS at the back of the target measures five  $K_{\alpha}$  lines of decreasing intensity for increasing  $Z$  (see Fig. 147.30). This decrease is slower for a higher hot-electron temperature. The Monte Carlo code simulations of hot-electron transport through this target are used to derive  $T_{\text{hot}}$  from the rate of  $K_{\alpha}$  intensity drop as a function of  $Z$  (see Fig. 147.31). The resulting temperatures are shown by the solid blue squares in Fig. 147.27.

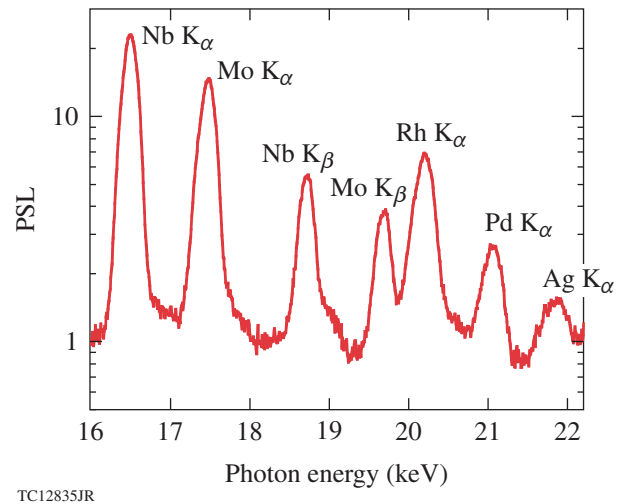
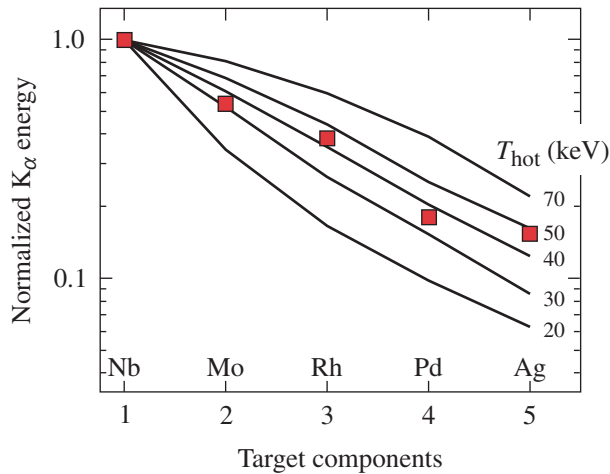


Figure 147.30

An example of the x-ray spectrum from a five-element target, as measured by XRS. The  $K_{\alpha}$  lines are used to determine the hot-electron temperature.

In addition to hot electrons,  $K_{\alpha}$  lines can also be excited by radiation, both thermal radiation from the plasma and bremsstrahlung radiated by the hot electrons. Only the latter, however, is accounted for in the Monte Carlo simulations. Therefore, plasma radiation's contribution to the  $K_{\alpha}$  intensity must be shown to be negligible. A clear indication that the  $K_{\alpha}$  lines in our experiments are excited primarily by hot electrons and their radiation and not by plasma radiation is seen in the laser-intensity dependence of the  $K_{\alpha}$  lines. Figure 6 of Ref. 1 shows that for a rise in the laser intensity by a factor of  $\sim 2$ , the Mo  $K_{\alpha}$  intensity rises by almost a factor of  $10^4$  (see also the related Fig. 147.34 below). On the other hand, the plasma



TC12836JR

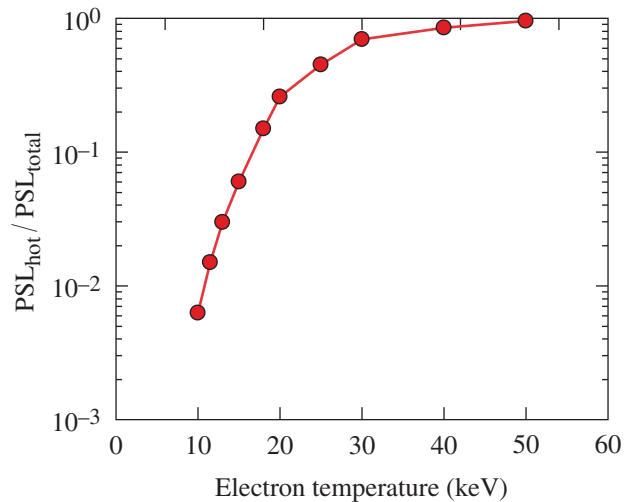
Figure 147.31

Monte Carlo curves of  $K_\alpha$  intensity for the five elements in the target, normalized to the first element. The data (for a laser irradiance of  $6 \times 10^{14} \text{ W/cm}^2$ ) indicate  $T_{\text{hot}} \sim 40 \text{ keV}$ .

continuum intensity increases about linearly with the laser intensity, indicating that its contribution to the  $K_\alpha$  excitation is negligible. An additional indication of the ratio between the two radiations in a pure CH target is seen in Fig. 147.26(a). For  $T_{\text{hot}}$  higher than  $\sim 20 \text{ keV}$ , the hot-electron curve rises sharply (because of increased hot-electron production at higher intensities) and the continuum above the K edge of, say, Ag (25 keV) will be dominated by the hot-electron bremsstrahlung.

### The Fraction of Laser Energy Converted to Hot Electrons

As seen in Fig. 147.26(a), the total measured x-ray yield includes a contribution from the thermal-plasma radiation, which is not included in the Monte Carlo code calculations. Therefore, the measured radiation should be corrected (reduced) before using the blue curve in Fig. 147.22 to deduce the energy in hot electrons. This correction is especially important at low hot-electron temperatures, where the hot-electron bremsstrahlung drops very fast. Figure 147.32 shows the correction factor; i.e., the ratio  $R = \text{PSL}_{\text{hot}} / \text{PSL}_{\text{total}}$  of hot-electron-induced radiation and total radiation (including the thermal-plasma radiation), measured in channel 5, as a function of  $T_{\text{hot}}$ . The correction factor  $R$  is calculated using the measured composite x-ray spectra, like those of Fig. 147.26(a): the spectrum (with and without the plasma component) is multiplied by channel 5, filters transmission and the IP sensitivity, and then integrated over photon energies. This ratio can be approximated as  $R = -0.521 + 4.81 \times 10^{-2} \times T_{\text{hot}} - 3.59 \times 10^{-4} \times T_{\text{hot}}^2$ , where  $T_{\text{hot}}$  is in keV. The results are shown in Fig. 147.32.



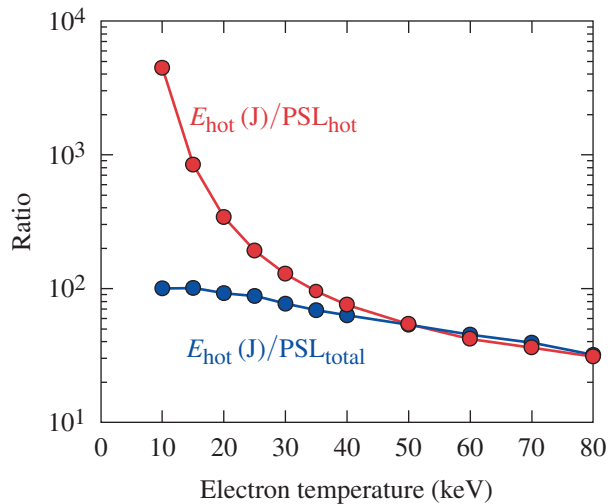
TC12837JR

Figure 147.32

Relative contribution of the plasma electrons and the hot electrons to the measured total x-ray spectrum. Experimental curves such as the two curves shown in Fig. 147.26(a), for various laser intensities, are convolved with the HXIP sensitivity of channel 5; plotted is the ratio of the signal caused by hot electrons alone and that caused by the hot electrons plus the plasma radiation. As the hot-electron temperature drops, so does the relative contribution of hot-electron radiation to the total measured x-ray yield.

Using the correction factor  $R$ , the HXIP curve in Fig. 147.22 can now be modified to allow for the contribution of the plasma radiation with the results shown in Fig. 147.33. The red curve is the corresponding blue curve from Fig. 147.22, shown as reference. To use this curve, the experimental radiation must be corrected for the plasma radiation. The blue curve in Fig. 147.33 was obtained by multiplying the red curve by the correction factor (Fig. 147.32). When using the blue curve in Fig. 147.33, the total measured channel 5 readings must be used (without subtracting the thermal contribution). The corrected curve indicates that the dependence of the hot-electron yield on hot-electron temperature is weak. Therefore, the discrepancy between the HXR and HXIP temperature results (see the **Introduction**, p. 134) is not very important when calculating the energy in hot electrons; however, the penetration depth of hot electrons, relevant to preheat calculation, remains important.

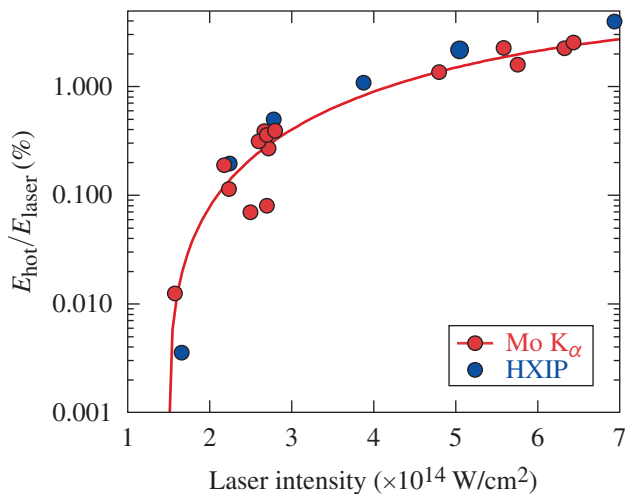
To verify the validity of the present derivation of hot-electron energy, Fig. 147.34 compares the fraction of laser energy converted into hot electrons ( $f_{\text{hot}}$ ) using the present HXIP results (blue circles) and previous Mo  $K_\alpha$  results<sup>1</sup> (red circles). The HXIP results refer to 125- $\mu\text{m}$ -thick CH targets, whereas the Mo  $K_\alpha$  results refer to CH-coated Mo targets. The tempera-



TC12838JR

Figure 147.33

The blue curve in Fig. 147.22 is adjusted to include the contribution of the thermal radiation, using the results of Fig. 147.32. The red curve here reproduces the unadjusted Fig. 147.22 curve. Since that curve shows  $E_{\text{hot}}/\text{PSL}_{\text{hot}}$  and Fig. 147.32 shows the ratio  $\text{PSL}_{\text{hot}}/\text{PSL}_{\text{total}}$ , the product of these quantities is  $E_{\text{hot}}/\text{PSL}_{\text{total}}$  and is represented here by the blue curve. When the adjusted, measured channel 5 signal is used, the resulting  $E_{\text{hot}}$  is seen to depend only weakly on  $T_{\text{hot}}$ .



TC12839JR

Figure 147.34

The fraction of total laser energy converted to energy in hot electrons. The red circles represent the data from Ref. 1, using the Mo  $K_{\alpha}$  line from a CH-coated Mo target, with  $T_{\text{hot}}$  corrected based on the laser-intensity scaling found in the present experiments. The blue circles represent data from a 125- $\mu\text{m}$ -thick CH target, using the HXR continuum measured by HXIP. The results indicate that these two methods of deducing  $E_{\text{hot}}$  are equivalent.

ture values in the older experiment were corrected using the scaling with laser intensity obtained in this experiment. The agreement shows that the method for measuring hot-electron energy using the HXIP (corrected for the thermal radiation) is consistent with the method in Ref. 1 using Mo  $K_{\alpha}$  lines. The agreement also shows that the production of hot electrons in CH-coated Mo is very similar to that in thick CH targets. It should be noted that the large possible error in  $f_{\text{hot}}$  (because of the thermal contribution) near the threshold can be tolerated because of the steep rise, and that typical fusion implosion experiments correspond to the upper end of the intensity range in Fig. 147.34, where the thermal contribution is negligible.

### Conclusion

This article extends our previous measurements<sup>1-3</sup> of the temperature and total energy of laser-generated hot electrons, using 2-ns UV pulses at  $10^{14}$  W/cm<sup>2</sup> on the OMEGA EP laser.<sup>1-3</sup> The three-channel fluorescence-photomultiplier detector (HXRD) was replaced with a nine-channel image-plate-based detector (HXIP). For the same conditions, the measured temperatures are lower than those measured using a HXR by a factor of  $\sim 1.5$  to 1.7. This measurement was supplemented with three experiments that measured the hot-electron temperature using  $K_{\alpha}$  emission from high-Z target layers. These experiments gave temperatures that were consistent with those measured using the HXIP. The lower hot-electron temperatures, however, do not significantly impact the deduced total energy in hot electrons when the effect of the thermal plasma radiation on bremsstrahlung measurements is taken into account.

Lower temperatures mean that the simulated preheat in cryogenic spherical implosions, using HXR temperatures, could be overestimated, however, since lower  $T_{\text{hot}}$  entails smaller penetration into the target core. In fact, recent cryogenic experiments<sup>16</sup> show that the preheat is smaller than predicted (by measuring the degradation in areal density compared to the one predicted), and even the preheat remains small when the production of hot electrons increases significantly. This could be caused by reduced penetration of hot electrons into the core.

While the fraction of laser energy converted into hot electrons is found to increase up to 1% to 3% with the laser intensity, other factors can contribute to lowering the preheat of the cold dense shell in spherical implosions, such as a large angular divergence of the hot electrons.<sup>17</sup> High-Z ablaters are capable of reducing the production of hot electrons because of a shorter scale length and a higher plasma temperature.<sup>18</sup>

## ACKNOWLEDGMENT

This material is based upon work supported by the Department of Energy National Nuclear Security Administration under Award Number DE-NA0001944, the University of Rochester, and the New York State Energy Research and Development Authority.

## REFERENCES

1. B. Yaakobi, P.-Y. Chang, A. A. Solodov, C. Stoeckl, D. H. Edgell, R. S. Craxton, S. X. Hu, J. F. Myatt, F. J. Marshall, W. Seka, and D. H. Froula, *Phys. Plasmas* **19**, 012704 (2012).
2. D. H. Froula, B. Yaakobi, S. X. Hu, P.-Y. Chang, R. S. Craxton, D. H. Edgell, R. Follett, D. T. Michel, J. F. Myatt, W. Seka, R. W. Short, A. Solodov, and C. Stoeckl, *Phys. Rev. Lett.* **108**, 165003 (2012).
3. D. H. Froula, D. T. Michel, I. V. Igumenshchev, S. X. Hu, B. Yaakobi, J. F. Myatt, D. H. Edgell, R. Follett, V. Yu. Glebov, V. N. Goncharov, T. J. Kessler, A. V. Maximov, P. B. Radha, T. C. Sangster, W. Seka, R. W. Short, A. A. Solodov, C. Sorce, and C. Stoeckl, *Plasma Phys. Control. Fusion* **54**, 124016 (2012).
4. J. D. Lindl, *Inertial Confinement Fusion: The Quest for Ignition and Energy Gain Using Indirect Drive* (Springer-Verlag, New York, 1998), Chap. 11.
5. *LLE Review Quarterly Report* **79**, 121, Laboratory for Laser Energetics, University of Rochester, Rochester, NY, LLE Document No. DOE/SF/19460-317, NTIS Order No. DE2002762802 (1999).
6. V. A. Smalyuk, D. Shvarts, R. Betti, J. A. Delettrez, D. H. Edgell, V. Yu. Glebov, V. N. Goncharov, R. L. McCrory, D. D. Meyerhofer, P. B. Radha, S. P. Regan, T. C. Sangster, W. Seka, S. Skupsky, C. Stoeckl, B. Yaakobi, J. A. Frenje, C. K. Li, R. D. Petrasso, and F. H. Séguin, *Phys. Rev. Lett.* **100**, 185005 (2008).
7. C. Stoeckl, V. Yu. Glebov, D. D. Meyerhofer, W. Seka, B. Yaakobi, R. P. J. Town, and J. D. Zuegel, *Rev. Sci. Instrum.* **72**, 1197 (2001).
8. A. L. Meadowcroft, C. D. Bentley, and E. N. Stott, *Rev. Sci. Instrum.* **79**, 113102 (2008).
9. A. R. Christopherson, R. Betti, W. Theobald, and J. Howard, "Probing Hot Electron Preheat and Hot Spot Asymmetries in ICF Implosions," the Ninth International Conference on Inertial Fusion Sciences and Applications (IFSA 2015), Seattle, WA, 20–25 September 2015 (Paper Th.O.2.2).
10. *LLE Review Quarterly Report* **125**, 37, Laboratory for Laser Energetics, University of Rochester, Rochester, NY, LLE Document No. DOE/NA/28302-993 (2010).
11. I. Kawrakow, *Med. Phys.* **27**, 485 (2000); I. Kawrakow, E. Mainegra-Hing, D. W. O. Rogers, F. Tessier, and B. R. B. Walters, "The EGSnrc Code System: Monte Carlo Simulation of Electron and Photon Transport," National Research Council Canada, Ottawa, Canada, NRCC Report PIRS-701 (May 2011).
12. K. A. Brueckner, *Phys. Rev. Lett.* **36**, 677 (1976); R. P. Drake, R. E. Turner, B. F. Lasinski, E. A. Williams, K. Estabrook, W. L. Krueer, E. M. Campbell, and T. W. Johnston, *Phys. Rev. A* **40**, 3219 (1989); T. Döppner *et al.*, *Phys. Rev. Lett.* **108**, 135006 (2012).
13. D. T. Michel, A. V. Maximov, R. W. Short, J. A. Delettrez, D. Edgell, S. X. Hu, I. V. Igumenshchev, J. F. Myatt, A. A. Solodov, C. Stoeckl, B. Yaakobi, and D. H. Froula, *Phys. Plasmas* **20**, 055703 (2013).
14. D. T. Michel, A. V. Maximov, R. W. Short, S. X. Hu, J. F. Myatt, W. Seka, A. A. Solodov, B. Yaakobi, and D. H. Froula, *Phys. Rev. Lett.* **109**, 155007 (2012).
15. J. Miyahara *et al.*, *Nucl. Instrum. Methods Phys. Res. A* **246**, 572 (1986).
16. V. N. Goncharov, T. C. Sangster, R. Betti, T. R. Boehly, M. J. Bonino, T. J. B. Collins, R. S. Craxton, J. A. Delettrez, D. H. Edgell, R. Epstein, R. K. Follett, C. J. Forrest, D. H. Froula, V. Yu. Glebov, D. R. Harding, R. J. Henchen, S. X. Hu, I. V. Igumenshchev, R. Janezic, J. H. Kelly, T. J. Kessler, T. Z. Kosc, S. J. Loucks, J. A. Marozas, F. J. Marshall, A. V. Maximov, R. L. McCrory, P. W. McKenty, D. D. Meyerhofer, D. T. Michel, J. F. Myatt, R. Nora, P. B. Radha, S. P. Regan, W. Seka, W. T. Shmayda, R. W. Short, A. Shvydky, S. Skupsky, C. Stoeckl, B. Yaakobi, J. A. Frenje, M. Gatu-Johnson, R. D. Petrasso, and D. T. Casey, *Phys. Plasmas* **21**, 056315 (2014).
17. B. Yaakobi, A. A. Solodov, J. F. Myatt, J. A. Delettrez, C. Stoeckl, and D. H. Froula, *Phys. Plasmas* **20**, 092706 (2013).
18. R. K. Follett, J. A. Delettrez, D. H. Edgell, V. N. Goncharov, R. J. Henchen, J. Katz, D. T. Michel, J. F. Myatt, J. Shaw, A. A. Solodov, C. Stoeckl, B. Yaakobi, and D. H. Froula, *Phys. Rev. Lett.* **116**, 155002 (2016).

# A Pulse-Front-Tilt-Compensated Streaked Optical Spectrometer with High Throughput and Picosecond Time Resolution

## Introduction

Time-resolved spectroscopy, using an optical spectrometer coupled to a streak-camera recording system, is a common diagnostic technique in the field of short-pulse laser physics research. Streaked spectrometers analyze a point-source input by aligning the dispersed output of the spectrometer to the input slit of a streak camera. These instruments are particularly effective for single-shot experiments requiring detailed measurements of optical spectra with temporal resolutions of the order of picoseconds to nanoseconds. The overall temporal resolution of such instruments depends on the streak camera's performance and the configuration of the spectrometer used. For many demanding applications, a streaked-spectrometer instrument must have high spectral and temporal resolution while maintaining large optical throughput. These three parameters are intrinsically linked and the ability to simultaneously optimize them is limited. This article presents a novel technique that decouples throughput considerations from the spectral- and temporal-resolution optimization process.

## Background of Pulse-Front Tilt

Pulse-front tilt (PFT) is a time-shearing effect inherent to angular dispersion in which the arrival time of light varies linearly with position across the beam in the plane of dispersion.<sup>1,2</sup> PFT can be explained geometrically by examining the path-length difference introduced across the beam at a dispersive interface (Fig. 147.35). In the case where a diffraction grating is used to generate angular dispersion, the total PFT after dispersion is given by

$$\Delta t = Nm\lambda / c, \quad (1)$$

where  $N$  is the total number of illuminated grating grooves,  $m$  is the grating order used,  $\lambda$  is the wavelength of light, and  $c$  is the speed of light. An important quantity in spectrometer design is the angular dispersion that relates the change in angle of diffraction  $\beta$  to the change in wavelength and is given by

$$d\beta / d\lambda = mG / \cos(\beta). \quad (2)$$

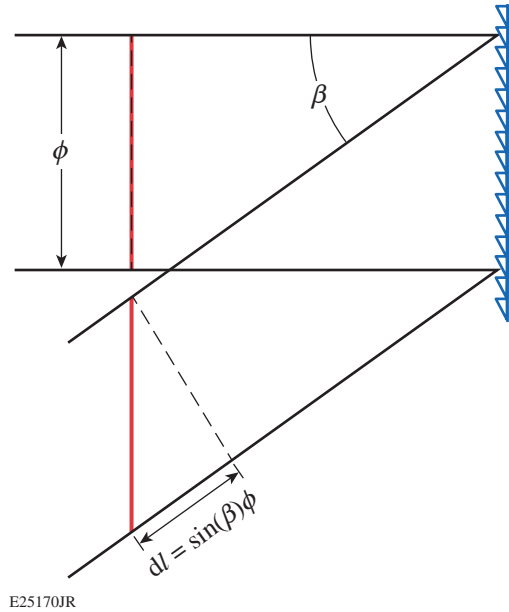


Figure 147.35

Pulse-front tilt (PFT) is introduced by the path-length asymmetries of a beam exiting an angularly dispersive medium. The total PFT increases with beam diameter and angular dispersion.

Combining Eqs. (1) and (2), and relating  $N$  to the beam diameter  $\phi$  and groove density  $G$ , produces an expression that illustrates the difficulty of designing a spectrometer with high spectral resolution, good temporal resolution, and large throughput:

$$\Delta t = \frac{\phi \lambda \cos(\beta)}{c} \frac{d\beta}{d\lambda}. \quad (3)$$

For a given angular dispersion, attempts to improve throughput by increasing the size of the collection optic will result in a loss of temporal resolution.

## Spectral- and Temporal-Resolution Limitations

The size of an individual spectral-resolution element can be defined as the product of the instrument's spatial impulse response multiplied by the linear dispersion ( $\delta\lambda = \Delta x d\lambda/dx$ ). The linear dispersion ( $d\lambda/dx$ ) is the product of the angular

dispersion and the output image's focal length. The imaging performance of the spectrometer, the point-spread function (PSF<sub>SC</sub>) of the streak camera, and the size of the input object's image ( $wM$ ) all contribute to the spatial impulse response. Adding these terms in quadrature gives

$$\Delta x^2 = (wM)^2 + \text{PSF}_{\text{geo}}^2 + \text{PSF}_{\text{dif}}^2 + \text{PSF}_{\text{SC}}^2, \quad (4)$$

where  $w$  is the size of the input object,  $M$  is the magnification of the spectrometer along the axis of dispersion, and  $\text{PSF}_{\text{geo}}$  and  $\text{PSF}_{\text{dif}}$  are the geometric and diffractive limitations, respectively, of the spectrometer imaging optics. It is worth noting that, for a fixed collection aperture, attempts to improve spectral resolution by using a longer output focal length will increase  $M$  if asymmetric conjugates are used or will increase PFT if symmetric conjugates are used.

Three main mechanisms generally limit the temporal resolution of a streak camera: (1) the line-spread transit (LST) time, (2) electron transit time spread (TTS), and (3) space-charge broadening. LST is defined as the time it takes the sweep to traverse the width of a static cathode image and can be reduced by using a fast sweep rate and a narrowly focused cathode image. TTS arises because electrons generated at the photocathode have a distribution of initial velocity vectors and do not take the same amount of time to reach the phosphor output screen. TTS can be decreased by reducing the overall transit time or narrowing the excess electron energy distribution through judicious choice of photocathode material and/or signal wavelengths. Space-charge broadening is caused by the repulsive force felt from neighboring photoelectrons as they travel down the tube. Space-charge broadening spoils the image of the cathode and effectively increases the achieved LST. This

effect can be managed by keeping the total electron-current density below an experimentally determined threshold level.

### Segmented Spectrometer Design

Using a rectangular mask to limit the beam size and, therefore, the total number of grooves illuminated at the grating surface is a viable technique to decrease total PFT.<sup>3</sup> While simple and effective, this method reduces system throughput and is not suitable for low-signal applications. Additionally, decreasing the beam size increases the imaging  $f$  number. When taken to the extreme, the masked aperture generates a large diffraction-limited spot size that spoils the instrument's spectral resolution. This result is consistent with the concept that spectral resolving power is directly proportional to the number of illuminated grating grooves.

A new type of spectrometer layout is proposed that uses the concept of a masked grating aperture to improve temporal resolution but maintains the throughput of an unmasked system. This is accomplished by breaking the full-aperture beam into a series of discrete rectangular segments. Each segment is prescribed an appropriate amount of delay, such that after the beam exits the dispersive medium, the individual segments are temporally aligned. Figure 147.36 shows how a transmission echelon optic is used to generate the required delay profile to compensate the overall PFT. The residual PFT is only what is accumulated across a single segment. The temporal delay between each segment is determined by the step height of the echelon optic and is set to be equal to the total PFT of a single segment. The practical limitations to the minimum echelon step width are the same as for a masked spectrometer. The echelon step width is minimized until the diffraction-limited spot size is comparable to the other contributing terms in the spectrometer's PSF.

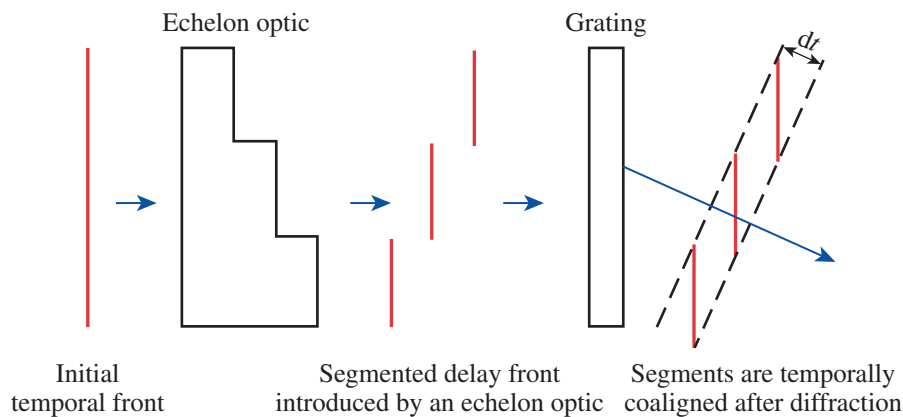


Figure 147.36 PFT can be reduced with no loss to throughput by segmenting the incoming beam into multiple sub-elements that are individually delayed to compensate for the path-length difference introduced by the diffraction grating. The residual PFT is limited to the accumulation across a single segment and the overall temporal resolution is improved by a factor equal to the number of sub-elements used.

E25172JR

## Spectrometer Design

A prototype segmented spectrometer (Fig. 147.37) has been designed to support the development of a fiber-optic Thomson-scattering system at LLE. Thomson scattering will be used to characterize the growth of electron plasma waves in pump-probe experiments that last less than 25 ps. The spectrometer was designed to match the 1-ps temporal resolution of the Rochester Optical Streak System 8200 (Ref. 4). The spectrometer provides a 100-nm spectral field of view centered at the 527-nm Thomson-scattering probe wavelength with a 0.8-nm spectral resolution. Light from the plasma-wave experiment will be coupled to the spectrometer using a gradient-index fiber optic. The fiber has a 50- $\mu\text{m}$  core diameter and a 0.2 ( $f/2.5$ ) numerical aperture. The input signal is collimated by a 225-mm-focal-length, color-corrected doublet lens operating at  $f/2.9$ . Angular dispersion is provided by a 300-g/mm transmission grating that generates 40 ps of pulse-front tilt. A 34-element reflective echelon optic with 2.2-mm step widths and 174- $\mu\text{m}$  step heights is used to improve the achievable temporal resolution to 1.2 ps. Individual spectrometer segments focus to the streak camera at  $f/100$ , producing diffraction-limited spot sizes of 55- $\mu\text{m}$  full width at half maximum (FWHM). Figure 147.38 shows how the echelon step width was optimized to improve temporal

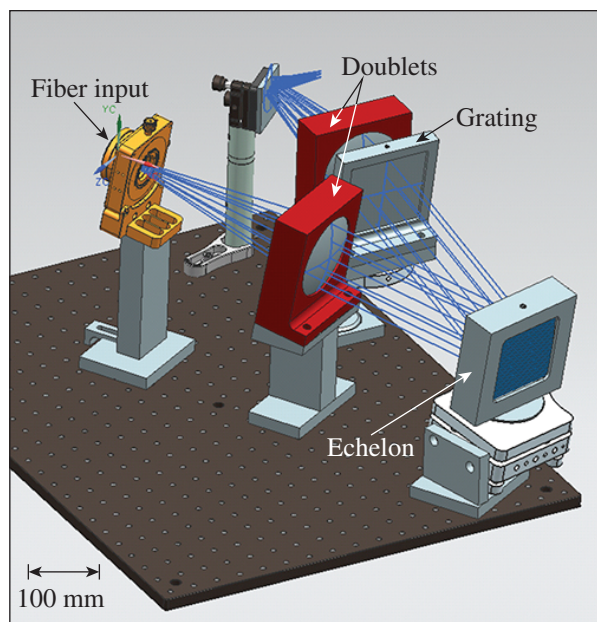


Figure 147.37  
CAD model of the spectrometer layout. A pair of  $f/2.9$  doublets collimate and focus the dispersed input from a 50- $\mu\text{m}$ -core fiber optic. The PFT from the 300-g/mm transmission grating is reduced by using a 34-element reflective echelon optic.

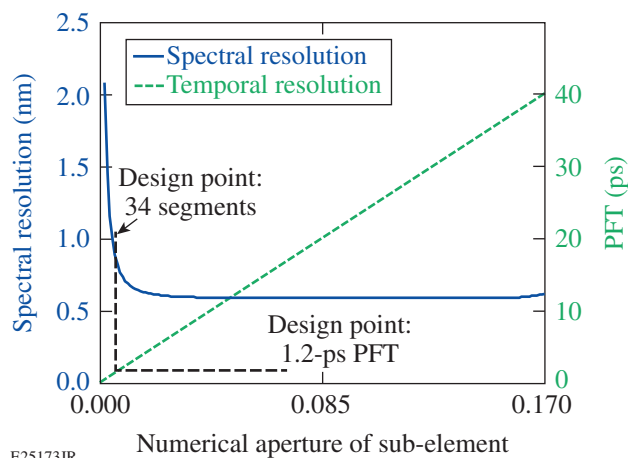


Figure 147.38  
Spectral resolution is determined by convolving the modeled imaging-performance parameters and multiplying by linear dispersion. The overall beam size was selected based on the geometric limitations of the imaging optics. Temporal resolution was improved by segmenting the full beam into properly delayed sub-elements. The design point represents a compromise between these factors, resulting in 0.8-nm spectral resolution, 1.2-ps temporal resolution, and  $f/2.9$  throughput.

resolution while maintaining spectral resolution close to the performance of the nominal full-aperture system.

## Conclusions

This article presents a novel spectrometer design that decouples the relationship between throughput and pulse-front tilt. An echelon optic is used to segment the aperture of the spectrometer into a series of sub-elements that are optically and temporally co-aligned. This technique makes it possible to optimize the spectral resolution, throughput, and temporal resolution simultaneously.

## ACKNOWLEDGMENT

This material is based upon work supported by the Department of Energy National Nuclear Security Administration under Award Number DE-NA0001944, the University of Rochester, and the New York State Energy Research and Development Authority. The support of DOE does not constitute an endorsement by DOE of the views expressed in this article.

## REFERENCES

1. J. Hebling, *Opt. Quantum Electron.* **28**, 1759 (1996).
2. S. Akturk, X. Gu, P. Bownan, and R. Trebino, *J. Opt.* **12**, 093001 (2010).
3. A. Visco, R. P. Drake, D. H. Froula, S. H. Glenzer, and B. B. Pollock, *Rev. Sci. Instrum.* **79**, 10F545 (2008).
4. Sydor Instruments, LLC, Rochester, NY 14624.

# Design of an Extreme Ultraviolet Spectrometer Suite to Characterize Rapidly Heated Solid Matter

## Introduction

Solid-density hot plasmas can be created by using a high-intensity laser incident on a solid metal foil.<sup>1</sup> Following irradiation by the high-intensity laser, the target heats in a matter of picoseconds. Electrons in the laser's focal spot are rapidly energized and confined to a target volume by a sheath set up around the target. The fast electrons thermalize through collisional and noncollisional processes that occur much faster than the hydrodynamic expansion time scale. This makes it possible to heat the target to high temperatures before the onset of hydrodynamic motion, allowing one to measure the hot plasma in a pre-expanded state. These conditions form a platform for measuring intrinsic material properties such as the equation of state (EOS) of high-energy-density (HED) matter.

X-ray and ultraviolet spectroscopy have been used to extract information about the temperature and density evolution of hot, solid-density targets in a variety of conditions. A new extreme ultraviolet (XUV) spectrometer has been built to make temperature measurements that provide complementary information to higher-energy spectroscopic observations (e.g.,  $K_{\alpha}$ -line spectroscopy or thermal-line radiation) of the mass-averaged temperature. The XUV radiation is highly localized to the surface of the promptly heated material before expansion. The early-time heating dynamics of the target are important to understand for future off-Hugioniot EOS measurements.

## Spectrometer Layout

Figure 147.39 provides a schematic overview of the spectrometer and camera layout. A high-throughput XUV spectrometer was realized using a grazing-incidence toroidal reflector and a variable line-space grating.<sup>2</sup> A precision-cut 100-mm  $\times$  2-mm slit<sup>3</sup> is held close to the target with a re-entrant nose cone. All direct lines of sight between the target interaction and the charge-coupled-device (CCD) detector are shielded by a minimum of 6-mm tungsten to minimize the noise from hard x-ray hits on the camera. Two limited apertures inside the spectrometer serve to limit stray light. The spectrometer consists of a modular front section that can be mounted to a scientific CCD camera (Spectral Instruments SI-800), an image plate, or an x-ray streak camera. Two identical spectrometers have been built for simultaneous time-averaged and time-resolved XUV emission studies.

The spectrometer consists of a 450-lines/mm, variable line space grating<sup>2</sup> and a toroidal mirror,<sup>2</sup> which images the spectrum to a flat-field detector located outside the target chamber. Both the grating and mirror operate at a grazing angle of 7.5°. The mirror and the detector plane are located 190 mm and 570 mm from the laser focus, respectively. The view angle for both spectrometers is 45° with respect to the optical axis of the incident laser. The solid angle of both spectrometers is limited by the toroidal reflector and is  $3 \times 10^{-3}$  sr; the spectrometer

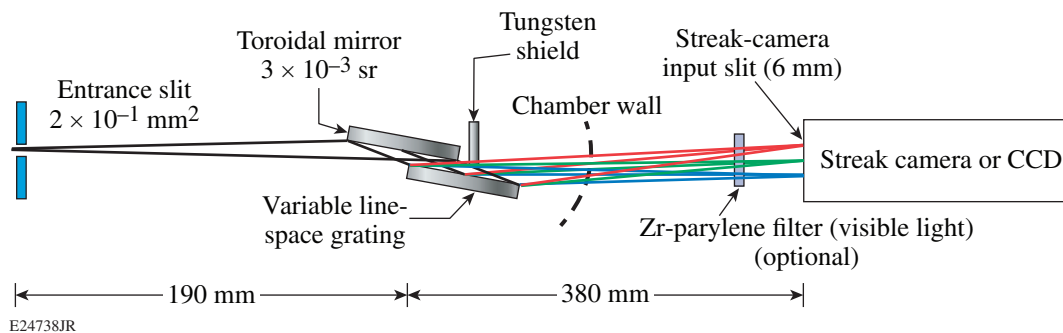
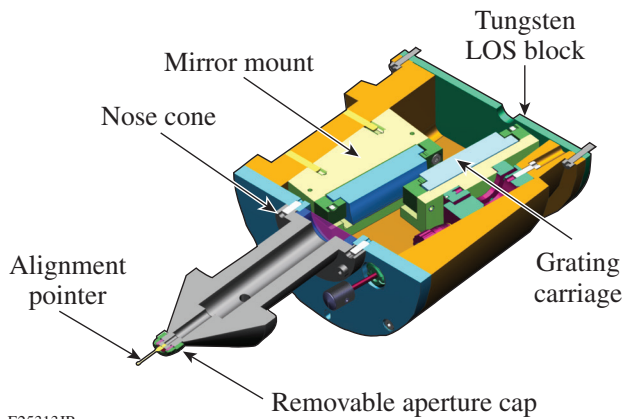


Figure 147.39  
Schematic diagram of the extreme ultraviolet (XUV) flat-field spectrometer. CCD: charge-coupled device.

has a magnification of 3, giving a field of view of  $\sim 500 \mu\text{m}$  in the target plane. A ray-trace model of the spectrometer was implemented in the code *FRED* to simulate the optical performance of the spectrometer.<sup>4</sup> The simulation predicts a spectral resolution of 0.1-nm full width at half maximum (FWHM) at 12.5 nm.

Figure 147.40 shows a schematic of the spectrometer with the top sectioned for clarity. The slit aperture is held in place with a threaded cap on the front nose cone. The cap may be removed to replace or inspect the aperture slit between shots. A pointer can be attached to the nose cone to aid in spectrometer alignment on the target chamber's viewing system. The cone-shaped projection on the front of the spectrometer body limits blast material from the experiment from depositing into the spectrometer or onto the fine-adjust knobs of the grating carriage. The toroidal mirror is pinned in place on a custom kinematic mounting. The grating can be rotated  $\pm 3^\circ$  about two axes to allow for pointing and spectral window adjustment. The actuators for the tip/tilt adjustment pass through to the front end to allow for adjustment between shots when the chamber



E25313JR

Figure 147.40  
Schematic of the re-entrant spectrometer's front end. LOS: line of sight.

is vent cycled. The outer casing of the spectrometer is vented with sintered plugs to allow for venting during pump out. The tungsten line-of-sight (LOS) shield forms the rear panel on the enclosure and provides a limited aperture for the spectrum to pass through to the detector.

### Experiment

An experiment to validate the spectrometer performance and to measure short-pulse heating was conducted on LLE's Multi-Terawatt (MTW) Laser System.<sup>5,6</sup> The experimental setup is shown schematically in Fig. 147.41. A  $100 \times 100 \times 3\text{-}\mu\text{m}$  Al foil was irradiated with  $7 \pm 1 \text{ J}$  of 527-nm light in a 1-ps pulse with a contrast ratio of  $\sim 10^{14}$ . The contrast is estimated by measuring the pulse contrast at the fundamental frequency and calculated for the second-harmonic process.<sup>7</sup> The laser delivered a focus with 80% of the energy contained into a  $10\text{-}\mu\text{m}$  spot when measured on a low-power shot. The on-target intensity was  $\sim 3 \times 10^{18} \text{ W/cm}^2$ . The XUV photocathode on the streak camera was a  $200\text{-}\text{\AA}$  gold layer flash coated onto a  $0.5\text{-}\mu\text{m}$  parylene base layer. The full photocathode slit measures  $60 \text{ mm} \times 200 \mu\text{m}$  wide but typically only the central  $6 \text{ mm} \times 50 \mu\text{m}$  of the slit is used when the camera is set for best temporal focusing.

### Data Analysis

Figure 147.42 shows a time-integrated spectrum taken with the spectrometer onto a FUJI TR image-plate (IP) detector. The spectrum occupies  $\sim 1 \text{ mm}$  on the IP detector in the direction opposite the spectrum; the values shown are the summed values from the scanned data. The IP was scanned at a resolution of  $50 \mu\text{m}$  and a sensitivity level of 10,000. Several atomic transition lines from Al III, IV, and V ions are visible superimposed on the continuum emission in this time-integrated shot. The strongest lines observed are listed in Table 147.IV; these values were obtained from the National Institute of Standards and Technology (NIST)<sup>8</sup> wavelength database. The Al III transition was observed in absorption

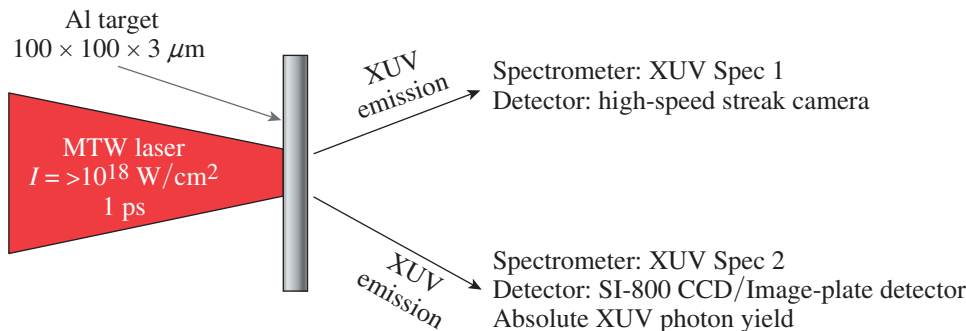
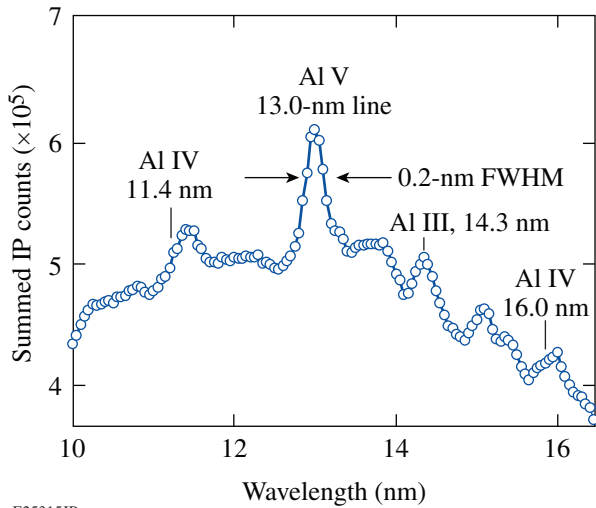


Figure 147.41  
Schematic diagram of the experimental setup.  
MTW: Multi-Terawatt.

E24735JR



E25315JR

Figure 147.42

Spectrum acquired on a 7-J, 1-ps laser shot onto a  $100 \times 100 \times 3\text{-}\mu\text{m}$  Al target. The spectrometer resolution was measured to be 0.2-nm full width at half maximum (FWHM).

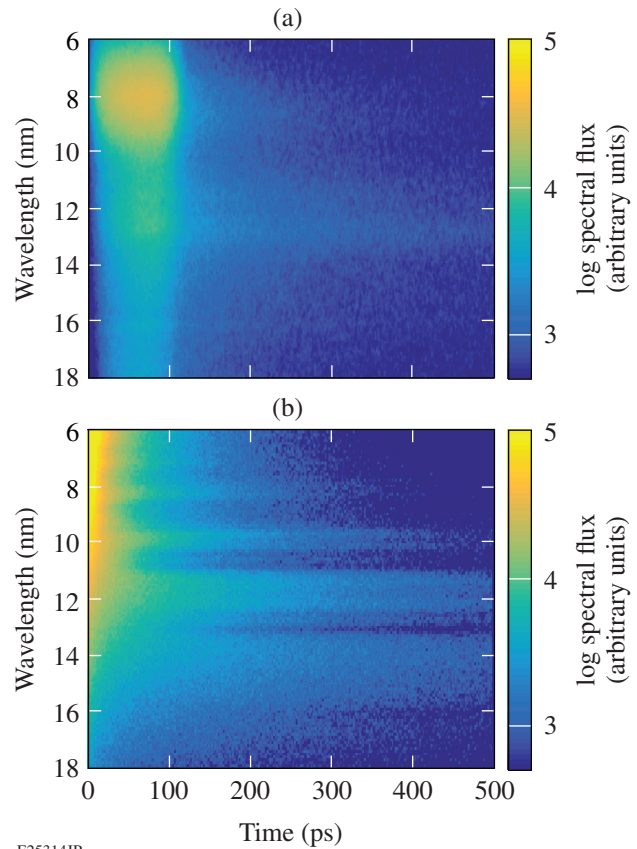
Table 147.IV: Aluminum atomic spectral lines identified in a short-pulse, heated aluminum target.

Ion	Experimental data (nm)	Reference data <sup>8</sup> (nm)	Relative intensity <sup>8</sup>	Oscillator strength <sup>8</sup>
Al IV	$11.4 \pm 0.2$	11.646	250	0.332
Al V	$13.0 \pm 0.2$	13.0847	1000	0.175
Al IV	$16.0 \pm 0.2$	16.169	700	0.017
Al III	$14.3 \pm 0.2$	14.395	—	—

only and no tabular data exist for the line strength or relative intensity. Additionally, the spectrometer resolution at 13.0 nm was measured to be 0.2-nm FWHM. The Al line at 13.0 nm is a doublet (13.0 and 13.1 nm) and some broadening of the peak is expected; however, the resolution at this wavelength is consistent with simulation predictions (0.2 nm versus 0.1 nm). The peak at 15.1 nm is likely O IV ions from an oxide layer on the surface of the target.

Figure 147.43 compares a time-resolved spectrum recorded on an MTW shot and a synthetic spectrum. For this comparison we used the collisional-radiative code *Spect3D* to compute the emergent radiation from the radiation–hydrodynamics simulation.<sup>9</sup> The XUV atomic model in *Spect3D* includes all ionization stages and excited-state energy levels. A radiation–hydrodynamics simulation was run with parameters closely

tied to the experiment.<sup>10</sup> In the simulation, a uniform energy density corresponding to the electron deposition was applied to the solid metal target and allowed to freely expand. The target temperature was initialized in the simulation at 100 eV. The emission is assumed to be in local thermodynamic equilibrium. In the time period of interest, the emission is predicted to be dominated by a smooth continuum with all the atomic transitions dissolved into the continuum. Later in time, the strongest emissions from ground-state transitions are observed. Previous inferences of temperature from the emission in this region have shown significant departures between the temperature observed in the continuum and electronic line ratios in time-integrated XUV spectrum measurements.<sup>11,12</sup> The streaked data here show that the continuum and line radiation occur at substantially different times in the expansion. This may explain the discrepancy between the temperature inferred from line emission and continuum emission.



E25314JR

Figure 147.43

Comparison of (a) streaked XUV data and (b) simulation.

The streaked spectra can be corrected for the wavelength-dependent photocathode sensitivity. The first step is to take a photometric calibration of the streaked spectrometer. A method similar to those described in Ref. 13 will be implemented when correcting the raw streak-camera data. During a shot, the streaked and time-integrated spectrometer acquires a spectrum. The spectrum captured, on a calibrated IP detector, is then compared to a streaked spectrum summed in the temporal direction. Grating efficiency as a function of wavelength will be corrected using a rigorous coupled-wave theory code, taking into account the groove shape, depth, and metal reflectivity.<sup>14</sup>

### Conclusion

A spectrometer capable of measuring the time-resolved XUV emission of a rapidly heated metal target has been designed and implemented. The spectrometer has a measured resolution of 0.2 nm at a design wavelength of 13 nm. The time-resolved spectra show reasonable agreement with radiation-hydrodynamic simulations. Future experiments will further explore the surface-temperature dynamics of these targets in a variety of metals.

### ACKNOWLEDGEMENT

This material is based upon work supported by the Department of Energy National Nuclear Security Administration under Award Number DE-NA0001944, the University of Rochester, and the New York State Energy Research and Development Authority. This work was performed under the auspices of the U.S. Department of Energy, Office of Science, Office of Fusion Energy Sciences Award Number DE-SC-0012317.

### REFERENCES

1. R. G. Evans *et al.*, Appl. Phys. Lett. **86**, 191505 (2005).
2. HORIBA Scientific, Edison, NJ 08820-3097.
3. National Aperture, Inc. Salem, NH 03079.
4. *FRED*, Photon Engineering, LLC, Tucson, AZ 85711 <http://www.photonengr.com/software> (1 June 2016).
5. V. Bagnoud, I. A. Begishev, M. J. Guardalben, J. Puth, and J. D. Zuegel, Opt. Lett. **30**, 1843 (2005).
6. C. Dorrer, I. A. Begishev, A. V. Okishev, and J. D. Zuegel, Opt. Lett. **32**, 2143 (2007).
7. I. A. Begishev, C. R. Stillman, S. T. Ivancic, S.-W. Bahk, R. Cuffney, C. Mileham, P. M. Nilson, D. H. Froula, J. D. Zuegel, and J. Bromage, "Efficient Second-Harmonic Generation of Large-Aperture Multi-Terawatt Hybrid Nd: Laser Subpicosecond Pulses for Laser-Matter Interactions," to be submitted to Applied Physics.
8. NIST Atomic Spectra Database, NIST Standard Reference Database #78, Version 5, see <http://www.nist.gov/pml/data/asd.cfm> (1 June 2016).
9. J. J. MacFarlane *et al.*, High Energy Density Phys. **3**, 181 (2007).
10. J. Delettrez, R. Epstein, M. C. Richardson, P. A. Jaanimagi, and B. L. Henke, Phys. Rev. A **36**, 3926 (1987).
11. T. Ma *et al.*, Rev. Sci. Instrum. **79**, 10E312 (2008).
12. U. Zastra *et al.*, Phys. Rev. E **78**, 066406 (2008).
13. R. Florido, R. C. Mancini, T. Nagayama, R. Tommasini, J. A. Delettrez, S. P. Regan, V. A. Smalyuk, R. Rodríguez, and J. M. Gil, High Energy Density Phys. **6**, 70 (2010).
14. L. Li *et al.*, Appl. Opt. **38**, 304 (1999).

---

# Influence of Surface Modifications on the Adsorption and Absorption of Tritium into Stainless-Steel 316

## Introduction

High concentrations of tritium develop on stainless-steel (SS) surfaces exposed to a tritium atmosphere.<sup>1</sup> These high concentrations are attributed to tritium dissolution within the adsorbed water layers present on all metal surfaces.<sup>1-4</sup> Tritium dissolved within these layers contributes  $\geq 20\%$  to the total inventory absorbed by SS.<sup>1</sup> Additionally, these water layers govern the migration of the isotope during an exposure to a tritium atmosphere, as well as during a storage period following the exposure. Because such a large fraction of the tritium inventory resides in the water layers, altering these layers by altering the metal surface can significantly affect the total quantity of tritium absorbed by SS.

In the present study, the effect of altering the metal surface on the migration and total absorption of tritium into SS 316 was investigated by preparing SS samples with a variety of surface modifications, which included mechanical polishing, electropolishing (EP),<sup>5,6</sup> gold plating, nitric-acid treatments, and Fe or Cr oxidation.<sup>7</sup> The migration and total absorption of tritium in the various SS samples was measured using plasma-induced ion sputtering<sup>8</sup> and thermal desorption.<sup>9</sup>

A quantitative tritium migration model (QTRIMM) based on Fickian diffusion through composite media is used to describe the measured total tritium inventories and migration rates. The composite medium treated in this model is the adsorbed water layer(s)/metal-lattice system. This model accounts for the high concentrations of tritium on the surfaces of SS by relating the tritium concentrations on the surface and in the metal lattice at the surface/metal-lattice interface.<sup>8</sup>

## Modeling

QTRIMM is based on a numeric solution to the diffusion equation<sup>10</sup> and can be used to calculate the tritium concentration profiles in a metal substrate.<sup>8</sup> The boundary conditions used in this model are based on several fundamental assumptions. The first assumption is that a rapid equilibrium occurs between tritium in the gas phase and tritium dissolved in the adsorbed surface water. The second assumption is that all iso-

tope exchange reactions have equal probability; consequently, there will be equal tritium mole fractions in the gas phase and on the surface. Equal reaction probabilities are not likely because the formation of double-isotope species, such as  $T_2O$ , is not as probable as the formation of a single-isotope species, such as HTO. The consequence of making this limiting assumption will be discussed later.

$$\chi_{\text{surf}} = \chi_{\text{gas}}, \quad (1)$$

where  $\chi_{\text{surf}}$  and  $\chi_{\text{gas}}$  are the mole fractions of tritium in the adsorbed water layers and gas phase, respectively. The assumption of equal mole fractions leads to an equation for the quantity of adsorbed tritium ( $A_{\text{surf}}$ ) on a stainless-steel surface during exposure to tritium gas:

$$A_{\text{surf}} = \lambda * \chi_{\text{gas}} * SA * Q * \frac{2\text{-mol H}}{1\text{-mol H}_2\text{O}}, \quad (2)$$

where  $\lambda$  is the tritium decay constant (Bq), SA is the surface area of the metal ( $m^2$ ), and  $Q$  is the surface concentration of adsorbed water ( $\text{mol H}_2\text{O}/m^2$ ).

Once tritium adsorbs onto the metal surface, it can diffuse into the metal lattice. To determine the flux of tritium across the surface-water layer/metal-lattice interface, the tritium concentrations at the interface are related through the ratio of the tritium solubilities in the two regions.<sup>8</sup>

The final assumption is that negligible quantities of tritium desorb from the surface during the storage period between charging the sample with tritium and each experiment. Little tritium is expected to desorb during this period because the samples were stored under dry helium at 1 atm. Measurements of the residual tritium in the storage vessels show that less than 5% of the activity is lost to the vessel during the storage period. Tritium concentrations redistribute throughout the sample by diffusing from the water layer into the metal lattice to attain an equilibrium state.

## Experimental Setup and Procedures

### 1. Surface Modifications

The surfaces of each sample underwent various pretreatments intended to modify the metal surface. All samples measured  $5.1 \times 1.8 \times 0.3 \text{ cm}^3$ , and their surfaces were machined away to remove manufacturing defects and to expose the metal lattice. The samples were cleaned first with acetone followed by de-ionized water, and finally dried with isopropyl alcohol. Samples receiving no additional treatment are referred to as “as received” or AR. The next modification involved mechanically polishing the AR samples to yield finer surface finishes. Several mechanically polished samples were then electroplated with gold to a thickness of  $1.7 \text{ }\mu\text{m}$ . To bind the gold to the surface, a nickel strike interface was necessary. This interfacial layer had a thickness of  $6 \text{ }\mu\text{m}$ . Another subset of the mechanically polished samples was treated with methods III and IV described by Boulange-Petermann *et al.* for generating hydrophobic and hydrophilic surfaces.<sup>11</sup> In this technique, the samples were washed with 0.5 M of NaOH and then placed in either a 0.2-M or a 4-M nitric-acid bath. Lower acid concentrations are expected to yield more hydrophobic surfaces, while higher acid concentrations should yield hydrophilic surfaces.

The remaining mechanically polished samples were divided into three sets and each set was electropolished for a different duration. The first set (EP2) was electropolished for 10 min while the second set (EP3) was electropolished for 5 min. The third set (EP) was electropolished for an unknown time, as determined by the polisher. The intent of increasing the duration of electropolishing was to extend the surface chromium concentrations deeper into the metal lattice. Increased chromium concentrations are expected to reduce tritium adsorption.<sup>12</sup>

Several samples from the third set of electropolished samples were subjected to one of two treatments intended to enhance either the Fe or the Cr concentrations in the near-surface region.<sup>7</sup> These treatments were intended to test the impact of surface composition on the tritium absorption into stainless steel.

### 2. Surface Analysis

The surface roughness of each finish was measured using a Zygo NewView 100 interferometer or a Zygo NEXView interferometer (Table 147.V). No surface roughness data were available for Batch C oxidation treatments.

The near-surface compositions obtained with x-ray photoelectron spectroscopy (XPS) for select samples are shown in Figs. 147.44 and 147.45. The surfaces of samples treated to enhance either the Fe concentrations (oxidation treatment #1) or the Cr concentrations (oxidation treatment #2) exhibited two distinct regions, each with different Fe and Cr concentrations. In the present study, the average surface concentrations of Fe and Cr were used because the experimental methods represent average tritium interactions with the entire sample’s surface. The near-surface composition for the EP sample shows an increase in the Cr content compared to AR, polished, and the nitric-acid-treated samples. However, the EP process suppressed the Fe content compared to AR and the acid and oxidation treatments. It is also clear that the 0.2- and 4-M acid treatments increased both the Cr and Fe content of the near surface compared to AR, but the increase in Cr between the two acid treatments is nearly identical.

Comparatively, oxidation treatment #2, and the polished samples have a Cr and Fe composition that falls in between the two acid treatments. Therefore, if the surface composition controls tritium absorption, the total quantity of absorbed tritium in polished samples and samples undergoing oxidation treatment #2 should be between the tritium quantities contained within the samples treated with either concentration of nitric acid.

Figures 147.45–147.47 compare the Fe and Cr  $2p_{3/2}$  photoelectron spectra as a function of depth into the metal sample. To collect these data, the surfaces were etched at a rate of 6.7 nm/min and a spectrum collected every 15 s. The resulting collection of spectra for a single sample shows the evolution of the oxidation states of Fe and Cr as a function of depth. In

Table 147.V: Measured surface roughness ( $R_a$ ) for various surface finishes.

Batch A		Batch B		Batch C	
Finish	$R_a$ (nm)	Finish	$R_a$ (nm)	Finish	$R_a$ (nm)
AR1	434	AR2	351	AR3	535
EP2	110	Polish #12	338	Polished	81
EP3	85	Polish #8	316	EP	92
0.2-M HNO <sub>3</sub>	74	Polish #3	46		
4 M	73	Gold	57		

general, the results show a decrease in the oxide concentration and an increase in the elemental composition of each metal with increasing depth. Additionally, each set of spectra indicate that all surfaces (except EP samples and samples that underwent oxidation treatment #1) are dominated by a mix of iron (III) and iron (II) oxides, with a smaller concentration of chromium (III) oxide.

### 3. Sample Loading

All stainless-steel samples were charged with tritium by exposing the samples to a deuterium–tritium (DT) gas mixture at 25°C for 24 h. After exposure, the samples were stored in separate metal containers under a dry helium atmosphere. Three separate batches of samples were charged with tritium using the pressures and tritium purities given in Table 147.VI.

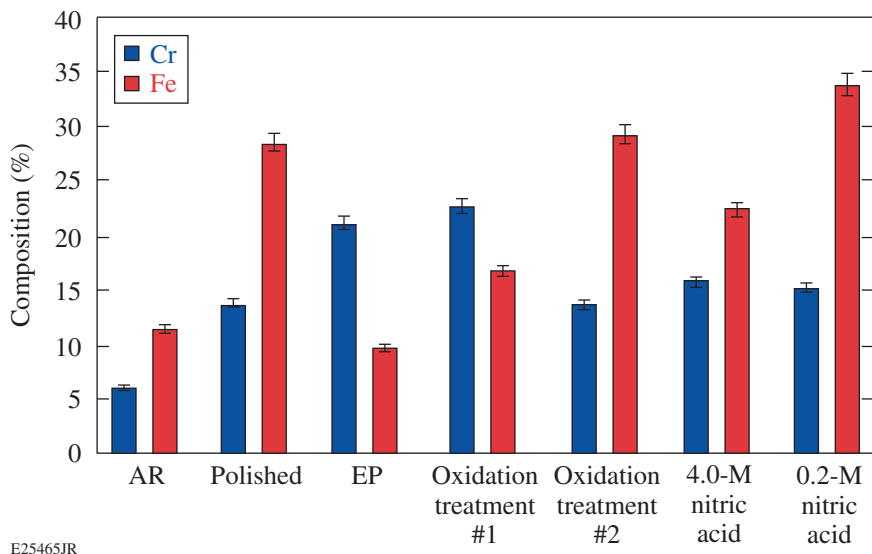


Figure 147.44 Measured Cr and Fe content in select samples using x-ray photoelectron spectroscopy (XPS).

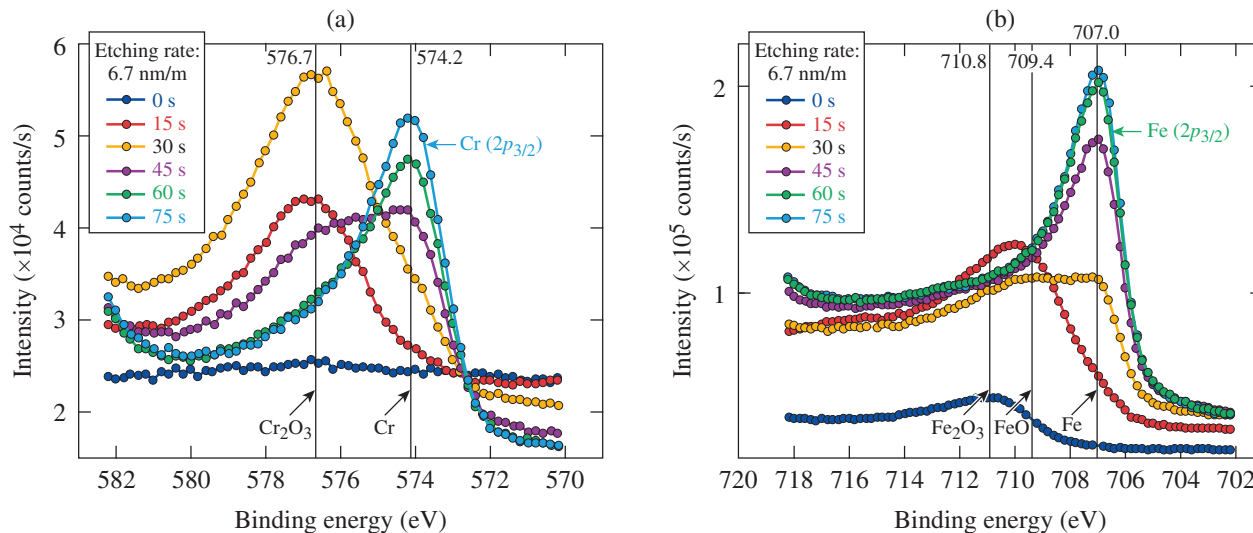


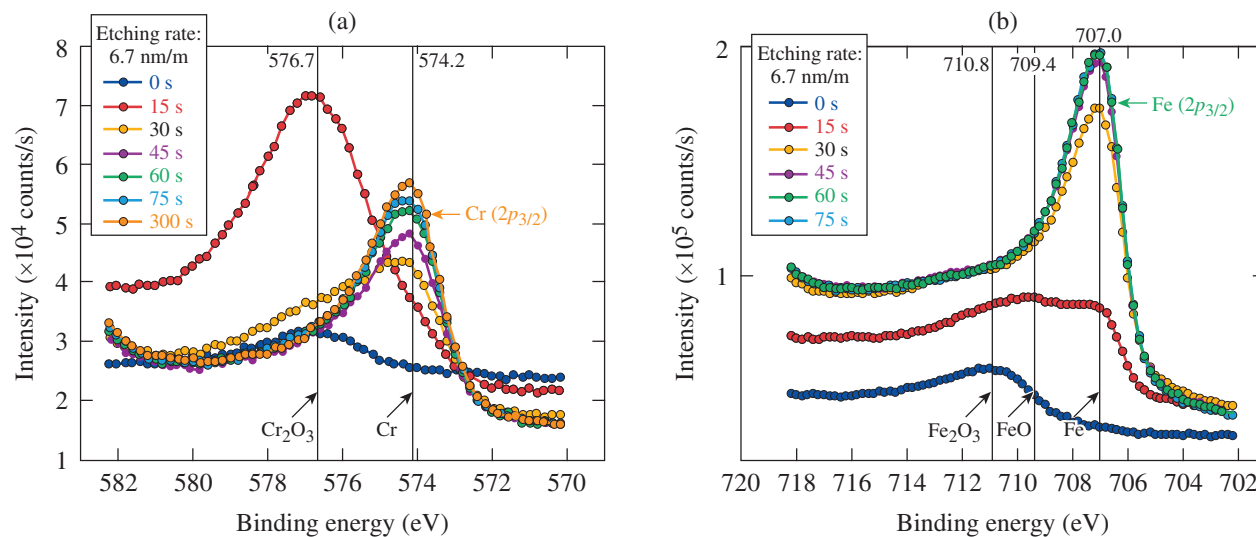
Figure 147.45 XPS photoelectron spectra for (a) Cr and (b) Fe atoms bound to the surface of as-received (AR) samples.

Table 147.VI: Sample loading and storage conditions.

Batch	Pressure (Torr)	Tritium (%)	Storage time (days)
A	550	57	13 to 29
B	530	58	8 to 29
C	550	59	6 to 18

#### 4. Experimental Procedure

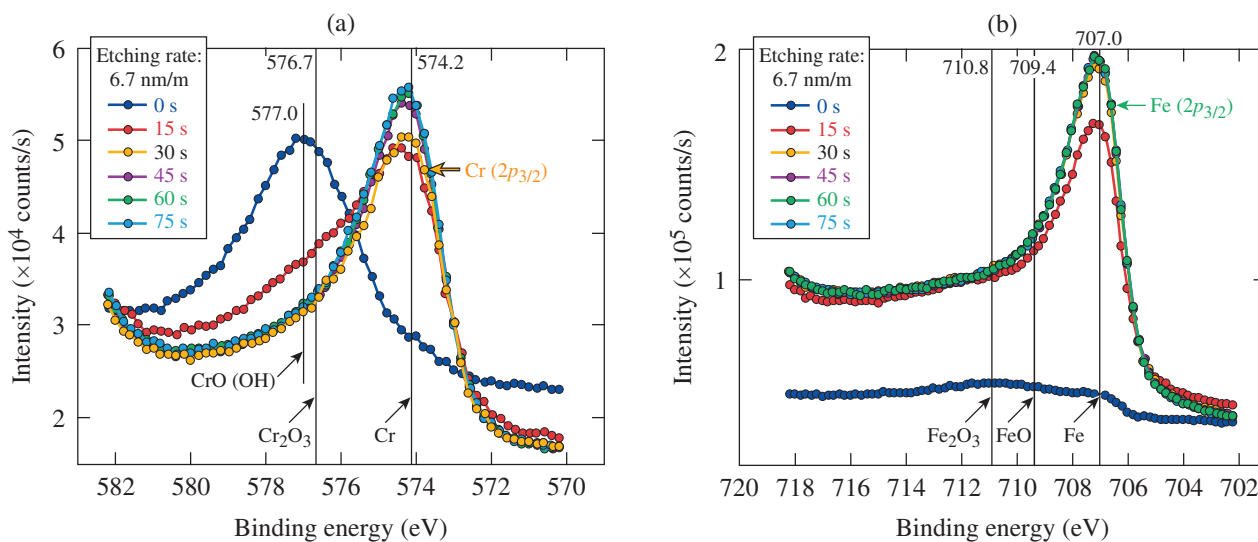
Total tritium inventories were measured with temperature-programmed desorption (TPD) as described in previous work.<sup>9</sup> Tritium migration in the near-surface region was measured with plasma-induced ion sputtering, also described elsewhere.<sup>8</sup>



E25467JR

Figure 147.46

XPS photoelectron spectra for (a) Cr and (b) Fe atoms bound to the surface of samples treated with 4 M of  $\text{HNO}_3$ .



E25468JR

Figure 147.47

XPS photoelectron spectra for (a) Cr and (b) Fe atoms bound to the surface of samples treated with 0.2 M of  $\text{HNO}_3$ .

**Results and Discussion**

The total quantity of tritium removed during thermal desorption experiments shows a strong dependence on the surface composition as illustrated in Figs. 147.48 and 147.49. Each thermal desorption experiment was run at least twice, using separate and fresh samples to verify reproducibility. The AR samples were included to gauge how the various surface modifications influence the total tritium inventory and to provide a reference between the different loading batches. The observed variation in the tritium inventories between the different batches has not been resolved yet, but it is likely a result of subtle changes in the loading, storage, and handling procedures.

The data in Fig. 147.48 demonstrate that, relative to AR1 samples, electropolishing reduces the total quantity of tritium absorbed by the metal. However, increasing the electropolish-

ing duration from 5 to 10 min caused no further reduction in the total tritium inventory.

The data in Fig. 147.48 also demonstrate that the nitric-acid treatments result in significantly higher quantities of tritium absorbed into the samples, as compared with AR1 samples. The higher inventories are evident even though the acid treatment increased the Cr content in the near surface (Fig. 147.44). Contrary to expectations, these results suggest that the increased Cr concentration did not reduce tritium adsorption or absorption.

In general, mechanically polishing a SS surface leads to a reduction in the quantity of absorbed tritium (Fig. 147.50). However, this reduction in total tritium inventory is not exclusively caused by smoother surfaces. For example, polish #12 and polish #8 samples from Batch B in Fig. 147.50 had a surface roughness similar to the AR2 samples but retained half the tritium present on AR2 samples. Additional polishing of both samples in Batch C to reduce the surface roughness about eightfold from ~351 nm to 46 nm did not reduce the absorbed tritium content.

The measured total tritium inventories in gold-plated, SS (Au-SS) samples suggest that the electroplated gold layer does not act as a barrier to tritium absorption. The Au-SS samples contain less tritium than the AR2 samples, but comparable inventories to the polish #3 samples (Fig. 147.50). This suggests that the reduction in absorbed tritium, when comparing Au-SS to AR2 samples, is likely a result of polishing the samples, not electroplating them with gold.

The data provided in Fig. 147.49 again suggest that increasing the near-surface Cr concentration does not alter the absorption of tritium into the substrate. First, the EP samples have

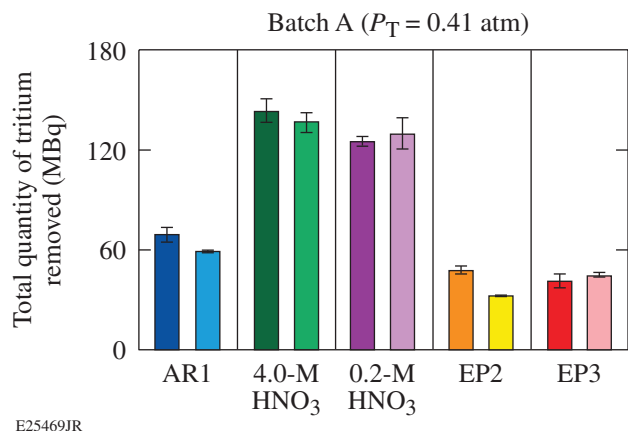


Figure 147.48  
Quantities of tritium removed during thermal desorption experiments using samples loaded with tritium in Batch A.

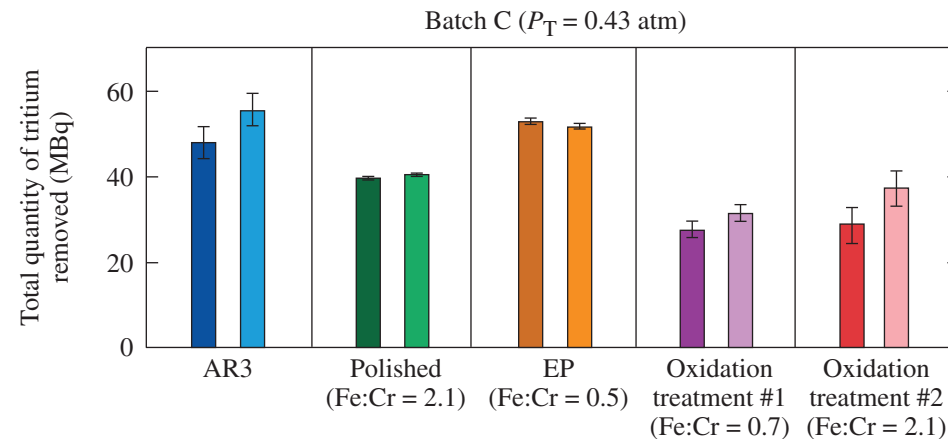


Figure 147.49  
Quantities of tritium removed during thermal desorption using samples from Batch C.

E25471JR

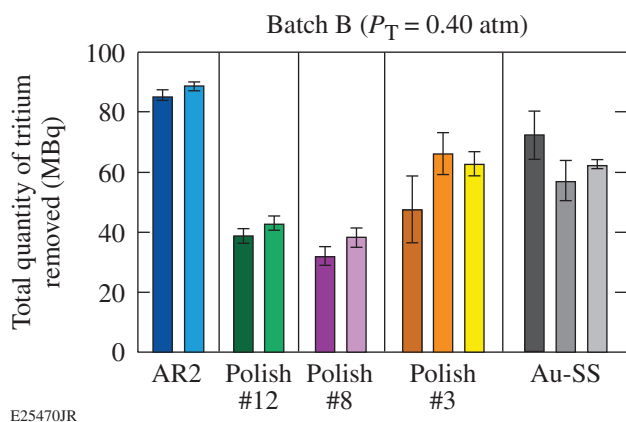


Figure 147.50  
Quantities of tritium removed during thermal desorption experiments using samples loaded with tritium in Batch B.

significantly higher Cr concentrations in the near surface, as compared with the AR samples (Fig. 147.44). However, the EP samples show comparable tritium inventories to the AR3 samples. This is, again, contrary to the expectation that increased Cr concentrations in the near surface lead to lower tritium inventories. Furthermore, samples treated with oxidation treatment #1 showed comparable Cr concentrations to the EP samples (Fig. 147.44), but significantly lower total tritium inventories (Fig. 147.49). Finally, samples treated with oxidation treatment #2 show comparable tritium inventories to oxidation treatment #1, even though the Cr and Fe concentrations are significantly different (Fig. 147.44). These results suggest that the chemical composition of the near surface of stainless steel does not influence the absorption of tritium. It should also be noted that an increase in near-surface Fe concentrations does not account for the observed differences in total inventories. Significantly different tritium inventories were recorded for

samples that underwent the nitric-acid treatments and the oxidation treatment #2. However, the Fe and Cr concentrations were comparable.

The results shown in Fig. 147.48 also confirm that simply polishing SS surfaces reduces the tritium inventory in SS samples. Furthermore, mechanical polishing a surface does not reduce the tritium inventory to the same degree as oxidizing a surface.

The results in Fig. 147.49 show no correlation with surface roughness (0 to 0.54  $\mu\text{m}$ ) to the total activity determined by thermal programmed desorption. Different surface alterations show similar roughness values but drastic variability in the total activity as seen for polish #4 and the nitric-acid treatments. This trend suggests that an increased surface area is not indicative of increased tritium absorption. The data may suggest that the role of the surface area in the absorption of tritium may contribute little compared to the chemical absorption processes.

Using the data shown in Figs. 147.48–147.50, the surface concentration of adsorbed water ( $Q$ ) can be determined using QTRIMM. These concentrations were determined by varying  $Q$  values until the calculated and measured total tritium inventories agreed. Averages of the data shown in Figs. 147.48–147.50 were used in this fitting procedure. The minimization was accomplished using *MATLAB*'s nonlinear least-squares fitting routine. The results of the fits are shown in Table 147.VII for the various surface finishes and loading batches.

The calculated  $Q$  values correspond to submonolayer water coverage of the surface, which is on the lower end of the expected values.<sup>13</sup> These low values are likely a result of the limiting assumption of equal isotopic exchange prob-

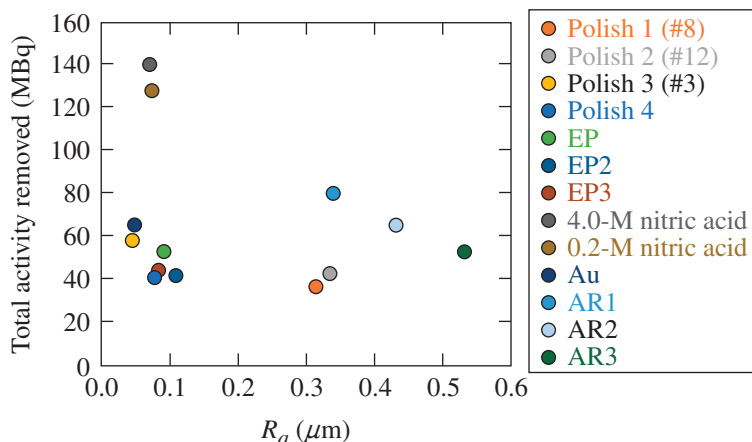


Figure 147.51  
Total activity collected from various samples as a function of surface roughness.

E25472JR

Table 147.VII: Results of fitting thermal and pulsed-plasma data using QTRIMM.  $Q$  values were determined from thermal-desorption data, while the removal efficiencies were determined from pulsed-plasma experiments.

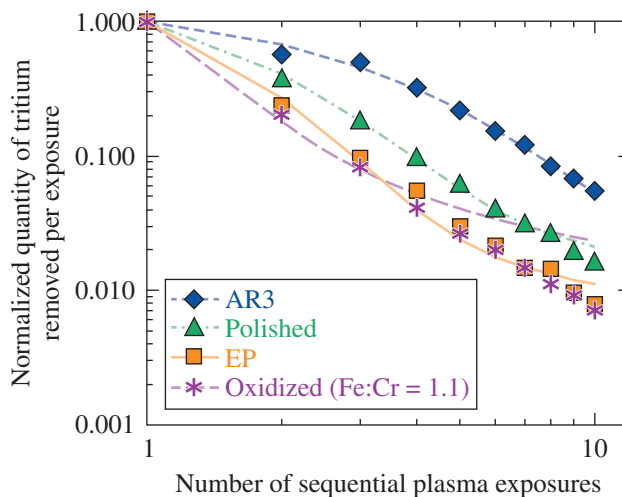
Batch	Metal finish	$Q$ ( $\mu\text{mol}/\text{m}^2$ )	Removal efficiency	$A_{\text{surf}}/A_{\text{total}}$ (%)
A	AR1 (Fe:Cr = 1.8)	22.04	n/a	49
A	4-M HNO <sub>3</sub> (Fe:Cr = 1.3)	55.74	n/a	57
A	0.2-M HNO <sub>3</sub> (Fe:Cr = 2.1)	50.21	n/a	57
A	EP2	11.39	n/a	40
A	EP3	12.66	n/a	42
B	AR2	31.7	0.41	88
B	Polish #12	11.6	0.59	68
B	Polish #8	9.1	0.61	62
B	Polish #3	19.4	0.52	79
C	AR3	15.7	0.34	73
C	Polished	10.7	0.63	65
C	EP (Fe:Cr = 0.5)	16.0	0.75	74
C	Oxidized (Fe:Cr = 0.7)	6.2	0.91	51
C	Oxidized (Fe:Cr = 2.1)	7.7	0.84	56

abilities. Lowering the exchange probability for the formation of double isotope species T<sub>2</sub>O on the metal surface will result in an increase in the calculated quantity of adsorbed water. The derived  $Q$  values indicate that  $\geq 44\%$  of the total tritium inventory is initially located within the adsorbed water layers (Table 147.VII).

The  $Q$  values found from fitting thermal-desorption data agree with data obtained from pulsed-plasma experiments. No plasma data were collected for Batch A. Representative results obtained from samples supporting AR, polished, EP, and Fe-oxidized surfaces from Batch B that were subjected to a pulsed plasma are shown in Fig. 147.52. The data shown have been normalized to the quantity of tritium removed during the first exposure in each respective series to allow for direct comparison of the trends in each data series. These trends indicate that the mechanism for tritium migration to the surface is diffusion from the metal lattice between each plasma exposure.<sup>8</sup>

Figure 147.52 also shows fits to the data using QTRIMM. These fits were calculated by using  $Q$  values obtained from thermal-desorption fits and by varying only the removal efficiency ( $\epsilon$ ) until the data and calculations agreed. To be consistent, only  $Q$  values obtained from QTRIMM fitted to thermal desorption data for samples with the same surface finish and

charged with tritium in the same batch were used to fit pulsed-plasma data. The resulting fits to data show excellent agreement for all data series, except for samples that underwent selective oxidation pretreatments. Removal efficiencies found for each fit are given in Table 147.VII for each surface modification.



E24934aJR

Figure 147.52 Comparison of the results obtained from pulsed-plasma experiments to best fits (calculated using QTRIMM) of various samples charged with tritium in Batch B. The error in each data point is  $\pm 5\%$ .

## Conclusions

The experimental data show that modifying the near surface ( $\leq 40$  nm) of a SS surface by polishing, EP, selective oxidation, or nitric-acid treatments can significantly alter the total quantity of absorbed tritium. These results suggest that a significant fraction of the total tritium inventory initially resides on the surface since as these modifications affect only the near surface of the metal substrate ( $< 10$  nm).

The nitric-acid treatments of the electropolished SS 316 surfaces increased the total tritium inventory by 200% when compared against untreated (AR) samples and 300% compared to EP samples. These results suggest that nitric-acid treatments created more hydrophilic surfaces when compared to untreated (AR) samples.

The differences in the total tritium inventories for the various surface treatments appear to be related to the quantity of water adsorbed on the surface. Increasing or decreasing the water content appears to increase or decrease the total tritium inventory. Figures 147.48 and 147.49 suggest that a 50% reduction in water concentration results in a 35% reduction in total tritium inventory in the electropolished case. On the other hand, increasing the water content by a factor of  $\sim 2.4$  increased the total tritium inventory by 200% in the nitric-acid-treatment case. Measuring the water isotherms is necessary to confirm the calculation results.

The absorption and migration of tritium in each SS sample can be described using QTRIMM. Comparing the output of this model to thermal-desorption data allowed us to determine the surface concentration of adsorbed water. Using this surface concentration, the initial contribution of adsorbed tritium to the total inventory was determined to be  $\geq 44\%$ . Additionally, by using the  $Q$  values derived from fitting thermal-desorption data, we could accurately describe the migration of tritium to the surface for each sample during pulsed-plasma experiments.

## ACKNOWLEDGMENT

This material is based upon work supported by the Department of Energy National Nuclear Security Administration under Award Number DE-NA0001944, the University of Rochester, and the New York State Energy Research and Development Authority. The support of DOE does not constitute an endorsement by DOE of the views expressed in this article.

## REFERENCES

1. R.-D. Penzhorn *et al.*, *J. Nucl. Mater.* **353**, 66 (2006).
2. T. Hirabayashi, M. Saeki, and E. Tachikawa, *J. Nucl. Mater.* **126**, 38 (1984).
3. M. A. Henderson, *Surf. Sci. Rep.* **46**, 1 (2002).
4. T. Ohmi *et al.*, *Rev. Sci. Instrum.* **64**, 2683 (1993).
5. Y. T. Sasaki, *J. Vac. Sci. Technol. A* **25**, 1309 (2007).
6. S.-J. Lee and J.-J. Lai, *J. Mater. Process. Technol.* **140**, 206 (2003).
7. T. Ohmi *et al.*, *J. Electrochem. Soc.* **140**, 1691 (1993).
8. M. Sharpe, W. T. Shmayda, and W. U. Schröder, *Fusion Sci. Technol.* **70**, 97 (2016).
9. M. J. Quinlan, W. T. Shmayda, S. Lim, S. Salnikov, Z. Chambers, E. Pollock, and W. U. Schröder, *Fusion Sci. Technol.* **54**, 519 (2008).
10. J. Crank, *The Mathematics of Diffusion* (Oxford University Press, Oxford, 1979), p. 189.
11. L. Boulange-Petermann, B. Baroux, and M.-N. Bellon-Fontaine, *J. Adhes. Sci. Technol.* **7**, 221 (1993).
12. Y. Ozeki *et al.*, *Fusion Sci. Technol.* **60**, 1499 (2011).
13. M. Nishikawa *et al.*, *J. Nucl. Mater.* **277**, 99 (2000).



---

## Publications and Conference Presentations

---

### Publications

---

- R. Betti, A. R. Christopherson, A. Bose, and K. M. Woo, "Alpha Heating and Burning Plasmas in Inertial Confinement Fusion," *J. Phys.: Conf. Ser.* **717**, 012007 (2016).
- R. Betti and O. A. Hurricane, "Inertial-Confinement Fusion with Lasers," *Nat. Phys.* **12**, 435 (2016).
- T. J. B. Collins, J. A. Marozas, S. Skupsky, D. Cao, P. W. McKenty, J. A. Delettrez, and G. Moses, "Design Options for Polar-Direct-Drive Targets from Alpha Heating to Ignition," *J. Phys.: Conf. Ser.* **717**, 012012 (2016).
- D. H. Crandall, "The Quest for Laboratory Inertial Fusion Burn in the United States," *J. Phys.: Conf. Ser.* **717**, 012001 (2016).
- R. Cristiano, L. Parlato, U. Nasti, M. Ejrnaes, H. Myoren, T. Taino, R. Sobolewski, and G. P. Pepe, "Superconductor/Ferromagnet Nanowires for Optical Photon Detection," *IEEE Trans. Appl. Supercond.* **26**, 2200104 (2016).
- A. K. Davis, D. Cao, D. T. Michel, M. Hohenberger, D. H. Edgell, R. Epstein, V. N. Goncharov, S. X. Hu, I. V. Igumenshchev, J. A. Marozas, A. V. Maximov, J. F. Myatt, P. B. Radha, S. P. Regan, T. C. Sangster, and D. H. Froula, "Isolating and Quantifying Cross-Beam Energy Transfer in Direct-Drive Implosions on OMEGA and the National Ignition Facility," *Phys. Plasmas* **23**, 056306 (2016) (invited).
- B. Delorme, M. Olazabal-Loumé, A. Casner, Ph. Nicolaï, D. T. Michel, G. Riazuelo, N. Borisenko, J. Breil, S. Fujioka, M. Grech, A. Orekhov, W. Seka, A. Sunahara, D. H. Froula, V. Goncharov, and V. T. Tikhonchuk, "Experimental Demonstration of Laser Imprint Reduction Using Underdense Foams," *Phys. Plasmas* **23**, 042701 (2016).
- W. R. Donaldson, J. Katz, R. Huff, E. M. Hill, J. H. Kelly, J. Kwiatkowski, R. B. Brannon, and R. Boni, "A Picosecond Beam-Timing System for the OMEGA Laser," *Rev. Sci. Instrum.* **87**, 053511 (2016).
- C. Dorrer, A. Consentino, and D. Irwin, "Direct Optical Measurement of the On-Shot Incoherent Focal Spot and Intensity Contrast on the OMEGA EP Laser," *Appl. Phys. B* **122**, 156 (2016).
- R. K. Follett, J. A. Delettrez, D. H. Edgell, V. N. Goncharov, R. J. Henchen, J. Katz, D. T. Michel, J. F. Myatt, J. Shaw, A. A. Solodov, C. Stoeckl, B. Yaakobi, and D. H. Froula, "Two-Plasmon Decay Mitigation in Direct-Drive Inertial-Confinement-Fusion Experiments Using Multilayer Targets," *Phys. Rev. Lett.* **116**, 155002 (2016).
- V. N. Goncharov, S. P. Regan, T. C. Sangster, R. Betti, T. R. Boehly, E. M. Campbell, J. A. Delettrez, D. H. Edgell, R. Epstein, C. J. Forrest, D. H. Froula, V. Yu. Glebov, D. R. Harding, S. X. Hu, I. V. Igumenshchev, F. J. Marshall, R. L. McCrory, D. T. Michel, J. F. Myatt, P. B. Radha, W. Seka, A. Shvydky, C. Stoeckl, W. Theobald, B. Yaakobi, and M. Gatu-Johnson, "Demonstrating Ignition Hydrodynamic Equivalence in Direct-Drive Cryogenic Implosions on OMEGA," *J. Phys.: Conf. Ser.* **717**, 012008 (2016).
- S. X. Hu, L. A. Collins, V. N. Goncharov, J. D. Kress, T. R. Boehly, R. Epstein, R. L. McCrory, and S. Skupsky, "First-Principles Studies on the Equation of State, Thermal Conductivity, and Opacity of Deuterium-Tritium (DT) and Polystyrene (CH) for Inertial Confinement Fusion Applications," *J. Phys.: Conf. Ser.* **717**, 012064 (2016).
- S. X. Hu, L. A. Collins, V. N. Goncharov, J. D. Kress, R. L. McCrory, and S. Skupsky, "First-Principles Investigations on Ionization and Thermal Conductivity of Polystyrene for Inertial Confinement Fusion Applications," *Phys. Plasmas* **23**, 042704 (2016).
- I. V. Igumenshchev, V. N. Goncharov, F. J. Marshall, J. P. Knauer, E. M. Campbell, C. J. Forrest, D. H. Froula, V. Yu. Glebov, R. L. McCrory, S. P. Regan, T. C. Sangster, S. Skupsky, and C. Stoeckl, "Three-Dimensional Modeling of Direct-Drive Cryogenic Implosions on OMEGA," *Phys. Plasmas* **23**, 052702 (2016).

J. D. Kilkenny, J. A. Caggiano, R. Hatarik, J. P. Knauer, D. B. Sayre, B. K. Spears, S. V. Weber, C. B. Yeaman, C. J. Cerjan, L. Divol, M. J. Eckart, V. Yu. Glebov, H. W. Herrmann, S. Le Pape, D. H. Munro, G. P. Grim, O. S. Jones, L. Berzak-Hopkins, M. Gatu-Johnson, A. J. Mackinnon, N. B. Meezan, D. T. Casey, J. A. Frenje, J. M. Mcnane, R. Petrasso, H. Rinderknecht, W. Stoeffl, and A. B. Zylstra, "Understanding the Stagnation and Burn of Implosions on NIF," *J. Phys.: Conf. Ser.* **688**, 012048 (2016).

Y. Kim, H. W. Herrmann, N. M. Hoffman, M. J. Schmitt, P. A. Bradley, S. Gales, C. J. Horsfield, M. Rubery, A. Leatherland, M. Gatu Johnson, J. A. Frenje, and V. Yu. Glebov, "Direct-Drive DT Implosions with Knudsen Number Variations," *J. Phys.: Conf. Ser.* **717**, 012030 (2016).

T. Z. Kosc, J. H. Kelly, E. M. Hill, and L. J. Waxer, "Design and Operation of the Multiple-Pulse Driver Line on the OMEGA Laser," *J. Phys.: Conf. Ser.* **717**, 012104 (2016).

J. A. Marozas, T. J. B. Collins, J. D. Zuegel, P. W. McKenty, D. Cao, S. Fochs, and P. B. Radha, "Continuous Distributed Phase-Plate Advances for High-Energy Laser Systems," *J. Phys.: Conf. Ser.* **717**, 012107 (2016).

C. A. McCoy, M. C. Gregor, D. N. Polsin, D. E. Fratanduono, P. M. Celliers, T. R. Boehly, and D. D. Meyerhofer, "Shock-Wave Equation-of-State Measurements in Fused Silica Up to 1600 GPa," *J. Appl. Phys.* **119**, 215901 (2016).

J. F. Myatt, J. Shaw, V. N. Goncharov, J. Zhang, A. V. Maximov, R. W. Short, R. K. Follett, W. Seka, D. H. Edgell, and D. H. Froula, "Laser-Plasma Interaction in Direct-Drive Inertial Confinement Fusion," *J. Phys.: Conf. Ser.* **717**, 012040 (2016).

J. B. Oliver, C. Smith, J. Spaulding, A. L. Rigatti, B. Charles, S. Papernov, B. Taylor, J. Foster, C. W. Carr, R. Luthi, B. Hollingsworth, and D. Cross, "Glancing-Angle-Deposited Magnesium Oxide Films for High-Fluence Applications," *Opt. Mater. Express* **6**, 2291 (2016).

B. W. Plansinis, W. R. Donaldson, and G. P. Agrawal, "Temporal Waveguides for Optical Pulses," *J. Opt. Soc. Am. B* **33**, 1112 (2016).

P. B. Radha, V. N. Goncharov, M. Hohenberger, T. C. Sangster, R. Betti, R. S. Craxton, D. H. Edgell, R. Epstein, D. H. Froula, J. A. Marozas, F. J. Marshall, R. L. McCrory, P. W. McKenty,

D. D. Meyerhofer, D. T. Michel, S. X. Hu, W. Seka, A. Shvydky, S. Skupsky, J. A. Frenje, M. Gatu-Johnson, R. D. Petrasso, T. Ma, S. Le Pape, and A. J. Mackinnon, "Direct-Drive Implosion Physics: Results from OMEGA and the National Ignition Facility," *J. Phys.: Conf. Ser.* **688**, 012006 (2016).

P. B. Radha, M. Hohenberger, D. H. Edgell, J. A. Marozas, F. J. Marshall, D. T. Michel, M. J. Rosenberg, W. Seka, A. Shvydky, T. R. Boehly, T. J. B. Collins, E. M. Campbell, R. S. Craxton, J. A. Delettrez, S. N. Dixit, J. A. Frenje, D. H. Froula, V. N. Goncharov, S. X. Hu, J. P. Knauer, R. L. McCrory, P. W. McKenty, D. D. Meyerhofer, J. Moody, J. F. Myatt, R. D. Petrasso, S. P. Regan, T. C. Sangster, H. Sio, S. Skupsky, and A. Zylstra, "Direct Drive: Simulations and Results from the National Ignition Facility," *Phys. Plasmas* **23**, 056305 (2016) (invited).

P. B. Radha, M. Hohenberger, F. J. Marshall, D. T. Michel, J. Bates, T. R. Boehly, T. J. B. Collins, R. S. Craxton, J. A. Delettrez, S. N. Dixit, D. H. Edgell, J. A. Frenje, D. H. Froula, V. N. Goncharov, S. X. Hu, M. Karasik, J. P. Knauer, S. LePape, J. A. Marozas, R. L. McCrory, P. W. McKenty, D. D. Meyerhofer, J. F. Myatt, S. Obenschein, R. D. Petrasso, S. P. Regan, M. J. Rosenberg, T. C. Sangster, W. Seka, A. Shvydky, H. Sio, S. Skupsky, and A. Zylstra, "Polar-Direct-Drive Experiments at the National Ignition Facility," *J. Phys.: Conf. Ser.* **717**, 012009 (2016).

M. Rutkauskas, C. Farrell, C. Dorrer, K. L. Marshall, T. Crawford, T. R. Lundquist, P. Vedagarbha, K. Erington, D. Bodoh, and D. T. Reid, "Two-Photon Laser-Assisted Device Alteration in CMOS Integrated Circuits Using Linearly, Circularly and Radially Polarized Light," *Microelectronics Reliability* **60**, 62 (2016).

A. A. Solodov, M. J. Rosenberg, J. F. Myatt, R. Epstein, S. P. Regan, W. Seka, J. Shaw, M. Hohenberger, J. W. Bates, J. D. Moody, J. E. Ralph, D. P. Turnbull, and M. A. Barrios, "Hydrodynamic Simulations of Long-Scale-Length Plasmas for Two-Plasmon-Decay Planar-Target Experiments on the NIF," *J. Phys.: Conf. Ser.* **717**, 012053 (2016).

C. Stoeckl, R. Boni, F. Ehrne, C. J. Forrest, V. Yu. Glebov, J. Katz, D. J. Lonobile, J. Magoon, S. P. Regan, M. J. Shoup III, A. Sorce, C. Sorce, T. C. Sangster, and D. Weiner, "Neutron Temporal Diagnostic for High-Yield Deuterium-Tritium Cryogenic Implosions on OMEGA," *Rev. Sci. Instrum.* **87**, 053501 (2016).

---

**Forthcoming Publications**


---

A. Bose, K. M. Woo, R. Betti, E. M. Campbell, D. Mangino, A. R. Christopherson, R. L. McCrory, R. Nora, S. P. Regan, V. N. Goncharov, T. C. Sangster, C. J. Forrest, J. Frenje, M. Gatu Johnson, V. Yu. Glebov, J. P. Knauer, F. J. Marshall, C. Stoeckl, and W. Theobald, "Core Conditions for Alpha Heating Attained in Direct-Drive Inertial Confinement Fusion," to be published in *Physical Review E*.

B. P. Chock, T. B. Jones, and D. R. Harding, "Effect of a Surfactant on the Electric-Field Assembly of Oil/Water Emulsions for Making Foam Targets," to be published in *Fusion Science and Technology*.

W. R. Donaldson, J. Katz, T. Z. Kosc, J. H. Kelly, E. M. Hill, and R. E. Bahr, "Enhancements to the Timing of the OMEGA Laser System to Improve Illumination Uniformity," to be published in *Nanoscience & Engineering (Proc. SPIE)*.

R. Epstein, S. P. Regan, B. A. Hammel, L. J. Suter, H. A. Scott, M. A. Barrios, D. K. Bradley, D. A. Callahan, C. Cerjan, G. W. Collins, S. N. Dixit, T. Döppner, M. J. Edwards, D. R. Farley, K. B. Fournier, S. Glenn, S. H. Glenzer, I. E. Golovkin, A. Hamza, D. G. Hicks, N. Izumi, O. S. Jones, M. H. Key, J. D. Kilkenny, J. L. Kline, G. A. Kyrala, O. L. Landen, T. Ma, J. J. MacFarlane, A. J. Mackinnon, R. C. Mancini, R. L. McCrory, D. D. Meyerhofer, N. B. Meezan, A. Nikroo, H.-S. Park, P. K. Patel, J. E. Ralph, B. A. Remington, T. C. Sangster, V. A. Smalyuk, P. T. Springer, R. P. J. Town, and J. L. Tucker, "Applications and Results of X-Ray Spectroscopy in Implosion Experiments on the National Ignition Facility," to be published in *Proceedings of Atomic Processes in Plasmas (invited)*.

R. K. Follett, J. A. Delettrez, D. H. Edgell, R. J. Henchen, J. Katz, J. F. Myatt, and D. H. Froula, "Plasma Characterization Using Ultraviolet Thomson Scattering from Ion-Acoustic and Electron Plasma Waves" to be published in *Review of Scientific Instruments (invited)*.

D. R. Harding, D. C. Whitaker, and C. Fella, "Growth of a Solid DT Crystal from the Liquid Inside Inertial Confinement Fusion Targets," to be published in *Fusion Science and Technology*.

O. A. Hurricane, D. A. Callahan, D. T. Casey, E. L. Dewald, T. R. Dittrich, T. Döppner, S. Haan, D. E. Hinkel, L. F. Berzak Hopkins, O. Jones, A. L. Kritcher, S. Le Pape, T. Ma, A. G.

MacPhee, J. L. Milovich, J. Moody, A. Pak, H.-S. Park, P. K. Patel, J. E. Ralph, H. F. Robey, J. S. Ross, J. D. Salmonson, B. K. Spears, P. T. Springer, R. Tommasini, F. Albert, L. R. Benedetti, R. Bionta, E. Bond, D. K. Bradley, J. Caggiano, P. M. Celliers, C. Cerjan, J. A. Church, R. Dylla-Spears, D. Edgell, M. J. Edwards, D. Fittinghoff, M. A. Barrios Garcia, A. Hamza, R. Hatarik, H. Herrmann, M. Hohenberger, D. Hoover, J. L. Kline, G. Kyrala, B. Koziolowski, G. Grim J. E. Field, J. Frenje, N. Izumi, M. Gatu Johnson, S. F. Khan, J. Knauer, T. Kohut, O. Landen, F. Merrill, P. Michel, A. Moore, S. R. Nagel, A. Nikroo, T. Parham, R. R. Rygg, D. Sayre, M. Schneider, D. Shaughnessy, D. Strozzi, R. P. J. Town, D. Turnbull, P. Volegov, A. Wan, K. Widmann, C. Wilde, and C. Yeaman, "Inertially Confined Fusion Plasmas Dominated by Alpha-Particle Self-Heating," to be published in *Nature Physics*.

A. S. Moore, J. Benstead, M. F. Ahmed, J. Morton, T. M. Guymmer, R. Soufil, T. Pardini, R. L. Hibbard, C. G. Bailey, P. M. Bell, S. Hau-Riege, M. Bedzyk, M. J. Shoup III, S. P. Regan, T. Agliata, R. Jungquist, D. W. Schmidt, L. B. Kot, W. J. Garbett, M. S. Rubery, J. W. Skidmore, E. Gullikson, and F. Salmassi, "Two-Color Spatial and Temporal Temperature Measurements Using a Streaked Soft X-Ray Imager," to be published in *Review of Scientific Instruments*.

S. Papernov, A. A. Kozlov, J. B. Oliver, C. Smith, L. Jensen, S. Günster, H. Mädebach, and D. Ristau, "Role of  $\text{HfO}_2/\text{SiO}_2$  Thin-Film Interfaces in Near-Ultraviolet Absorption and Pulsed Laser Damage," to be published in *Optical Engineering*.

S. P. Regan, V. N. Goncharov, I. V. Igumenshchev, T. C. Sangster, R. Betti, A. Bose, T. R. Boehly, M. J. Bonino, E. M. Campbell, D. Cao, T. J. B. Collins, R. S. Craxton, A. K. Davis, J. A. Delettrez, D. H. Edgell, R. Epstein, C. J. Forrest, J. A. Frenje, D. H. Froula, M. Gatu Johnson, V. Yu. Glebov, D. R. Harding, M. Hohenberger, S. X. Hu, D. Jacobs-Perkins, R. Janezic, M. Karasik, R. L. Keck, J. H. Kelly, T. J. Kessler, J. P. Knauer, T. Z. Kosc, S. J. Loucks, J. A. Marozas, F. J. Marshall, R. L. McCrory, P. W. McKenty, D. D. Meyerhofer, D. T. Michel, J. F. Myatt, S. P. Obenshain, R. D. Petrasso, P. B. Radha, B. Rice, M. J. Rosenberg, A. J. Schmitt, M. J. Schmitt, W. Seka, W. T. Shmayda, M. J. Shoup III, A. Shvydky, S. Skupsky, A. A. Solodov, C. Stoeckl, W. Theobald, J. Ulreich, M. D. Wittman, K. M.

Woo, B. Yaakobi, and J. D. Zuegel, "Demonstration of Fuel Hot-Spot Pressure in Excess of 50 Gbar for Direct-Drive, Layered Deuterium-Tritium Implosions on OMEGA," to be published in *Physical Review Letters*.

M. Sharpe, W. T. Shmayda, and W. U. Schröder, "Tritium Migration to the Surfaces of Stainless-Steel 316, Aluminum 6061, and Oxygen-Free, High-Conductivity Copper," to be published in *Fusion Science and Technology*.

W. T. Shmayda, M. D. Wittman, R. F. Earley, J. L. Reid, and N. P. Redden, "The Laboratory for Laser Energetics' Hydrogen Isotope Separation System," to be published in *Fusion Engineering and Design* (invited).

N. D. Viza, M. H. Romanofsky, M. J. Moynihan, and D. R. Harding, "The Effect of a Surfactant on the Operation of T-Junctions for Mass-Producing Foam Targets," to be published in *Fusion Science and Technology*.

## Conference Presentations

M. J. Rosenberg, V. Yu. Glebov, C. Stoeckl, W. Seka, F. J. Marshall, J. A. Delettretz, P. W. McKenty, M. Hohenberger, R. Betti, V. N. Goncharov, P. B. Radha, J. P. Knauer, T. C. Sangster, H. G. Rinderknecht, F. H. Séguin, A. B. Zylstra, J. A. Frenje, H. Sio, M. Gatu Johnson, C. K. Li, R. D. Petrasso, N. M. Hoffman, G. Kagan, H. W. Herrmann, R. E. Olson, P. A. Amendt, S. Le Pape, T. Ma, A. J. Mackinnon, J. R. Rygg, S. C. Wilks, L. Berzak Hopkins, D. T. Casey, O. L. Landen, J. D. Lindl, J. Pino, H. F. Robey, S. Atzeni, O. Larroche, and A. Nikroo, "Ion Kinetic Effects in Exploding-Pusher Implosions on OMEGA and the National Ignition Facility," ICF Kinetic Physics Workshop, Livermore, CA, 5–7 April 2016.

The following presentations were made at the 11th International Conference on Tritium Science and Technology, Charleston, SC, 17–22 April 2016:

C. Fagan, M. Sharpe, W. T. Shmayda, and W. U. Schröder, "The Impact of Hydrophobicity of Stainless-Steel Surfaces on Tritium Inventories."

M. Sharpe, C. Fagan, W. T. Shmayda, and W. U. Schröder, "Influence of Surface Modifications on the Adsorption and Absorption of Tritium into 316 Stainless Steel."

W. T. Shmayda, M. D. Wittman, J. L. Reid, and R. F. Earley, "Tritium Activities at the University of Rochester's Laboratory for Laser Energetics."

M. D. Wittman, W. T. Shmayda, J. L. Reid, N. Redden, R. F. Earley, J. Magoon, K. Heung, S. Xiao, T. Sessions, and S. Redd,

"Isotope Separation System at the University of Rochester's Laboratory for Laser Energetics."

The following presentations were made at the 12th Direct Drive and Fast Ignition Workshop, Talence, France, 25–27 April 2016:

R. Betti, A. Bose, K. M. Woo, E. M. Campbell, A. R. Christopherson, R. L. McCrory, and R. Nora, "Fusion-Yield Extrapolation to Higher Laser Energies for Direct-Drive Inertial Fusion Including the Effect of Alpha Heating."

V. N. Goncharov, S. P. Regan, T. C. Sangster, R. Betti, T. R. Boehly, M. J. Bonino, E. M. Campbell, T. J. B. Collins, R. S. Craxton, A. K. Davis, J. A. Delettretz, D. H. Edgell, R. Epstein, C. J. Forrest, D. H. Froula, V. Yu. Glebov, D. R. Harding, S. X. Hu, I. V. Igumenshchev, R. T. Janezic, J. H. Kelly, T. J. Kessler, T. Z. Kosc, S. J. Loucks, J. A. Marozas, F. J. Marshall, R. L. McCrory, P. W. McKenty, D. T. Michel, J. F. Myatt, P. B. Radha, W. Seka, W. T. Shmayda, A. Shvydky, S. Skupsky, C. Stoeckl, W. Theobald, F. Weilacher, B. Yaakobi, D. D. Meyerhofer, J. A. Frenje, M. Gatu Johnson, R. D. Petrasso, S. P. Obenshain, and M. Karasik, "Status of Direct-Drive Research in the U.S."

I. V. Igumenshchev, V. N. Goncharov, F. J. Marshall, J. P. Knauer, E. M. Campbell, C. J. Forrest, D. H. Froula, V. Yu. Glebov, R. L. McCrory, T. C. Sangster, S. Skupsky, and C. Stoeckl, "Three-Dimensional Modeling of Direct-Drive Cryogenic Implosions on OMEGA."

P. B. Radha, "Direct Drive at the National Ignition Facility."

S. P. Regan, V. N. Goncharov, T. C. Sangster, R. Betti, T. R. Boehly, M. J. Bonino, E. M. Campbell, D. Cao, T. J. B. Collins, R. S. Craxton, A. K. Davis, J. A. Delettrez, D. H. Edgell, R. Epstein, C. J. Forrest, D. H. Froula, V. Yu. Glebov, D. R. Harding, M. Hohenberger, S. X. Hu, I. V. Igumenshchev, R. T. Janezic, J. H. Kelly, T. J. Kessler, J. P. Knauer, T. Z. Kosc, J. A. Marozas, F. J. Marshall, R. L. McCrory, P. W. McKenty, D. T. Michel, J. F. Myatt, P. B. Radha, M. J. Rosenberg, W. Seka, W. T. Shmayda, A. Shvydky, S. Skupsky, A. A. Solodov, C. Stoeckl, W. Theobald, M. D. Wittman, B. Yaakobi, J. D. Zuegel, J. A. Frenje, M. Gatu Johnson, R. D. Petrasso, S. P. Obenschain, M. Karasik, A. J. Schmitt, D. D. Meyerhofer, and M. J. Schmitt, “Demonstration of 50-Gbar Hot-Spot Pressure and Reduction of Cross-Beam Energy Transfer for Direct-Drive, Layered Deuterium–Tritium Implosions on OMEGA.”

W. Theobald, R. Betti, W. Seka, A. Bose, K. S. Anderson, M. Hohenberger, F. J. Marshall, D. T. Michel, A. Shvydky, A. A. Solodov, C. Stoeckl, D. H. Edgell, B. Yaakobi, R. Nora, A. Casner, M. Lafon, C. Reverdin, X. Ribeyre, E. Llor-aisa, A. Vallet, J. Peebles, F. N. Beg, and M. S. Wei, “Gigabar Shocks for Direct-Drive Shock-Ignition Fusion.”

The following presentations were made at the Omega Laser Facility Users Group Workshop, Rochester, NY, 27–29 April 2016:

W. J. Armstrong, J. C. Puth, and R. Rombaut, “Target Diagnostic Timing Manager.”

J. R. Davies, D. H. Barnak, R. Betti, E. M. Campbell, P.-Y. Chang, G. Fiksel, J. P. Knauer, S. P. Regan, A. Harvey-Thompson, K. J. Peterson, A. B. Sefkow, D. B. Sinars, and S. A. Slutz, “An Overview of Laser-Driven Magnetized Liner Inertial Fusion on OMEGA.”

M. J. Guardalben, M. Spilatro, L. J. Waxer, and M. Barcysz, “OMEGA EP UV Prediction Model for Enhanced Operational Performance.”

E. M. Hill, G. Balonek, R. Cuffney, J. H. Kelly, and T. Z. Kosc, “OMEGA SSD Arbitrary Waveform Generation Installation and Activation.”

E. M. Hill and J. C. Puth, “Omega Laser Facility and Diagnostic Timing Management.”

S. Ivancic, D. Haberberger, P. Angland, M. Barcysz, M. Bedzyk, R. Boni, R. Brown, R. S. Craxton, A. Davies, F. Ehrne, R. K. Jungquist, J. C. Puth, R. G. Roides, W. Seka, M. J. Shoup III, C. Stoeckl, W. Theobald, D. Weiner, and D. H. Froula, “Optical Diagnostic Suite (Schlieren, Interferometry, and Angular Filter Refractometry) on OMEGA EP Using a 10-ps, 263-nm Probe Beam.”

R. Jungquist, “Short-Pulse Stray Light Management.”

R. W. Kidder, A. Zeller, M. Charissis, P. Stoeckl, J. J. Rung, and R. Holderried, “The Principal Investigator Portal Provides a Gateway to Shot Information for External Users.”

R. W. Kidder, A. Zeller, T. Meyer, P. Stoeckl, R. Pasols, and R. Holderried, “External User Access Through the LLE Principal Investigator Portal.”

J. Kwiatkowski, M. Barcysz, M. Bedzyk, A. Kalb, B. E. Kruschwitz, C. McMahon, T. Nguyen, A. L. Rigatti, and M. Sacchitella, “OMEGA EP Short-Pulse Ratiometer.”

J. Kwiatkowski, E. M. Hill, B. Ehrich, M. Heimbueger, F. J. Marshall, and B. E. Kruschwitz, “OMEGA EP Pointing, Focusing, and Timing.”

J. Kwiatkowski, S. J. Stagnitto, S. F. B. Morse, M. Labuzeta, and V. Guiliano, “Characterizing Debris-Shield Transmission Degradation and Estimating On-Target Energy.”

D. Mastro Simone, A. Agliata, T. Buczek, D. J. Lonobile, M. J. Shoup III, and C. Sorce, “Enhanced Gas-Filled Capabilities for Ten-Inch-Manipulator-Based Target Positioners.”

D. Mastro Simone, G. Fiksel, J. Magoon, A. Agliata, P.-Y. Chang, and D. H. Barnak, “Fielding MIFEDS on OMEGA.”

S. F. B. Morse, “Omega Facility OLUG 2016 Update: Progress on Recommendations and Items of General Interest.”

P. M. Nilson, F. Ehrne, C. Mileham, D. Mastro Simone, R. K. Jungquist, C. Taylor, R. Boni, J. Hassett, D. J. Lonobile, R. W. Kidder, M. J. Shoup III, A. A. Solodov, C. Stoeckl, and D. H. Froula, “High-Resolving Power, Ultrafast Streaked X-Ray Spectroscopy on OMEGA EP.”

T. C. Sangster, K. S. Anderson, R. Betti, T. R. Boehly, B. Boni, M. J. Bonino, E. M. Campbell, D. Canning, D. Cao, T. J. B.

Collins, R. S. Craxton, A. K. Davis, J. A. Delettrez, W. R. Donaldson, D. H. Edgell, R. Epstein, C. J. Forrest, D. H. Froula, V. Yu. Glebov, D. R. Harding, M. Hohenberger, S. X. Hu, H. Huang, I. V. Igumenshchev, R. T. Janezic, D. W. Jacobs-Perkins, J. Katz, R. L. Keck, J. H. Kelly, T. J. Kessler, B. E. Krushwitz, J. P. Knauer, T. Z. Kosc, S. J. Loucks, J. A. Marozas, F. J. Marshall, A. V. Maximov, R. L. McCrory, P. W. McKenty, D. T. Michel, S. F. B. Morse, J. F. Myatt, P. M. Nilson, J. C. Puth, P. B. Radha, B. S. Rice, M. J. Rosenberg, W. Seka, W. T. Shmayda, R. W. Short, A. Shvydky, M. J. Shoup III, S. Skupsky, A. A. Solodov, C. Sorce, S. Stagnitto, C. Stoeckl, W. Theobald, J. Ulreich, M. D. Wittman, B. Yaakobi, J. D. Zuegel, J. A. Frenje, M. Gatu Johnson, R. D. Petrasso, H. Sio, B. Lahmann, M. A. Barrios, P. Bell, D. K. Bradley, D. A. Callahan, A. Carpenter, D. T. Casey, J. Celeste, M. Dayton, S. N. Dixit, C. Goyon, O. A. Hurricane, S. Le Pape, L. Masse, P. Michel, J. D. Moody, S. R. Nagel, A. Nikroo, R. Nora, L. Pickworth, J. E. Ralph, H. G. Rinderknecht, R. P. J. Town, D. P. Turnbull, R. J. Wallace, P. J. Wegner, M. Farrell, A. Greenwood, T. Hilsabeck, J. D. Kilkenny, N. Rice, M. Schoff, N. Petta, J. Hund, S. P. Obenschain, J. W. Bates, M. Karasik, A. J. Schmitt, J. Weaver, M. J. Schmitt, G. Rochau, J. Porter, M. Sanchez, L. Claus, G. Robertson, O. Looker, J. Hares, and T. Dymoke-Bradshaw, “Direct Drive 2020.”

I. Seth and J. P. Knauer, “Analysis of Chemical Vapor Deposition Diamonds for Neutron Detection on OMEGA.”

S. Stagnitto, M. Labuzeta, and C. Sorce, “Qualifying as an External Instrument Specialist/Technician at LLE.”

X. K. Zhou and S. X. Hu, “Radiation Reaction of Electrons at Laser Intensities up to  $10^{25}$  W/cm<sup>2</sup>.”

---

N. D. Viza, M. Wang, M. H. Romanofsky, and D. R. Harding, “Using Lab-on-Chip Technology to Mass Produce Inertial Fusion Energy Targets,” Exploring Alternative Energy: CO<sub>2</sub> as a Resource, Rochester, NY, 29 April 2016.

---

The following presentations were made at the 46th Annual Anomalous Absorption Conference, Old Saybrook, CT, 1–6 May 2016:

D. H. Barnak, R. Betti, E. M. Campbell, P.-Y. Chang, J. R. Davies, G. Fiksel, J. P. Knauer, S. P. Regan, A. Harvey-Thompson,

K. J. Peterson, A. B. Sefkow, D. B. Sinars, and S. A. Slutz, “Scaling Laser-Driven Magnetized Liner Inertial Fusion to the National Ignition Facility.”

E. Borwick, S. X. Hu, J. Li, R. Yan, and C. Ren, “Full-Pulse Particle-in-Cell Simulations of Hot-Electron Generation in OMEGA Experiments.”

S. Bucht, D. Haberberger, J. Bromage, and D. H. Froula, “Transforming the Idler for Use in Laser–Plasma Interaction Experiments.”

E. M. Campbell, “The National Ignition Facility: An Unexpected Journey, Lessons to be Learned to Secure Projects of Scale, and Perspectives on the Future of Inertial Confinement Fusion Research.”

A. Davies, J. Katz, S. Bucht, D. Haberberger, J. Bromage, J. D. Zuegel, D. H. Froula, J. Sadler, P. A. Norreys, R. Bingham, R. Trines, and L. O. Silva, “Thomson Scattering from Non-linear Electron Plasma Waves.”

J. R. Davies, D. H. Barnak, R. Betti, P.-Y. Chang, K. J. Peterson, A. B. Sefkow, D. B. Sinars, and S. A. Slutz, “An Overview of Laser-Driven Magnetized Linear Inertial Fusion on OMEGA.”

A. K. Davis, D. T. Michel, S. X. Hu, R. Epstein, J. P. Knauer, and D. H. Froula, “Conduction-Zone Measurements Using X-Ray Self-Emission Images.”

D. H. Edgell, R. K. Follett, J. Katz, J. F. Myatt, W. Seka, and D. H. Froula, “Polarization Dependence of Cross-Beam Energy Transfer in Unabsorbed Light Beamlets.”

D. H. Froula, R. K. Follett, R. J. Henchen, V. N. Goncharov, A. A. Solodov, J. A. Delettrez, D. H. Edgell, B. Yaakobi, C. Stoeckl, and J. F. Myatt, “The Effect of Cross-Beam Energy Transfer on Two-Plasmon Decay in Direct-Drive Implosions.”

D. Haberberger, D. H. Froula, A. Pak, A. Link, P. K. Patel, F. Fiuza, S. Ya. Tochitsky, and C. Joshi, “Shock-Wave Acceleration of Ions on OMEGA EP.”

R. J. Henchen, S. X. Hu, W. Rozmus, J. Katz, and D. H. Froula, “Heat-Flux Measurements from Collective Thomson-Scattering Spectra.”

J. Li, R. Yan, and C. Ren, “Density Modulation–Induced Absolute Laser–Plasma Instabilities: Simulations and Theory.”

D. T. Michel, S. X. Hu, A. K. Davis, V. Yu. Glebov, V. N. Goncharov, I. V. Igumenshchev, P. B. Radha, C. Stoeckl, and D. H. Froula, "Measurements of the Effect of Adiabatic on the Shell Thickness of Direct-Drive Implosions on OMEGA."

J. F. Myatt, J. G. Shaw, R. K. Follett, D. H. Edgell, V. N. Goncharov, A. V. Maximov, R. W. Short, W. Seka, and D. H. Froula, "A Wave-Based Model for Cross-Beam Energy Transfer in Inhomogeneous Plasmas."

C. Ren, J. Li, W.-D. Liu, and R. Yan, "Simulation of Stimulated Brillouin Scattering and Stimulated Raman Scattering in Shock Ignition."

M. J. Rosenberg, A. A. Solodov, W. Seka, R. Epstein, J. F. Myatt, S. P. Regan, M. Hohenberger, T. J. B. Collins, P. A. Michel, D. P. Turnbull, C. Goyon, J. D. Moody, J. E. Ralph, M. A. Barrios, and J. W. Bates, "Planar Laser-Plasma Interaction Experiments at Direct-Drive Ignition-Relevant Scale Lengths at the National Ignition Facility."

W. Seka, J. F. Myatt, V. N. Goncharov, R. Betti, S. P. Regan, A. V. Maximov, J. A. Delettrez, R. E. Bahr, A. A. Solodov, M. J. Rosenberg, A. Bose, and R. W. Short, "The Influence of Smoothing by Spectral Dispersion on Cross-Beam Energy Transfer."

R. W. Short, W. Seka, and J. F. Myatt, "Kinetic Analysis of Convective Stimulated Raman Scattering and Its Potential as a Temperature Diagnostic."

A. A. Solodov, M. J. Rosenberg, J. F. Myatt, R. Epstein, S. P. Regan, W. Seka, J. G. Shaw, M. Hohenberger, J. W. Bates, P. A. Michel, J. D. Moody, J. E. Ralph, D. P. Turnbull, and M. A. Barrios, "Modeling of Laser-Plasma Interaction Experiments at Direct-Drive Ignition-Relevant Plasma Conditions at the National Ignition Facility."

I. Seth and J. P. Knauer, "Analysis of Chemical-Vapor-Deposition Diamonds for Neutron Detection on OMEGA," Intel International Science and Engineering Fair, Phoenix, AZ, 8–13 May 2016.

G. Chen, A. Koroliov, R. Sherstha, and R. Sobolewski, "Terahertz Spectroscopy of Graphene-Polymer Nanocomposites,"

Frontiers in Materials Science for the 21st Century, Rochester, NY, 16 May 2016.

The following presentations were made at the 21st Topical Conference on High-Temperature Plasma Diagnostics, Madison, WI, 5–9 June 2016:

P. X. Belancourt, W. Theobald, P. A. Keiter, T. J. B. Collins, M. J. Bonino, P. Kozlowski, S. P. Regan, and R. P. Drake, "Demonstration of Imaging X-Ray Thomson Scattering on OMEGA EP."

A. K. Davis, D. T. Michel, R. S. Craxton, R. Epstein, M. Hohenberger, T. Mo, and D. H. Froula, "X-Ray Self-Emission Imaging Used to Diagnose 3-D Nonuniformities in Direct-Drive ICF Implosions."

R. K. Follett, J. A. Delettrez, R. J. Henchen, J. Katz, D. H. Edgell, J. F. Myatt, and D. H. Froula, "Plasma Characterization Using Ultraviolet Thomson Scattering from Ion-Acoustic and Electron Plasma Waves" (invited).

C. J. Forrest, V. Yu. Glebov, V. N. Goncharov, J. P. Knauer, P. B. Radha, S. P. Regan, M. H. Romanofsky, T. C. Sangster, M. J. Shoup III, and C. Stoeckl, "High-Dynamic-Range Neutron Time-of-Flight Detector Used to Infer the  $D(t,n)^4\text{He}$  and  $D(d,n)^3\text{He}$  Reaction Yield and Ion Temperature on OMEGA."

V. Yu. Glebov, R. Flight, C. J. Forrest, J. P. Knauer, S. P. Regan, M. H. Romanofsky, T. C. Sangster, and C. Stoeckl, "A New Microchannel-Plate Neutron Time-of-Flight Detector."

S. T. Ivancic, D. Nelson, P. M. Nilson, C. R. Stillman, C. Mileham, I. A. Begishev, and D. H. Froula, "Design of an Extreme Ultraviolet Spectrometer Suite for Characterization of Rapidly Heated Solid Matter."

J. Katz, R. Boni, A. Maltsev, C. Muir, M. H. Romanofsky, and D. H. Froula, "A Pulse-Front-Tilt-Compensated Streaked Optical Spectrometer with High Throughput and Picosecond Time Resolution."

J. P. Knauer, C. J. Forrest, V. Yu. Glebov, T. C. Sangster, and C. Stoeckl, "Three-Axis Neutron Time-of-Flight Measurement."

P. M. Nilson, F. Ehrne, C. Mileham, D. Mastrosimone, R. K. Jungquist, C. Taylor, C. R. Stillman, S. T. Ivancic, R. Boni,

J. Hassett, D. J. Lonobile, R. W. Kidder, M. J. Shoup III, A. A. Solodov, C. Stoeckl, D. H. Froula, K. W. Hill, L. Gao, M. Bitter, P. Efthimion, and D. D. Meyerhofer, “High-Resolving-Power, Ultrafast Streaked X-Ray Spectroscopy on OMEGA EP” (invited).

C. Sorce, C. Stoeckl, J. Katz, R. Boni, F. Ehrne, C. J. Forrest, V. Yu. Glebov, D. J. Lonobile, S. P. Regan, M. J. Shoup III, A. Sorce, T. C. Sangster, D. Weiner, and J. Magoon, “A Neutron Temporal Diagnostic for High-Yield DT Cryogenic Implosions on OMEGA.”

C. R. Stillman, P. M. Nilson, S. Ivancic, C. Mileham, I. A. Begishev, R. K. Junquist, and D. H. Froula, “A Streaked X-Ray Spectroscopy Platform for Rapidly Heated, Near-Solid Density Plasmas.”

C. Stoeckl, W. Theobald, S. P. Regan, and M. H. Romanofsky, “Calibration of a Time-Resolved Hard X-Ray Detector Using Radioactive Sources.”

W. Theobald, C. Sorce, M. Bedzyk, F. J. Marshall, C. Stoeckl, S. P. Regan, T. Hilsabeck, J. D. Kilkenny, D. Morris, M. Chung, J. Hares, T. Dymoke-Bradshaw, P. Bell, J. Celeste, A. Carpenter, M. Dayton, D. K. Bradley, M. C. Jackson, L. Pickworth, S. Nagel, G. Rochau, J. Porter, M. Sanchez, L. Claus, G. Robertson, and Q. Looker, “Conceptual Design of a Single-Line-of-Sight Time-Resolved X-Ray Imager on OMEGA.”

—————  
The following presentations were made at CLEO 2016, San Jose, CA, 5–10 June 2016:

I. A. Begishev, J. Bromage, P. S. Datte, S. T. Yang, and J. D. Zuegel, “Record Fifth-Harmonic-Generation Efficiency Producing 211-nm Pulses Using Cesium Lithium Borate.”

S. G. Demos, R. Levenson, F. Fereidouni, and Z. Harmany, “Slide-Free (But Not Necessarily Stain-Free) Microscopy via Ultraviolet Excitation.”

C. Dorrer, W. A. Bittle, R. Cuffney, E. M. Hill, T. Z. Kosc, J. H. Kelly, and J. D. Zuegel, “High-Contrast, Time-Multiplexed Pulse-Shaping Systems.”

C. Dorrer, Y. Li, and P. Fiala, “Focal-Spot Optimization by Polarization Modulation.”

C. Dorrer, L. J. Waxer, A. Kalb, E. M. Hill, and J. Bromage, “Single-Shot, High-Resolution Fiber-Based Phase-Diversity Photodetection of Optical Pulses.”

—————  
R. Betti, A. R. Christopherson, A. Bose, K. M. Woo, J. Howard, K. S. Anderson, E. M. Campbell, J. A. Delettrez, V. N. Goncharov, F. J. Marshall, R. L. McCrory, S. P. Regan, T. C. Sangster, C. Stoeckl, W. Theobald, M. J. Edwards, R. Nora, B. K. Spears, and J. Sanz, “Status and Prospects for Burning Plasmas via Laser Fusion,” 43rd IEEE International Conference on Plasma Science, Banff, Alberta, Canada, 19–23 June 2016 (invited).

—————  
The following presentations were made at the 15th Meeting of the Tritium Users Group, Southampton, UK, 21–22 June 2016:

W. T. Shmayda, “Tritium Interaction with Stainless Steel.”

W. T. Shmayda, M. D. Wittman, J. L. Reid, and R. F. Earley, “Tritium Activities at the University of Rochester’s Laboratory for Laser Energetics.”

—————  
C. R. Stillman, P. M. Nilson, S. T. Ivancic, C. Mileham, I. A. Begishev, R. K. Junquist, and D. H. Froula, “A Streaked X-Ray Spectroscopy Platform for Rapidly Heated, Near-Solid Density Plasmas,” 2016 DOE NNSA Stewardship Science Graduate Fellowship Program, Las Vegas, NV, 27–30 June 2016.

—————  
C. J. Forrest, V. Yu. Glebov, J. P. Knauer, P. B. Radha, S. P. Regan, T. C. Sangster, C. Stoeckl, W. U. Schroeder, J. A. Frenje, M. Gatu Johnson, M. W. Paris, G. Hale, and A. B. Zylstra, “Neutron-Induced Break-up Reaction Using Deuterium Fusion Neutrons at the Omega Laser Facility,” 2016 R-Matrix Workshop on Methods and Applications, Santa Fe, NM, 27 June–1 July 2016.

The following presentations were made at the CEA-NNSA Workshop, Rochester, NY, 29–30 June 2016:

I. A. Begishev, J. Bromage, J. D. Zuegel, P. S. Datte, and S. T. Yang, “Record Fifth-Harmonic-Generation Efficiency Producing 211-nm Pulses Using Cesium Lithium Borate.”

V. Yu. Glebov, R. Flight, C. J. Forrest, J. P. Knauer, S. P. Regan, M. H. Romanofsky, T. C. Sangster, and C. Stoeckl, “A New Microchannel-Plate Neutron Time-of-Flight Detector.”

P. M. Nilson, F. Ehrne, C. Mileham, D. Mastrosimone, R. K. Jungquist, C. Taylor, R. Boni, J. Hassett, C. R. Stillman, S. T.

Ivancic, D. J. Lonobile, R. W. Kidder, M. J. Shoup III, A. A. Solodov, C. Stoeckl, D. H. Froula, K. M. Hill, L. Gao, M. Bitter, P. Efthimion, and D. D. Meyerhofer, “High-Resolving-Power, Ultrafast Streaked X-Ray Spectroscopy on OMEGA EP.”

W. Theobald, C. Sorce, M. Bedzyk, F. J. Marshall, C. Stoeckl, S. P. Regan, T. Hilsabeck, J. D. Kilkenny, D. Morris, M. Chung, J. Hares, A. Dymoke-Bradshaw, P. Bell, J. Celeste, A. Carpenter, M. Dayton, D. K. Bradley, M. C. Jackson, L. Pickworth, S. Nagel, G. Rochau, J. Porter, M. Sanchez, L. Claus, G. Robertson, and Q. Looker, “Conceptual Design of a Single-Line-of-Sight Resolved X-Ray Imager on OMEGA.”



